FTL REPORT R82-5

THE INTERACTION OF RADIO FREQUENCY

ELECTROMAGNETIC FIELDS

WITH ATMOSPHERIC WATER DROPLETS

AND APPLICATIONS TO AIRCRAFT ICE

PREVENTION

Robert John Hansman, Jr.

June 1982

MIT

DEPARTMENT
OF
AERONAUTICS
&
ASTRONAUTICS

FLIGHT TRANSPORTATION
LABORATORY
Cambridge, Mass. 02139

FTL REPORT R82-5

THE INTERACTION OF RADIO FREQUENCY ELECTROMAGNETIC FIELDS

WITH ATMOSPHERIC WATER DROPLETS

AND APPLICATIONS TO AIRCRAFT ICE PREVENTION

by

ROBERT JOHN HANSMAN, JR.

June 1982

THE INTERACTION OF RADIO FREQUENCY ELECTROMAGNETIC FIELDS
WITH ATMOSPHERIC WATER DROPLETS
AND APPLICATIONS TO AIRCRAFT ICE PREVENTION

by

Robert John Hansman, Jr.

ABSTRACT

In this work the physics of advanced microwave anti-icing systems, which pre-heat impinging supercooled water droplets prior to impact, is studied by means of a computer simulation and is found to be feasible. In order to create a physically realistic simulation, theoretical and experimental work was necessary and the results are presented in this thesis.

The behavior of the absorption cross-section for melting ice particles is measured by a resonant cavity technique and is found to agree with theoretical predictions. Values of the dielectric parameters of supercooled water are measured by a similar technique at $\lambda = 2.82$ cm down to $-17^{\circ}C$. The hydrodynamic behavior of accelerated water droplets is studied photographically in a wind tunnel. Droplets are found to initially deform as oblate spheroids and to eventually become unstable and break up in Bessel function modes for large values of acceleration or droplet size. This confirms the theory as to the maximum stable droplet size in the atmosphere. A computer code which predicts droplet trajectories in an arbitrary flow field is written and confirmed experimentally. Finally, the above results are consolidated into a simulation to study the heating by electromagnetic fields of droplets impinging onto an object such as an airfoil. Results indicate that there is sufficient time to heat droplets prior to impact for typical parameter values and design curves for such a system are presented in the study.

ACKNOWLEDGEMENTS

I wish to express my appreciation to all those who helped make this work possible. Particularly Professor Walter Hollister, who provided direction and support, and to the rest of my committee, Professor Robert Kyhl, Professor Richard Passarelli, and Professor Bernard Burke, for their helpful advice. I would also like to thank Professor Robert Simpson, who provided me with a home in the Flight Transportation Laboratory and Charles Miller for his photographic advice.

I wish to thank Al Shaw, Paul Bauer and Don Weiner for their technical support, John Pararas for his help with computer graphics and especially Bob McKillip for his "Quick Programming Course". I thank also Steve Knowlton for his discussions and companionship and the members of the Flight Transportation Laboratory.

The production of this thesis was made possible by the typing and editorial skills of Abby Crear, the drafting skills of Laura Wernick and the software of Bob McKillip.

My deepest thanks are due to my parents, to Laura Wernick, and to my many friends who motivated and supported me through the highs and lows of the research described in this thesis.

TABLE OF CONTENTS

5

CHAPTER 1

INTRODUCTION

Aircraft icing has long been recognized as one of the most serious meteorological hazards to flight. Ice formation can result in loss of aerodynamic efficiency, control and visibility, as well as an increase in aircraft weight and the failure of vital communication or instrumentation sources. While a variety of techniques have been applied to the icing problem, there are still areas where present systems fall short.[1,2]

The work described in this thesis is centered around understanding the physics of advanced concepts in aircraft ice protection which employ microwave electromagnetic radiation. While understanding the physics of advanced concepts was the fundamental thread which united the work, it was often necessary, in the course of the work, to cross into other fields in order to obtain a satisfactory understanding of the physics involved. Some of the fields in which experimental or theoretical work was necessary are Atmospheric Physics, Experimental and Computational Fluid Dynamics and the Interaction of Electromagnetic Radiation with Matter. As a result of the research, contributions have been made in each of the above fields enroute to the original objective of understanding the physics underlying microwave ice prevention systems.

In Section 1.1 the icing problem will be defined and current techniques used to deal with it will be discussed. In Section 1.2

some of the concepts for microwave ice protection will be described. In Section 1.3 an outline of the following chapters and their relationship to the thesis will be presented.

1.1   The Icing Problem

Ice forms on aircraft structures when flight is conducted through areas of supercooled cloud or precipitation droplets. Supercooled water droplets, which occur commonly in the atmosphere, exist in a metastable state. If some structure, such as an aircraft, comes in contact with a supercooled drop, then it will begin to heterogeneously nucleate and form ice. The rate of nucleation and subsequent freezing depends on the structure and on the temperature of the drop. This is the basic mechanism for ice formation on aircraft.

For slightly supercooled drops (-5°C to 0°C), the drops freeze slowly after impact and smooth "clear" ice is formed. For colder temperatures (-20°C to -5°C), droplets freeze quickly and an opaque, irregular "rime" ice is formed. Below -20°C, supercooled water becomes less common in the atmosphere as homogeneous nucleation begins to occur and at temperatures below -40°C essentially all water is in the ice phase.[3]   Frozen hydrometers do not contribute to the icing problem, as those particles which do strike the structure bounce off.

The values of droplet and liquid water content applicable to U.S. continental cumuliform and stratiform clouds are presented in the design criterion for ice protection certification in Part 25 of the U.S. Federal Aviation Regulations (FAR's).[4,5]   However, the FAR's neglect icing from supercooled precipitation droplets, such as

freezing rain. Table 1 summarizes the range of droplet parameters applicable for cloud and precipitation icing.

While a description of the meteorological conditions which lead to icing is fairly easy to provide, accurate forecasting of these conditions is much more difficult. This is due to difficulties in predicting whether a cloud will be in the supercooled-water or ice phase, which can change quickly with time. For example, if some ice phase particles are introduced into a supercooled cloud, through heterogeneous nucleation or some other means, then the cloud will very rapidly transition to the ice phase, due to the fact that the saturation vapor pressure over ice is lower than over water.[6] In addition, icing zones have been observed to be fairly localized even when accurately predicted.[7]

The uncertainty in predicting icing conditions causes forecasters to be conservative and to forecast icing conditions anytime the potential exists. The conservative nature of icing forecasting has two detrimental effects. The most important is the "cry wolf" syndrome, where pilots become accustomed to flying in forecast icing conditions with no difficulty and ignore icing forecasts in more severe conditions. This is borne out by the fact that in 92% of the icing accidents between 1973 and 1977, icing conditions were correctly forecast.[2]

The second detrimental effect of conservative forecasting is economic. Most general aviation aircraft are not certified for flight into "known" icing conditions. While the definition of "known" icing is somewhat ambiguous, many operators choose not to fly in

Table 1.   Parameters of the Icing Problem

	Cloud Droplets	Precipitation Droplets
Temperature	$0^{\circ}C \rightarrow 20^{\circ}C$	$0^{\circ}C \rightarrow -5^{\circ}C$
Liquid Water Content	$0 \rightarrow 1$ gm/m^3	$0 \rightarrow 3$ gm/m^3
Mean Drop Diameter	$10 \rightarrow 40$ microns	$1 \rightarrow 5$ mm

forecast icing conditions.   Cancellations due to invalid forecasts are a drain on the aircraft operators and the economy in general.

The reason for the conservative approach to aircraft icing are the inherent dangers.   Some of these are:

Loss of aerodynamic efficiency
> Increased drag
> Decreased lift
> Increased stall speed

Increased weight
Loss of control movement
Engine failure
Aeroelastic flutter resulting from change in structural mass
> distribution

Loss of visibility through windshield
Loss of navigation and communication antenna
Loss of cockpit instrumentation sources (pitot, static, etc.)
Loss of onboard radar

The above icing-related phenomena can occur singly or multiply with varying degrees of severity, depending on the icing conditions, the aircraft and the ice protection equipment on board.

The available ice protection devices come in two basic forms, anti-ice (no ice is allowed to form), and de-ice (some ice forms and is subsequently removed).   The current techniques all have advantages and drawbacks.   Electrothermal and hot-air anti-ice devices are very effective, but require large amounts of energy in that they evaporate all impinging water at a cost of 600 cal/gm (2.5 $\times$ 10^{10} erg/gm).   Freezing-point depressants such as glycol or chemical pastes are efficient but are subject to erosion on the leading edge, and combustion problems.   Pneumatic de-icing boots are efficient, but tend to be unreliable and subject to misuse.

From the foregoing, there is clearly a need for advancement, both in the ability to accurately forecast icing conditions and in ice protection once icing conditions are encountered. In addition, a better understanding of the icing problem on the part of pilots, as well as researchers, will help increase the safety and productivity of flight.

1.2 Concepts for Microwave Ice Protection

The use of microwave electromagnetic energy for ice protection has been proposed by a variety of researchers for both ice detection and ice prevention roles. Remote detection of localized icing zones was proposed by Atlas in 1954.[8]   Using meteorological radar, zones of moderate to high liquid water content above the freezing level can be observed in real time. With the advances in ground-based and airborne radar, this approach holds great promise. In 1976, Magenheim proposed using microwaves to detect the local accumulation of ice on airfoils and helicopter rotors by measuring the change in impedance, as ice accumulates on the dielectric coating of a surface waveguide located on the leading edge of the airfoil.[9]   The technique is fairly successful but suffers from anomalous measurements when liquid water is mixed with the ice.

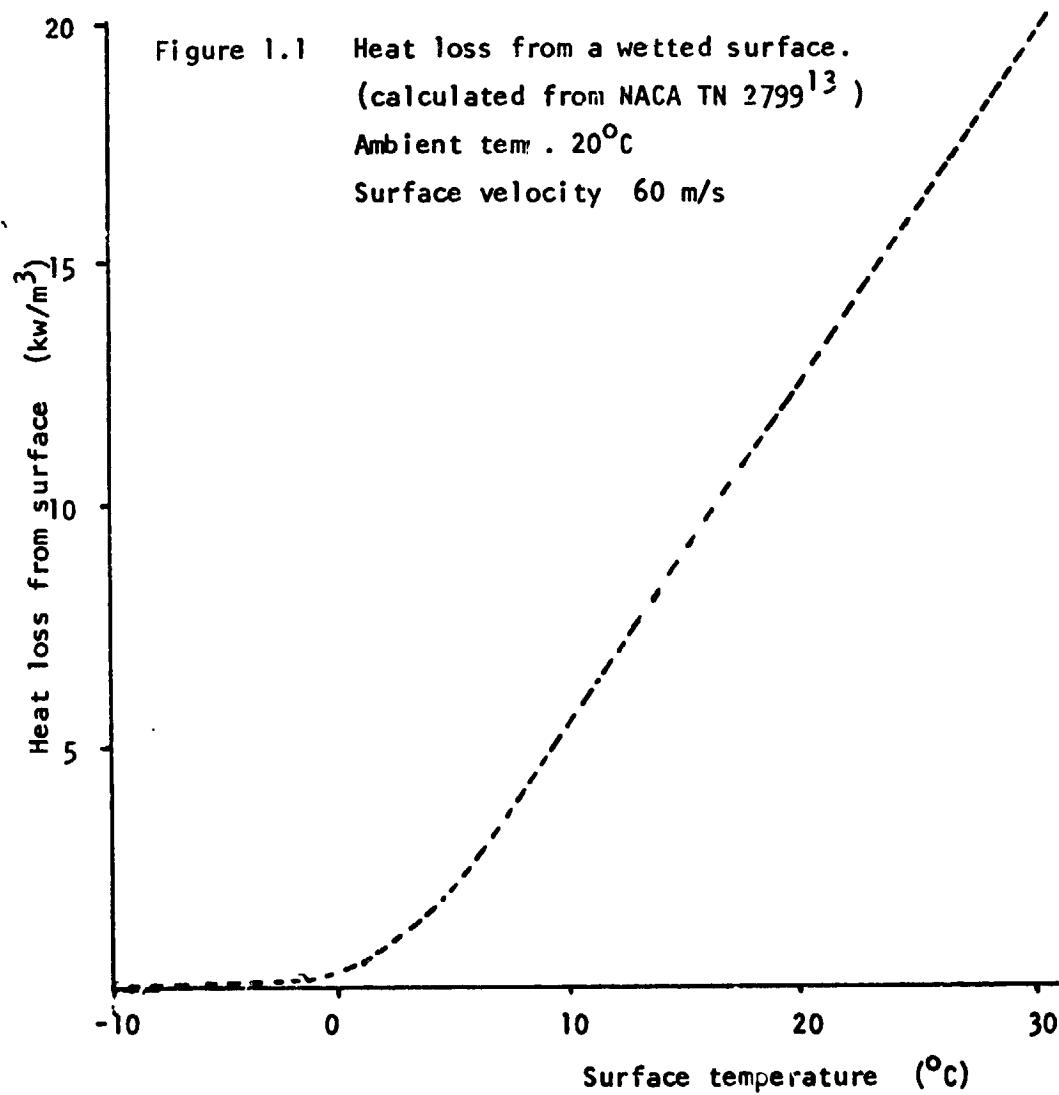Magenheim also proposed using microwave energy in a de-icing system. In this scheme, microwave heating at the ice dielectric interface of a surface waveguide, located on the leading edge of the airfoil, is used to break the adhesion bond of ice. This technique was demonstrated in 1976.[10]   However, it has no real advantage over electrothermal de-icing techniques, which operate on the identical

principle, and has some disadvantages in terms of complexity and efficiency.

In 1980, Hansman and Hollister proposed using microwave heating to prevent the formation (anti-ice) on aircraft structures.[11,12] The concept is to preheat the supercooled water droplets to above freezing prior to impact by a microwave field ahead of the airfoil and thereby prevent ice from forming.   The potential advantages seen for a microwave anti-icing system are low power consumption, low maintenance and aerodynamic cleanliness, as opposed to other anti-ice techniques. Low power consumption is anticipated due to the saving of the latent heat of fusion (80 cal/gm, 3.35×10^9 erg/gm) by circumventing the water-to-ice-to-water phase transitions, and to the ability of selectively heating supercooled water droplets.   The selective heating of water droplets is a result of the strong absorption character'stic of water in the microwave regime, whereas snow, ice and metal surfaces are poor absorbers.   This implies that the wing need not necessarily be as hot as with other techniques, which minimizes convective and evaporative losses.

The advantage of keeping the airfoil as cool as possible can be clearly seen in Figure 1.1, where the heat loss from a wet surface exposed to a tangential flow is plotted as a function of surface temperature.[13]   The ambient temperature is $-20^\circ C$ and the tangential velocity is 60 m/sec.   The heat flux increases dramatically above $0^\circ C$ due to conductive and evaporative losses.   In order to run the airfoil as cool as possible and still prevent runback freezing problems, the optimally efficient anti-icing system is most likely

Figure 1.1 Heat loss from a wetted surface.
(calculated from NACA TN 2799[13])
Ambient temp. 20°C
Surface velocity 60 m/s

a microwave hybrid.   In a hybrid system a microwave leading edqe
system would be combined with either a freezing-point depressant or
an electrothermal system on the aft airfoil sections.   Advanced
freezing-point depressant pastes [14] have been successful at suppressing
runback refreezing, and can operate at ambient temperatures, but are
subject to rapid erosion on the airfoil leading edge.   Electrothermal
systems which operate slightly above freezing are also efficient,
but have a problem initially heating the droplets.   These techniques
are, therefore, well-suited to being combined with microwave pre-
heating in order to approach optimal efficiency in cases where
anti-icing is required.

Power requirements for typical general aviation parameters are
estimated for the microwave system to be on the order of 100 W for
propeller anti-icing and 1 kW for wing anti-icing.   An additional
advantage of the microwave system is that, neglecting circuit losses,
power is only consumed when liquid water is present, and thereby
has the capability to serve as its own detector.

An example of a possible first-order microwave anti-icing scheme
employing surface waveguides is shown in Figures 1.2a and 1.2b.   In
Figure 1.2a, a cross-section of the airfoil showing the dielectric
inset for the surface wave is presented.   The electromagnetic wave
propagates along the leading edge of the airfoil and is bound to the
surface waveguide.   The electromagnetic field strength characteristi-
cally decays exponentially away from the waveguide.[15]   The waves are
launched at the wing root and propagate to the tip, where the energy
not absorbed by the water droplets is collected and recycled back

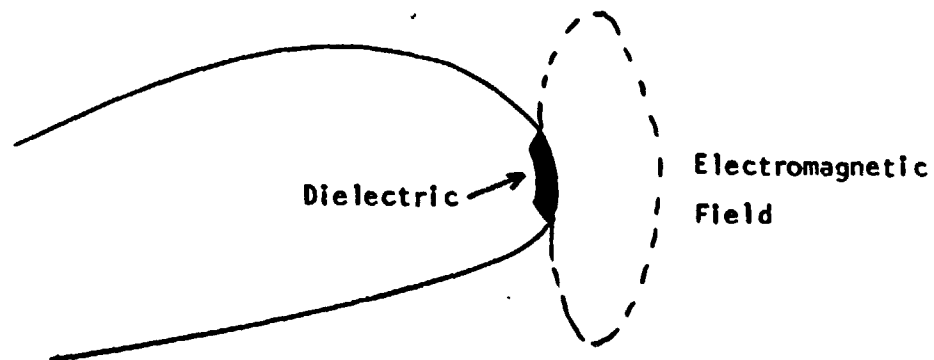Dielectric

Electromagnetic
Field

Figure 1.2a   Cross-section of an airfoil with
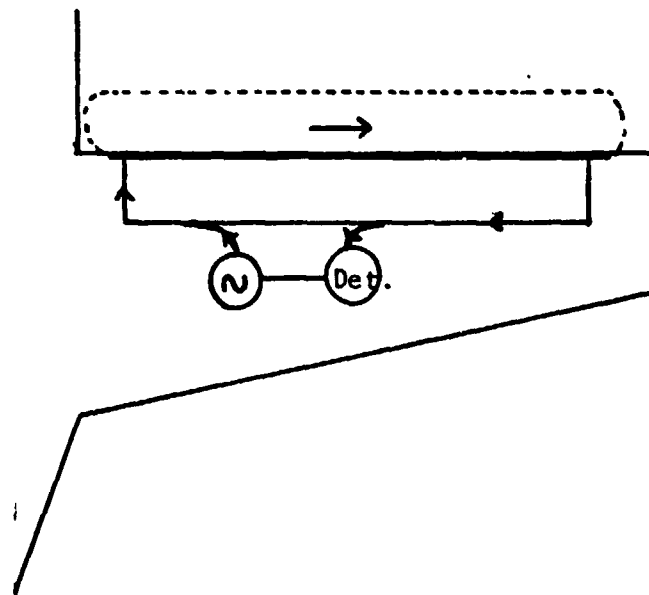surface waveguide.

Figure 1.2b   Schematic of the microwave anti-icing
system employing surface waveguides.

inside the wing to the root in a "race track" pattern.   It should be noted that the launching-retrieving process is not perfectly efficient.   The presence of liquid water can be measured by a power loss as observed through a directional coupler and detector on the return path of the circuit.

The microwave anti-ice system has some distinct and unique advantages over other anti-icing systems.   There are, however, several questions to be answered.   The primary question is whether there is sufficient time to heat impinging droplets at velocities of aeronautical relevance (80 to 200 mph).   While there are other questions such as runback-refreeze, electromagnetic field optimization and circuit efficiency, these become moot if there is not sufficient time to heat the droplets.   For this reason, the major thrust of this thesis will be to endeavor to determine, in a systematic manner, whether there is sufficient time to heat atmospheric water droplets to above freezing prior to impact.

1.3   Thesis Structure

The primary goal of this thesis, as discussed in Section 1.2, is to understand the physics of a supercooled water droplet being heated by microwave electromagnetic energy, as it approaches an airfoil.   This problem is studied by means of a computer simulation in Chapter 6, which was designed to be as physically complete as possible.   In order to provide the physical background for the simulation, some preliminary work of a more basic nature was necessary.

In Chapter 2, the theory of absorption by hydrometers is

reviewed. In Chapter 3, the absorption and scattering of mixed-phase ice/water particles is studied, both theoretically and experimentally. In addition, values of the dielectric parameters for supercooled water droplets are experimentally measured. In Chapter 4, the deformation and stability of droplets subject to an external acceleration are studied, both theoretically and in the wind tunnel. This work is intended to be combined with that of Chapter 2, where deviations from sphericity are found to have a pronounced effect on the absorption properties of droplets.

In Chapter 5, a computer simulation of water droplets is presented and experimentally verified. Finally, in Chapter 6 the results of the previous chapters are combined into a computer code, which follows the trajectories and heating of droplets as they approach an airfoil. In Chapter 7, the results and contributions of the work are briefly reviewed by way of a conclusion.

CHAPTER 2

THEORY OF ABSORPTION AND SCATTERING BY HYDROMETERS

A brief summary of basic scattering theory applicable to atmospheric hydrometers is presented in this chapter. In Section 2.1 some scattering terminology is defined. The known dielectric properties of liquid water and ice are presented in Section 2.2. In Section 2.3 and Section 2.4 the approaches of Mie, Rayleigh and Gans for scattering from spheres and ellipsoids are briefly discussed. Finally, in Section 2.5 the problem of a collection of scatterers is considered.

2.1   Scattering Terminology

In the classical formulation of the scattering problem, a plane wave is incident on the scattering object. Shown in Figure 2.1 are the cases of interest here. The wave is electromagnetic and propagates in the $\hat{n}_0$ direction with wave vector $\vec{k}_0 = \frac{2\pi}{\lambda} \hat{n}_0$. The wave is polarized with the electric field $\vec{E}_t$ in the $\hat{e}_0$ direction.

The scattering object is of arbitrary shape and is imbedded in a background of uniform dielectric material characterized by the complex dielectric constant ε_0. For most atmospheric applications, ε_0 is taken to be unity, the value for free space. The scattering object has a complex dielectric constant ε which can vary spatially. The background and the scattering object are assumed to be dielectric in nature. Therefore, the magnetic permeabilities of the background and the object are unity.
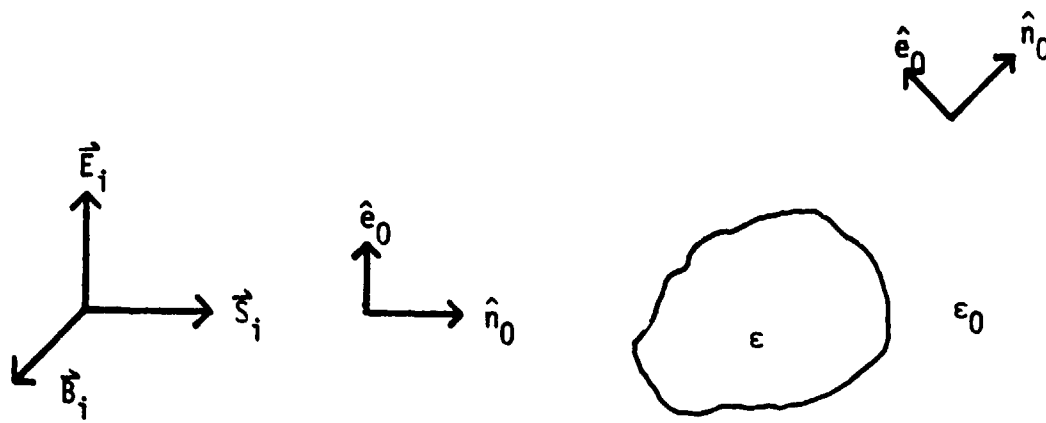
Figure 2.1   The scattering problem showing the incident and
scattered polarization and propagation vectors.

The energy flux of the incident wave is characterized by its Poynting vector

$$\vec{S}_i = \frac{c}{4\pi} \vec{E}_i \times \vec{B}_i \tag{2.1}$$

which is aligned in the $\hat{n}_0$ direction.

When the incident wave impinges on the object, energy can be lost either to scattering or to absorption by the object. These losses are characterized by various cross-sections. Cross-sections have units of area and, when multiplied by the incident Poynting flux, yield the power flow into absorption or scattering. Addition of the absorption cross-section σ_a and the scattering cross-section σ_s equals the total cross-section

$$\sigma_t = \sigma_a + \sigma_s \tag{2.2}$$

which measures the total energy flow out of the wave due to the object.

In many cases, the scattered energy is not isotropic. The differential cross-section, $\frac{d\sigma(\hat{n},\hat{e})}{d\Omega}$ is then used. When multiplied by $|S_i|$ it yields the power flux with polarization $\hat{e}$ through a differential of solid angle centered about the direction defined by $\hat{n}$. The scattering cross-section is then found by integrating over the total solid angle and all polarizations.

$$\sigma_s = \iint \frac{d\sigma(\hat{n},\hat{e})}{d\Omega} \, d\Omega \, d\bar{e} \tag{2.3}$$

For radar applications the energy scattered back toward the source is of special importance. Toward this end, the back-scatter cross-section σ_b is defined. It is the scattering cross-section of an isotropic source with a constant differential cross-section equal to that of the object in the backscatter or negative $\hat{n}_0$ direction.

$$\sigma_b = \iint \frac{d\sigma(\hat{n} = -\hat{n}_0)}{d\Omega} \, d\Omega d\hat{e} \tag{2.4}$$

It should be noted that in the literature, σ_a, σ_s, σ_t are sometimes replaced by Q_a, Q_s, Q_t, and σ_b is sometimes simply σ. The above convention has been chosen to avoid confusion with the "quality factor" Q in later sections.

2.2 The Dielectric Properties of Water and Ice

The dielectric properties of a non-magnetic material can be characterized by the real and imaginary parts of its complex dielectric constant.

$$\epsilon(f,T) = \epsilon'(f,T) - i\epsilon''(f,T) \tag{2.5}$$

The real part is a measure of the polarization of the material subject to an applied electric field. The imaginary part is a loss term measuring the energy transfer from the field to the material. The dielectric constant is a function of frequency f and temperature T. The frequency is related to the free space wavelength λ by the speed of light c.

$$f = \frac{c}{\lambda} \tag{2.6}$$

Unless otherwise noted, ε will be assumed to be equal to unity for background materials of air or free space.

Values of the dielectric constant for water and ice have been extensively measured. Several good tabulations have been published, with those of von Hippel[16] and Ryde[17] being especially useful.

The temperature dependence of ε' and ε'' for water at several wavelengths is plotted in Figures 2.2 and 2.3 from von Hippel's data. The dependence of ε' and the loss term ε'' on T is clearly not negligible, particularly at the lower temperatures. The absence of data for supercooled water is distressing, because of the strong dependence of ε on temperature. The lack of data is primarily due to the difficulty in maintaining supercooled water, in the liquid state, under controlled dielectric measuring conditions. However, supercooled water is important because it occurs commonly in nature.

For some applications it is convenient to define the complex refractive index m as the square root of ε:

$$m = \sqrt{\varepsilon} = n - i\kappa \tag{2.7}$$

where n is the refractive index and κ is the absorption coefficient of the material. It will also be convenient to define

$$K = \frac{m^2 - 1}{m^2 + 2} \tag{2.8}$$

Figure 2.2   Real part of the
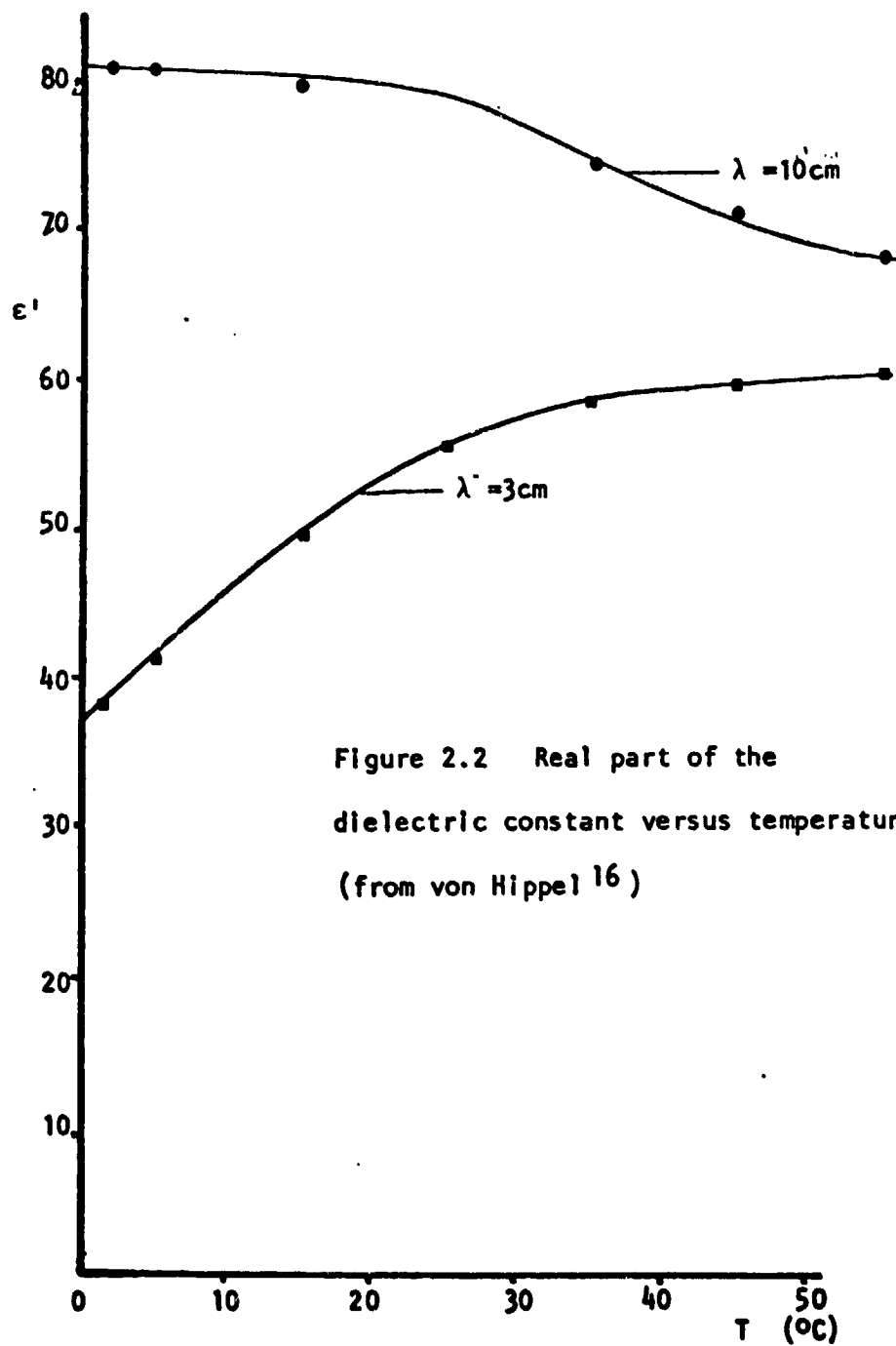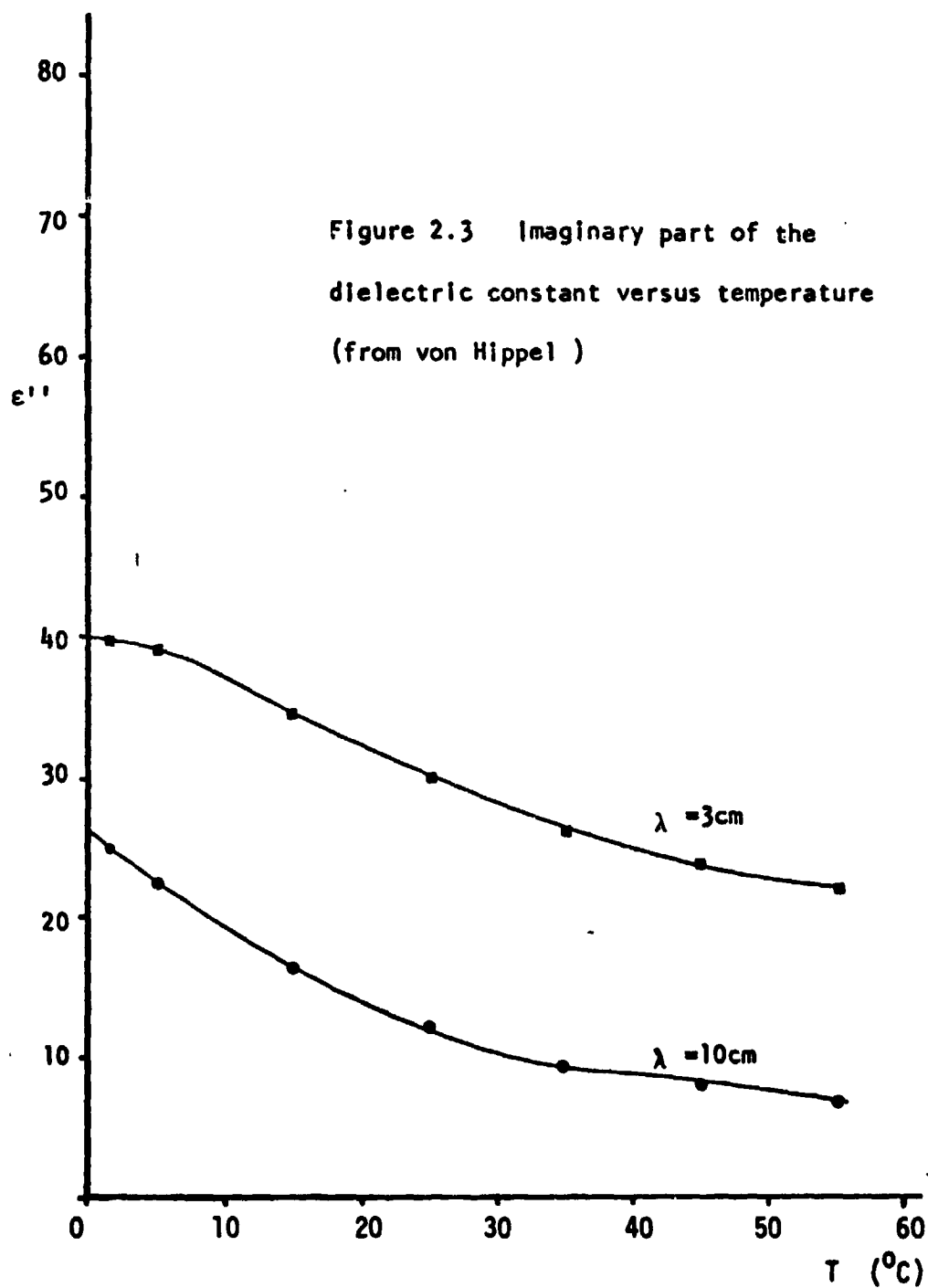dielectric constant versus temperature.
(from von Hippel [16])

Figure 2.3   Imaginary part of the
dielectric constant versus temperature
(from von Hippel)

Values of n, κ, $|K^2|$ and the imaginary part of $-K$ given by Ryde[10] are shown for water and ice in Tables 2.1 and 2.2.

2.3 Absorption and Scattering by Dielectric Spheres

The scattering of electromagnetic waves by a dielectric sphere is one of the few scattering problems for which there exists a complete analytical solution. The general solution was first published by Mie in 1908.[18] Mie's work was preceded by that of Lord Rayleigh. In 1871 Rayleigh solved the scattering problem in the long wavelength limit as part of his explanation for the blue color of the sky.[19,20] Both solutions are discussed in the following.

2.3.1 Mie Theory

Mie's analysis of scattering by a dielectric sphere[18] is simple in concept although somewhat complex in detail. The general approach will be outlined here along with the results. The reader is referred to Stratton's text[21] or Mie's original work[18] for the details.

Mie's approach was to write the field of the incident plane wave as the sum of vector spherical wave functions centered at the sphere. The incident field gives rise to oscillating charges in the sphere which produce secondary fields inside and outside of the sphere. These external and internal fields are also expanded in spherical wave functions. The expansion coefficients for the secondary fields are found by imposing boundary conditions at the origin and the surface of the sphere.

Table 2.1 Values of the dielectric parameters for water (taken from Ryde, 17)

$T(^{\circ}C)$		$\lambda(cm)$			
		10	3.21	1.24	0.62
20		8.88	8.14	6.15	4.44
10	n	9.02	7.80	5.45	3.94
0		8.99	7.14	4.75	3.45
-8			6.48	4.15	3.10
20		0.63	2.00	2.86	2.59
10		0.90	2.44	2.90	2.37
0	k	1.47	2.89	2.77	2.04
-8				2.55	1.77
20		0.928	0.9275	0.9193	0.8926
10	$|K|^2$	0.9313	0.9282	0.9152	0.8726
0		0.9340	0.9300	0.9033	0.8312
-8				0.8902	0.7921
20		0.00474	0.01883	0.0471	0.0915
10	$Im(-K)$	0.00688	0.9247	0.0613	0.1142
0		0.01102	0.0333	0.0807	0.1441
-8				0.1036	0.1713

Table 2.2 Values of the dielectric parameters for ice[*] (taken from Ryde, 17)

$T(^{o}C)$			
	n	1.78	At all temperatures
0		24×10^{-4}	
-10	k	7.9×10^{-4}	
-20		5.5×10^{-4}	
	$\lvert K \rvert^2$	0.197	At all temperatures. This is for ice of unit density, the value to be used when D is diameter of melted ice particle. (Marshall and Gunn, 1952)
0		9.6×10^{-4}	
-10	Im(-K)	3.2×10^{-4}	
-20		2.2×10^{-4}	

* Refractive index of ice is independent of wavelength in the centimeter band.

In order to calculate the cross-sections once the secondary fields are known, the Poynting flux is integrated over a spherical surface, concentric with the scatterer to yield the energy flow. Integrating the total Poynting vector, which includes the incident and secondary fields, will result in the energy flow into the sphere and thus σ_a. Integrating the scattered Poynting vector with only the secondary fields will yield the scattered energy flow away from the sphere or σ_s. The problem is simplified by assuming that the sphere of integration is large enough that the asymptotic values of the spherical wave functions can be used.

The foregoing analysis results in the following cross-sections

$$\sigma_t = \frac{\lambda^2}{2\pi} (-\text{Re}) \sum_{n=1}^{\infty} (2n + 1)(a_n + b_n) \tag{2.9}$$

$$\sigma_s = \frac{\lambda^2}{2\pi} \sum_{n=1}^{\infty} (2n + 1)(|a_n|^2 + |b_n|^2) \tag{2.10}$$

$$\sigma_a = \sigma_t - \sigma_s \tag{2.11}$$

$$\sigma_b = \frac{\lambda^2}{4\pi} \left| \sum_{n=1}^{\infty} (-1)^n (2n + 1)(a_n - b_n) \right|^2 \tag{2.12}$$

where λ is the wavelength in the background medium. The expansion coefficients of the exterior secondary field a_n and b_n can be thought of as the nth magnetic and electric multiple coefficients. They are made up of spherical Bessel functions and depend on properties of the sphere such as the complex refractive index m and α where $\alpha = \frac{2\pi a}{\lambda}$ and a is the radius of the sphere.

The Mie cross-sections have been calculated for ice and water spheres by a variety of investigators for different values of α and temperature. [17,22-25]

2.3.2 Rayleigh Theory

For small spheres or long wavelengths

$$\alpha = \frac{2\pi a}{\lambda} \ll 1 \tag{2.13}$$

the simplifying assumptions of Rayleigh can be made. Physically, the above constraint implies that the incident field is spatially uniform over the sphere. In this situation the exterior secondary fields from the sphere can be replaced by those of an oscillating dipole $\bar{p}$

$$\vec{p} = (\frac{\varepsilon - 1}{\varepsilon + 2})\, a^3 \, \vec{E}_i = (\frac{m^2 - 1}{m^2 + 2})\, a^3 \, \vec{E}_i \tag{2.14}$$

where a is the radius of the sphere and $\vec{E}_i$ is the incident electric field. The cross-sections σ_s and σ_b are calculated using these fields. The absorption cross-section σ_a can be calculated from the ohmic losses of the oscillating charges required to create the dipole.

The preceding cross-sections can also be calculated using the Mie formalism by expanding the coefficients a_n and b_n in terms of α. By neglecting terms of higher order than α^6, all multipoles higher than the dipole drop out. Both approaches yield the following cross-sections[23]

$$\sigma_t = \sigma_a + \sigma_s \tag{2.15}$$

$$\sigma_s = \frac{2}{3} \frac{\lambda^2}{\pi} \ \alpha^6 \ |K|^2 \tag{2.16}$$

$$\sigma_a = \frac{\lambda^2}{\pi} \ \alpha^3 \ Im(-K) \tag{2.17}$$

$$\sigma_b = \frac{\lambda^2}{\pi} \ \alpha^6 \ |K|^2 \tag{2.18}$$

where

Values of $|K^2|$ and $Im(-K)$ are tabulated in Section 2.2. Noting that $\alpha = \frac{2\pi a}{\lambda}$ the scattering cross-section and backscatter cross-section have the characteristic $1/\lambda^4$ dependence known as Rayleigh's law.

The Rayleigh cross-sections are of extreme importance in the study of scattering from atmospheric hydrometers. They are valid over a wide range of useful parameters and are the basis of comparison for those refinements which attempt to include such additional effects as non-spherical shape or non-homogeneous material.

2.4 Absorption and Scattering by Ellipsoids

The problem of scattering by an ellipsoid of revolution was treated in the long wavelength limit by Gans in 1912.[26] Gans' approach is essentially an extension of Rayleigh's work. He resolves the incident electric field into components along three perpendicular axes, one being the axis of rotation of the ellipsoid. Gans then assumes that

the electric field components excite dipole oscillations along the
ellipsoid axes.   Scattering phenomena can then be calculated by analogy
to Rayleigh scattering.

If the ellipsoid coordinate system is ξ, η, $\times$, with ξ the
axis of revolution, then the dipole moments given by Gans are

$$P_\xi = gE_\xi \tag{2.20}$$

$$P_\eta = g'E_\eta \tag{2.21}$$

$$P_\chi = g'E_\chi \tag{2.22}$$

where

$$g = \frac{V(m^2 - 1)}{4\pi + (m^2 - 1)P} \tag{2.23}$$

$$g' = \frac{V(m^2 - 1)}{4\pi + (m^2 - 1)P'} \tag{2.24}$$

for oblate spheroids.

$$P = 4\pi - 2P' = \frac{4\pi}{e}\ [1 - \sqrt{\frac{1 - e^2}{e^2}}\ \sin^{-1}e] \tag{2.25}$$

and for prolate spheroids.

$$P = 4\pi - 2P' = 4\pi\ \frac{1 - e^2}{e^2}\ [\frac{1}{2e}\ \ln(\frac{1 + e}{1 - e}) - 1] \tag{2.26}$$

where   V   is the volume of the ellipsoid and   e   is the eccentricity
defined as

$$e = \sqrt{1 - (B/A)^2} \tag{2.27}$$

$$V = \frac{4}{3} AB^2 \qquad \text{Prolate} \qquad\qquad (2.28)$$

$$V = \frac{4}{3} A^2B \qquad \text{Oblate} \qquad\qquad (2.29)$$

with A and B being the major and minor radii of the ellipsoid.

The Gans backscatter cross-sections for water, ice and snow have been calculated for randomly and preferentially oriented ellipsoids by Atlas, Kerker, and Hirschfeld.[27] Their work indicates that for water ellipsoids oriented with major axis along $\vec{E}_i$, σ_b increases roughly linearly with axes ratio A/B up to values of order 10. This effect is geometrical and has little dependence on wavelength. Ice and snow are seen to be only weakly dependent on geometrical factors due to their generally small dielectric constant.

The absorption cross-section for oriented ellipsoids will be of particular interest in later sections and was not calculated by Atlas, et al. Therefore σ_a will be calculated here using the Gans approach. The incident electric field is assumed to propagate perpendicular to the axis of rotation of the ellipsoid. The problem then becomes essentially two-dimensional. In Figure 2.4 the orientation angle θ is defined as the angle between $\vec{E}_i$ and ξ.

The absorption cross-section σ_a is calculated by assuming that the ξ and η dipoles have separate cross-sections σ_ξ and σ_η which are excited by the appropriate components of the incident field. The absorption cross-section is then

$$\sigma_a = \sigma_\xi \cos^2\alpha + \sigma_\eta \sin^2\alpha \qquad\qquad (2.30)$$
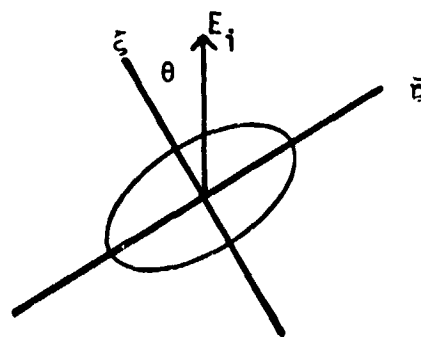
Oblate Ellipsoid
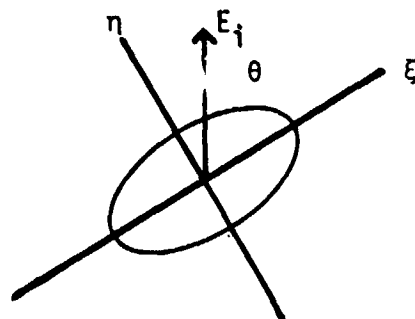
Prolate Ellipsoid

Figure 2.4 Orientation of the incident electric field
with respect to the ellipsoid coordinate system.

The partial cross-sections σ_ξ and σ_η are defined by analogy to Rayleigh scattering as

$$\sigma_\xi = \frac{8\pi^2}{\lambda} \; \text{Im}(-g) \tag{2.31}$$

$$\sigma_\eta = \frac{8\pi^2}{\lambda} \; \text{Im}(-g') \tag{2.32}$$

where λ is the free space wavelength and g, g' are the Gans factors.

The ratio of σ_ξ and σ_η for water at $0^\circ C$ to σ_a of an equivolumetric sphere is plotted versus the axis ratio A/B for oblate and prolate spheroids in Figures 2.5 and 2.6. Of interest is the strong increase in absorption as the ellipsoid becomes more eccentric. This appears to be valid independent of wavelength, subject to the long wavelength limit.

2.5   Absorption and Scattering by a Collection of Scatterers

In many cases of significance, the scattering object is actually a collection of smaller scatterers. The absorption cross-section σ_a for such a collection is, to first order, just the sum of all the individual cross-sections

$$\sigma_a = \sum_j \sigma_{a,j} \tag{2.33}$$

as long as the scatterers are not in immediate proximity to one another. This can be illustrated by considering two Rayleigh spheres of radius a separated by a distance r. The scattered electric field from sphere 1

Figure 2.5   Ratio of σ_ξ and σ_η to the spherical value versus A/B.

Oblate Ellipsoids

Figure 2.6   Ratio of σ_ξ and σ_η to to spherical value versus A/B.
Prolate Ellipsoids
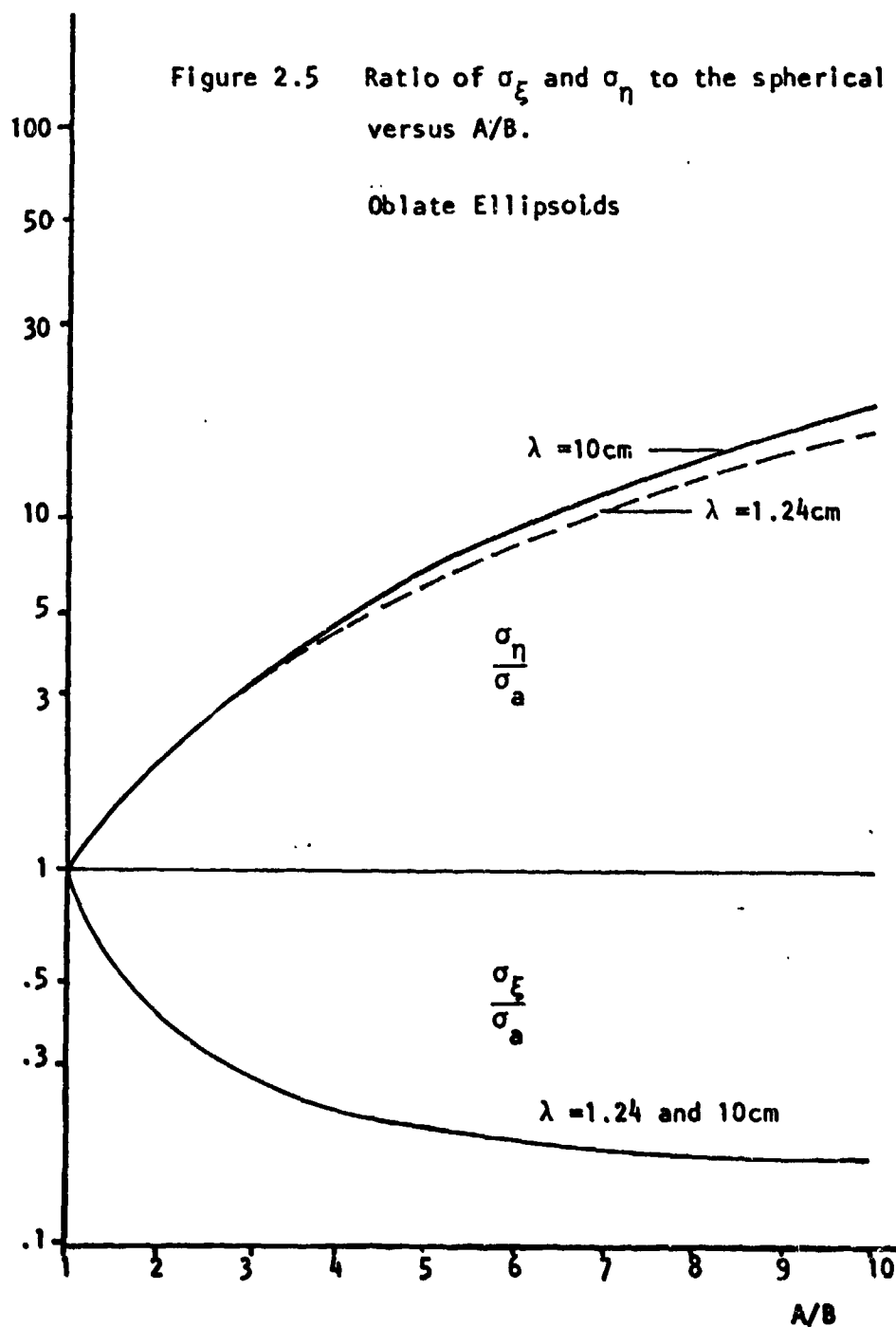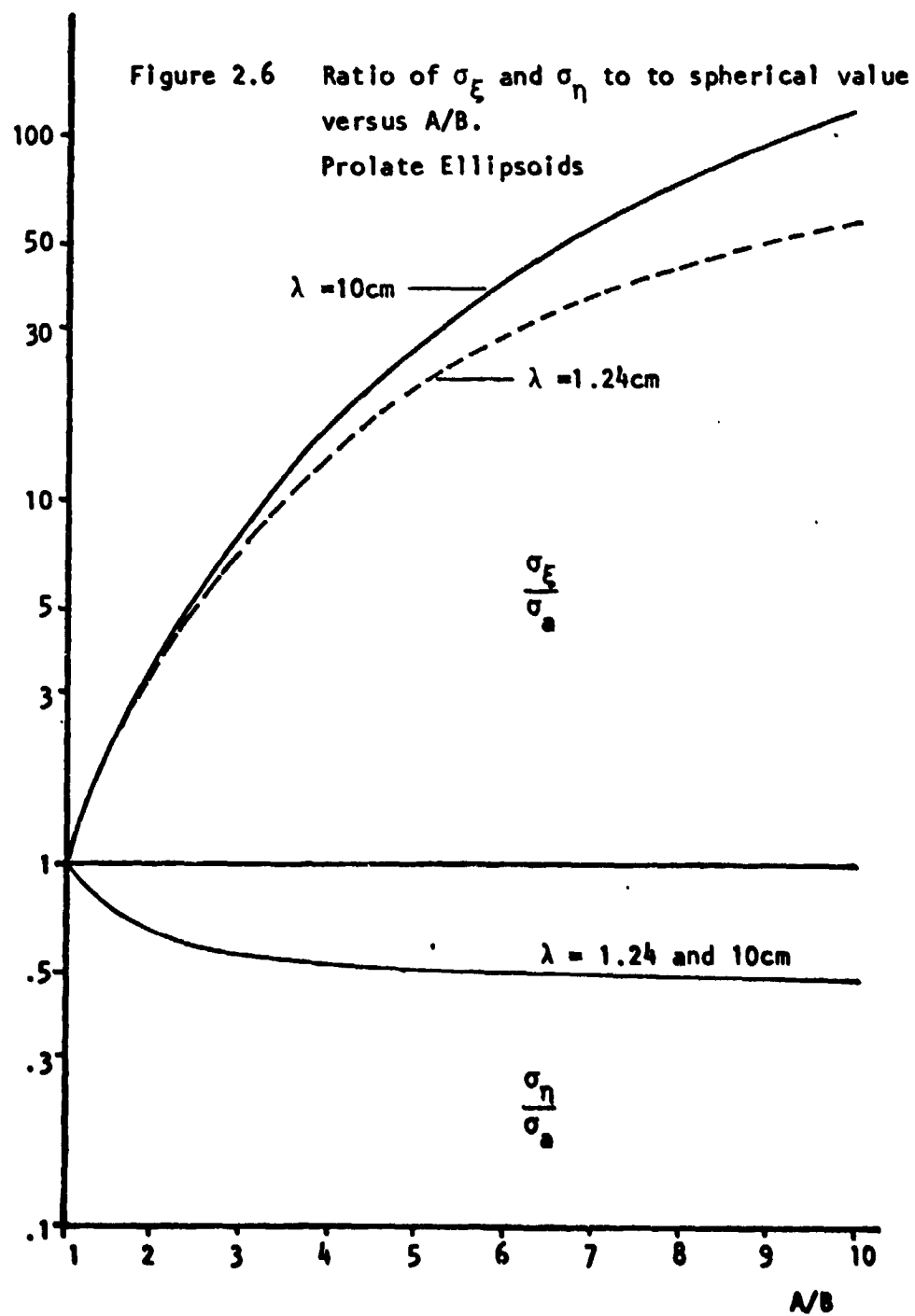
felt by sphere 2 is of order $(\frac{a}{r})^3 E_i$ where E_i is the incident electric field. It is clear that for interparticle spacings greater than a few radii, the incident field dominates and the particles absorb independently.

Collective effects can be important for the scattering cross-sections. In the case of identical scatterers the differential scattering cross-section can be written as[28]

$$\left(\frac{d\sigma}{d\Omega}\right)_{\substack{all \\ scatterers}} = F(\vec{q}) \left(\frac{d\sigma}{d\Omega}\right)_{\substack{one \\ scatterer}} \tag{2.34}$$

where $F(q)$ is the structure factor used in x-ray crystallography. It depends on the distribution of scatterers and is defined as

$$F(\vec{q}) = |\sum_j \exp(i\vec{q} \cdot \vec{x}_j)|^2 \tag{2.35}$$

The vector q is the change in wave vector

$$\vec{q} = \vec{k}_0 - \vec{k}_s$$

and $\vec{x}_j$ is the position of the jth scatterer.

It is instructive to consider $F(\vec{q})$ for the backscatter cross-section $\vec{q} = 2\vec{k}_0$. For a uniform distribution of fixed identical scatterers

$$F(2\vec{k}_0) = 0 \tag{2.36}$$

This is due to the phase cancellation of backscatter signal from

one scatterer by another separated by an integer number of half wave-lengths along the incident direction. If, however, there is some relative motion between the scatterers, then the phase cancellation averages out and

$$F(2\vec{k}_0) = N \tag{2.37}$$

where N is the number of scatterers. The backscatter cross-section for meteorological scatterers can then be written as

$$\sigma_b = \sum_j \sigma_{b,j} \tag{2.38}$$

This effect allows the backscatter cross-section to be related to such meteorologically relevant parameters as the liquid water content and the rainfall rate.

CHAPTER 3

ABSORPTION AND SCATTERING THROUGH THE ICE-WATER PHASE TRANSITION

The problem of scattering from melting and freezing hydrometers is considered in this chapter.   In Section 3.1 the theory of scattering from mixed-phase particles is discussed, along with a model for scattering by melting atmospheric particles.   In Section 3.2, experimental techniques used to measure absorption during the phase transitions are presented.   Finally, Section 3.3 contains the results of the absorption cross-section measurements.

3.1 Theory of Scattering by Melting and Freezing Hydrometers

The scattering by water-coated ice spheres has been studied theoretically by several investigators.   In 1951 Aden and Kerker[29] extended Mie's theory to the case of two concentric spheres.   In 1952, Langleben and Gunn[30] calculated cross-sections for water-coated ice spheres using the Aden and Kerker results.   Additional cross-sections have been calculated by Ba..en, Herman and Browning.[31,32]   Experimental measurements of the backscatter cross-sections for large melting ice spheres were made by Atlas et al in 1960.[33]

Labrum studied the problem of scattering by two confocal ellipsoids in 1952[34] in an attempt to explain enhanced reflection from the "bright band".   The "bright band" is observed on meteorological radar as a highly-reflective zone located just below the freezing level. The enhanced reflection in the "bright band" can only be partially explained by the dynamics of melting precipitation particles.   Labrum applied the Gans methodology to calculate backscatter cross-sections.

He also made some experimental measurements of backscatter from melting nonspherical ice particles.[35] Because of experimental difficulties, however, Labrum was only able to get general qualitative agreement with the theoretical backscatter cross-sections.

In Section 3.1.1, the above theoretical results for spheres and ellipsoids will be summarized. In Section 3.1.2, a model of the melting and scattering processes which include the theoretical cross-sections will be presented.

3.1.1   Water-Coated Ice Spheres and Ellipsoids

An example of the absorption, scattering, and backscatter cross-sections calculated by Langleben and Gunn[30] is shown in Figure 3.1. In this case the wavelength is 3 cm and the equivalent melted diameter D_{eq} of the sphere is 2.4 mm. The cross sections are normalized by their melted values σ_{melted} and are plotted against the mass fraction of water f_w

$$f_w = \frac{M_w}{M_w + M_i}$$ (3.1)

where M_w is the mass of water in the sphere and M_i is the mass of ice.

The behavior of the cross-sections in Figure 3.1 with f_w is typical of those water-coated ice spheres with radius less than λ. The scattering cross-sections increase rapidly with f_w to the value for water spheres. The absorption cross-section rises very rapidly with f_w to more than twice the melted value between $f_w = .1$ and $f_w = .2$ and then gradually reduces to the melted value.

Figure 3.1

Theoretical normalized absorption and
scattering cross-sections versus mass fraction.

(from Langleben and Gunn   )
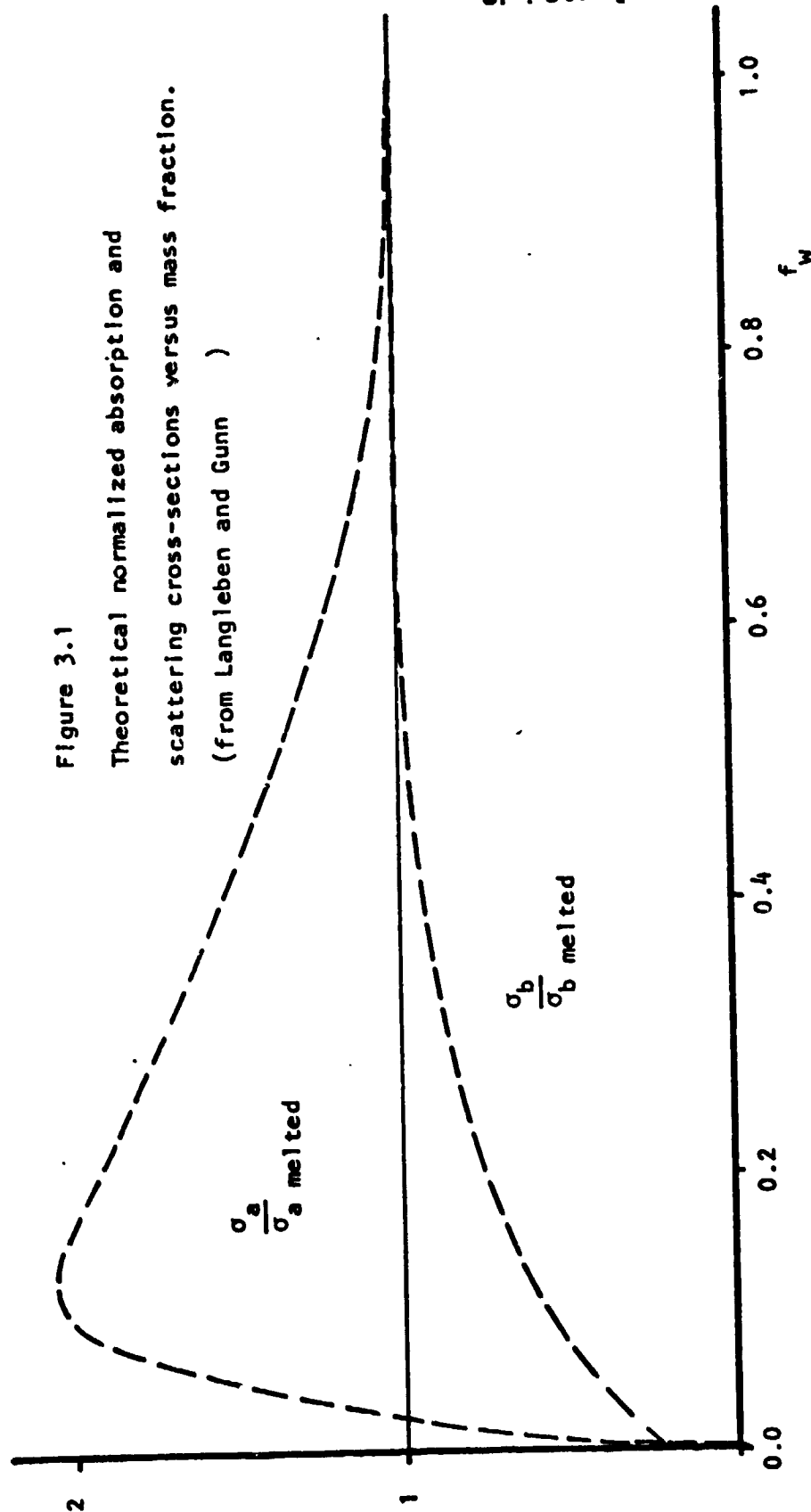
The increased absorption of a partially-melted ice sphere can be understood physically by considering the melted case. The absorption by a melted sphere can be thought of as ohmic losses arising from currents which create oscillating multipoles to match the boundary conditions at the sphere's surface. If an obstruction, in this case an ice sphere, is placed in the center of the water sphere, the path length for the currents is increased and the ohmic losses will similarly increase. If the ice sphere is very small there will be little effect, and if the sphere is predominantly ice, then the excited multiples are weaker and much of the current will flow in the low loss ice, resulting in little absorption.

For scattering from melting ellipsoids of revolution, it will be assumed that the melting effects of this section and the Gans shape effects of Section 2.4 can be included multiplicatively. Therefore

$$\sigma = \frac{\sigma}{\sigma_{melted}} \quad \frac{\sigma_{gans}}{\sigma_{sphere}} \quad \sigma_{sphere} \qquad (3.2)$$

Here σ is the cross-section to be calculated, $\dfrac{\sigma}{\sigma_{melted}}$ is the ratio of partially- to totally-melted cross-sections for a sphere. The ratio $\dfrac{\sigma_{gans}}{\sigma_{sphere}}$ is that of the Gans cross-section to an equivolumetric sphere and σ_{sphere} is the cross-section of the equivolumetric water sphere.

Backscatter cross-sections calculated as above agree with those of Labrum[34] to at least first order. The above simplification is considered acceptable considering that, for most applications, the assumption of an ellipsoid of revolution is itself only an approximation of some more complicated shape.

3.1.2   Model of Melting of Scatterers in the Atmosphere

The approximation of atmospheric scatterers as bodies of revolution works well for ice, where the low dielectric constant makes shape effect unimportant, and for small water drops where surface tension dominates.   For melting ice crystals, however, a somewhat more complex model must be used.   In order to model the melting process, snowflakes were observed as they fell onto a plate of warm glass.   Five distinct phases of the melting process were observed, although not every particle exhibited all five phases.

The five phases are shown schematically in Figure 3.2.   Phase 1 is the ice phase before melting.   In Phase 2 the crystal begins to melt at its extremities, where the heat transfer is the greatest.   Small water spheres begin to form at the extremities.   In Phase 3 enough water has melted to coalesce into a water shell.   There is, however, still sufficient ice structure in this phase to maintain a non-spherical shape.   In Phase 4 the ice has melted to such a point that the structural integrity of the ice is gone and the surface tension of the water causes the drop to collapse into a spherical shape.   Phase 5 is that of the totally-melted sphere.

The absorption and scattering characteristics of a melting ice particle are different in each of the five phases.   An example of the scattering behavior of a melting crystal is shown in Figure 3.3, where σ_a and σ_b are plotted against the mass fraction f_w.   In Phase 1 the particle scatters and absorbs like an equivolumetric ice sphere. In Phase 2 the particle can be approximated as a collection of Rayleigh scatterers.   The absorption cross-section is, therefore, a linearly-increasing function of f_w.   The backscatter cross-section is
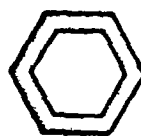
PHASE 1

PHASE 2
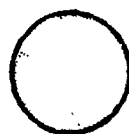
PHASE 3

PHASE 4

PHASE 5

Figure 3.2 Schematic representation of the five
phases of melting.

dependent on the form function $F(2\bar{k}_0)$ defined in Section 2.5. It will, in general, be a complicated function depending on the orientation of the particle and the locations where melting begins. In many cases the crystal will have some symmetry, hexagonal or otherwise, and the melting should initiate symmetrically, which simplifies calculation of F. The maximum value of F is N^2, where N is the number of water spheres.

In Phase 3, shape effects, as approximated by Gans scattering, are combined with the melting effects to calculate the cross-sections as in Section 3.1.1. In the example shown in Figure 3.3, the cross-sections are enhanced by shape effects, implying that the electric field is oriented at least partly along the major axis. It should be noted that the shape effects could also degrade the cross-sections to values lower than those of a melting sphere, if the electric field were oriented along a minor axis.

In Phase 4, the particle acts like a water-coated ice sphere for σ_a and σ_b. Finally, in Phase 5 when the particle is totally melted, the cross-sections are those of a water sphere.

Freezing water drops in the atmosphere exhibit much simpler behavior than the melting case. The drops are generally in the metastable supercooled state prior to melting. When crystallization occurs, it does so rapidly and relatively homogeneously. The scattering behavior of a freezing drop can be approximated by that of a sphere or an ellipsoid with a homogeneous dielectric constant

$$\varepsilon = \frac{\varepsilon_{ice} M_i + \varepsilon_{water} M_w}{M_i + M_w} \tag{3.3}$$

Figure 3.3 Theoretical behavior of σ_a and σ_b for the
five melting phases.
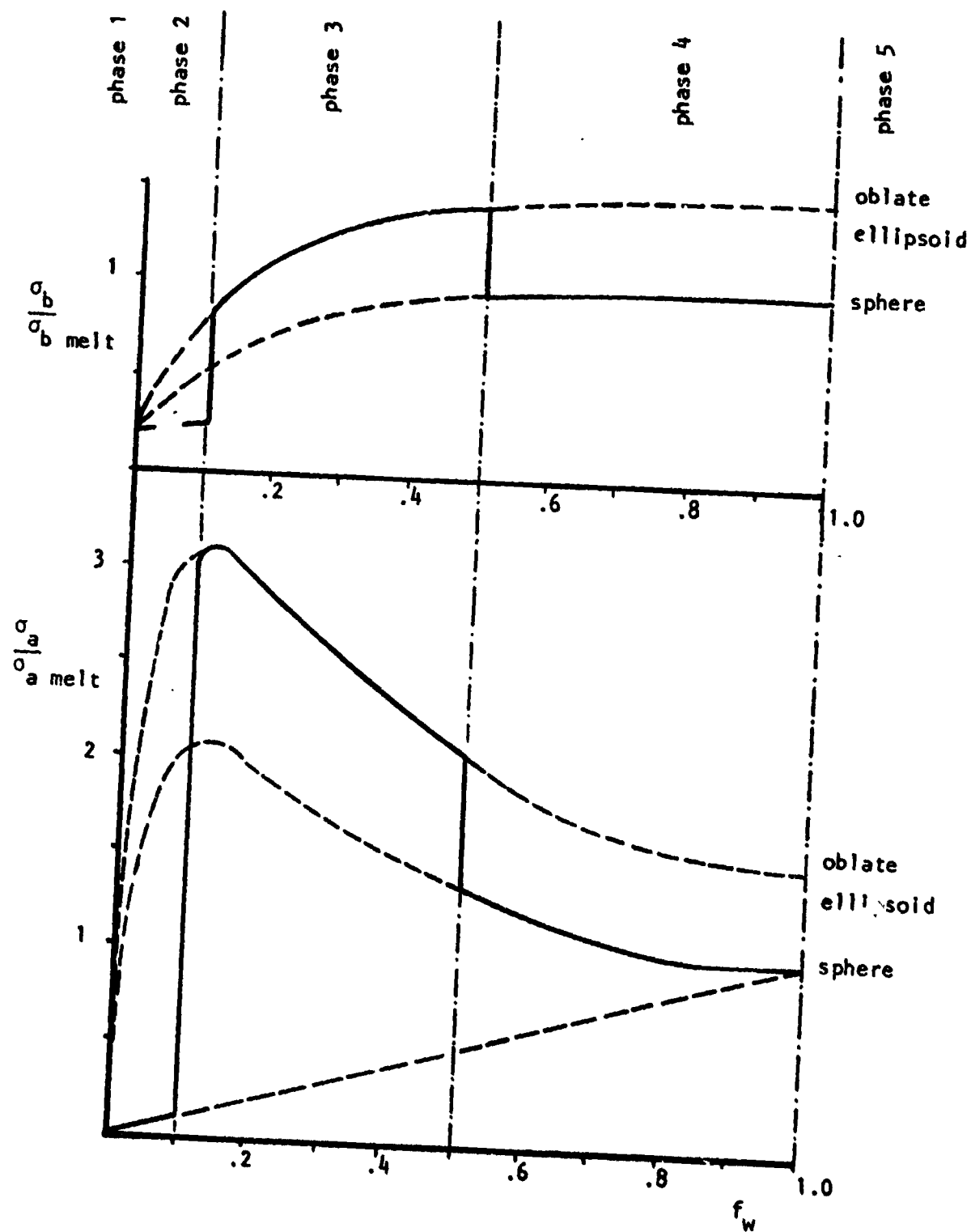
which is the mass weighted average of the dielectric constants ε_{ice} and ε_{water} of the constituents.

3.2   Experimental Methods for Measuring Absorption During Phase
Transition

Relatively few experimental measurements have been made to verify the theoretical cross-sections of melting and freezing hydrometers. Radar observations of phenomena such as the "bright band" yield some insight, but are subject to many uncertainties, due to factors such as precipitation dynamics, coalescence, and general uncertainty as to the exact nature of the scatterers.

Controlled experiments which measure the cross-sections of a single scatterer are difficult, due to the very small power changes involved.   Those measurements which have been made, by Labrum[35] and those by Atlas et al,[33] measured backscatter cross-sections under less-than-ideal conditions.   Labrum measured σ_b for melting hemispheres placed in a waveguide.   Atlas et al measured σ_b for very large melting spheres suspended by a balloon in the near field of a meteorological radar.

A technique for accurately measuring the absorption cross-sections of melting meteorological scale drops using perturbation techniques in a resonant microwave cavity has been developed.   Section 3.2.1 describes the technique and the particular cavity used in the experiments.   In Section 3.2.2 the experimental set-up is discussed. Section 3.3 contains the experimental results obtained using this technique.

3.2.1   Perturbation Techniques in a Resonant Cavity

The technique used for measuring the absorption cross-section σ_a consists, basically, of measuring the change in quality factor Q of a high Q resonant cavity where

$$Q = \omega \frac{\text{energy stored in cavity}}{\text{power loss in cavity}} = \omega \frac{U}{P} \tag{3.4}$$

and
$$\omega = 2\pi f \tag{3.5}$$

$$U = \text{energy stored in the cavity} \tag{3.6}$$

$$P = \text{power loss in the cavity} \tag{3.7}$$

The value of Q can be related to σ_a if the drop is non-magnetic and its dimensions are small compared with the scale length of the electric field inside the cavity.   Under these assumptions the scatterer sees an oscillating electric field of strength E_0.   The power absorbed by the drop P_d can be written using σ_a and the Poynting vector which would result if the electric field were in free space.

$$P_d = \sigma_a \frac{c}{8\pi} E_0^2 \tag{3.8}$$

To relate P_d to the change in Q when a drop is introduced into a cavity, the case of the empty cavity must first be considered.   For the empty cavity

$$Q_e = \omega \frac{U}{P_w} \tag{3.9}$$

where Q_e is the empty Q and P_w is the power dissipated in the walls of the cavity. When the drop is placed in the cavity, assuming U does not change, the perturbed value Q_p becomes

$$Q_p = \omega \frac{U}{P_w + P_d} \qquad (3.10)$$

If the droplet Q is defined as

$$Q_d = \omega \frac{U}{P_d} \qquad (3.11)$$

then

$$\frac{1}{Q_d} = \frac{1}{Q_p} - \frac{1}{Q_e} \qquad (3.12)$$

Noting Equations 3.8 through 3.12, the absorption cross-section can be written as

$$\sigma_a = \left(\frac{8\pi\omega U}{cE_0^2}\right) \frac{1}{Q_d} \qquad (3.13)$$

If the cavity is such that U is proportional to E_0^2, then the electric field strength will drop out.

The cavity chosen for drop measurements was a right circular cylinder operating in the TM_{010} mode. This mode was chosen because of its fairly uniform electric field at the center of the cavity oriented along the cavity axis. The TM_{010} mode also has very small surface currents on the end plates near the axis, allowing holes to be drilled in the endplates with minimal effect on the cavity fields.

The cavity was designed to resonate at 10.66 GHz. Its diameter D was 2.153 cm and its length L was 1.229 cm. Figure 3.4 is the mode chart for right circular cylinders,[36] showing the operating point for the cylinder. There is good mode separation, with the closest mode being the TE_{111} at 14.4 GHz. Since the TM_{010} is the lowest mode, frequencies lower than the TM_{010} resonance are cut off. The cavity is constructed out of copper and the empty Q is calculated to be 9000.

The electric and magnetic fields for the TM_{010} mode are

$$E_z(\rho,t) = E_0 J_0(\frac{4.81}{D}) \; e^{-i\omega t} \tag{3.14}$$

$$B_\phi(\rho,t) = -i E_0 J_1(\frac{4.81\rho}{D}) \; e^{-i\omega t} \tag{3.15}$$

where ρ, ϕ, and z are the standard cylindrical coordinates. With the fields known, it is possible to calculate the stored energy U. Noting the periodic time dependence and assuming the unperturbed dielectric constant to be unity

$$U = \frac{1}{16\pi} \int_{cavity} |E_z(\rho,t)|^2 + |B_\phi(\rho,t)|^2 \; d \, vol \tag{3.16}$$

$$U = \frac{E_0^2}{8} \; L \int_0^{D/2} [J_0^2(\frac{4.81}{D}\rho) + J_1^2(\frac{4.81\rho}{D})]\rho \; d\rho \tag{3.17}$$

$$U = 0.0084 \; (D^2 L) \; E_0^2 \tag{3.18}$$

Note that U has the desired E_0^2 dependence. For the values of D and L described above
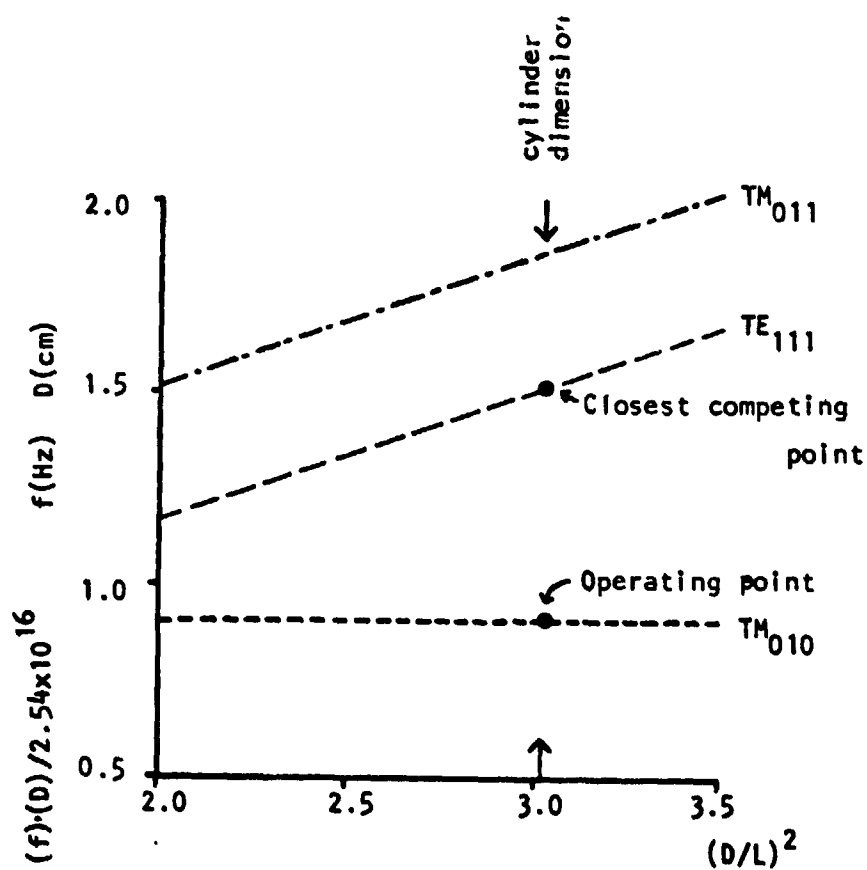
Figure 3.4 Mode chart for right circular cylinder showing the TM_{010} operating point and the closest competing point.

$$U = 0.048 \, E_0^2 \qquad\qquad (3.19)$$

Therefore

$$\sigma_a = \frac{0.048 \, \omega \, E_0^2}{\frac{c}{8\pi} E_0^2} \; \frac{1}{Q_d} \;=\; 0.048 \, \frac{f}{Q_d} \; (cm^2) \qquad (3.20)$$

The absorption cross-section is simply proportional to the product of f and $1/Q_d$.

3.2.2   Experimental Set-Up

The microwave circuit used to measure cavity Q is shown in Figure 3.5.   Power was generated by an X-band sweep oscillator which varied frequency linearly over a specified range near the resonant frequency.   Power was transmitted through a variable attenuator and by a commercial wavemeter to provide a frequency reference.   The cavity was connected to the circuit via a short stub to a coaxial tee. The coax coupled magnetically into the cavity fields by a loop oriented in the ϕ direction located on one of the end plates.   The tee was connected to the rest of the circuit by flexible coaxial cable.   This allowed the entire cavity assembly to be placed in a cold box.   The cable was terminated at both ends by matched attenuators in order to reduce reflections.

After passing the cavity, power was measured by a crystal detector. The crystal had been calibrated previously against a bolometer.   The output of the crystal went to a digital scope.   The scope was triggered by the sweeper and had the capability to store traces on floppy
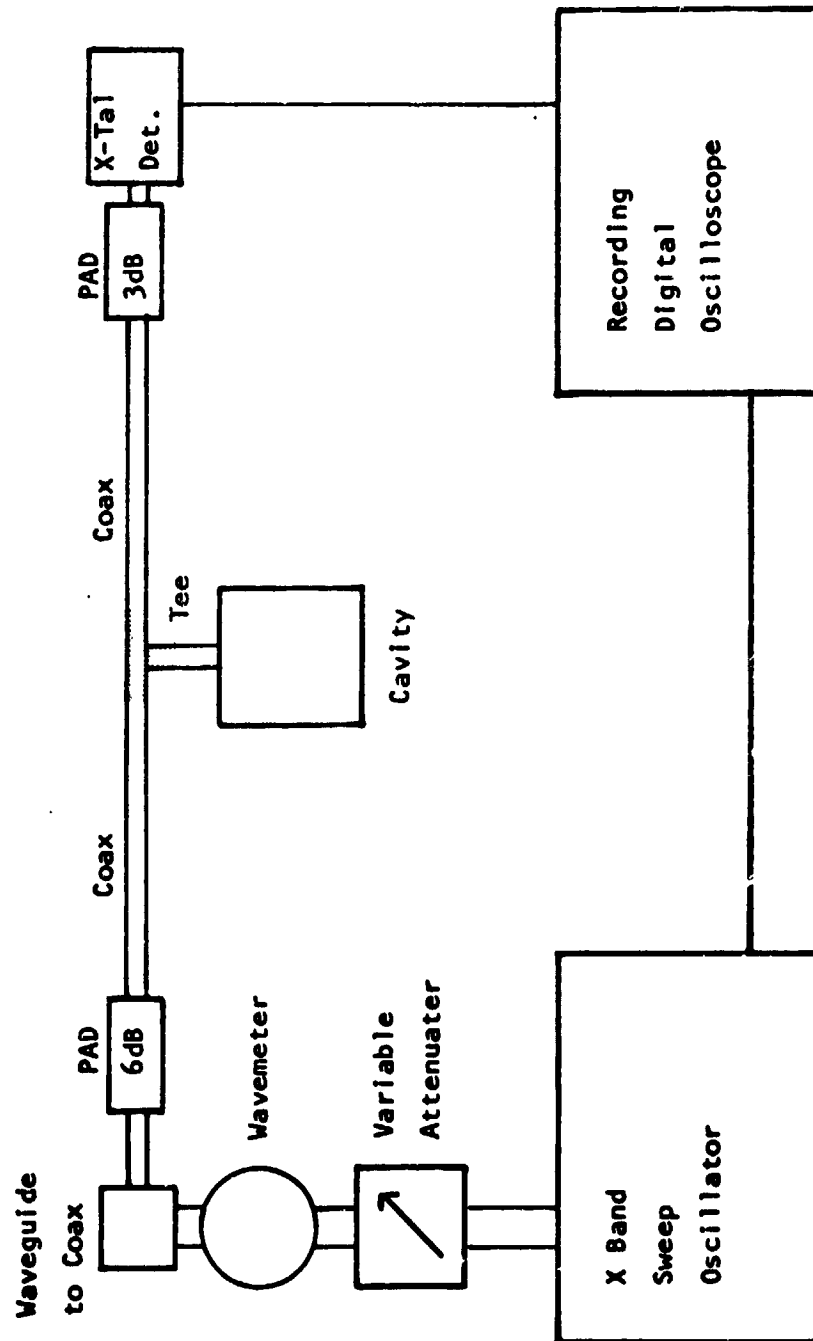
Figure 3.5 Microwave circuit for Q measurement

disks for later analysis. This feature was used when measuring time-dependent phenomena, such as melting effects.

In Figure 3.6 a typical scope trace of crystal voltage versus time or, equivalently, frequency, is shown. The reference marker and the cavity resonance are visible. When the frequency is off resonance, no power is absorbed by the cavity and the power to the crystal is at a maximum. On resonance the cavity is very absorptive and the crystal power is at its minimum. The loaded Q of the cavity, which includes coupling effects, is

$$Q_L = \frac{f_0}{\Gamma} \tag{3.21}$$

where f_0 is the resonant frequency and Γ is the full width at half maximum of the resonance. The cavity Q discussed previously is the unloaded Q which is related to Q_L for a circuit such as this by

$$Q_0 = \sqrt{\frac{P_{max}}{P_{min}}} \; Q_L = \sqrt{\frac{P_{max}}{P_{min}}} \; \frac{f_0}{\Gamma} \tag{3.22}$$

where P_{max} and P_{min} are the maximum and the minimum powers received by the crystal.[37]

The actual cavity assembly used in the experiment is shown in Figure 3.7. It was machined out of 1.5 inch copper rod. The cavity diameter D was 2.153 cm and the cavity length L was 1.229 cm. One end plate was removable for cavity cleaning and polishing. There were holes drilled on axis in each of the 1.5-cm-thick end plates with a 2 mm radius to provide access for drop insertion. The cavity was

Figure 3.6
TYPICAL SCOPE TRACE
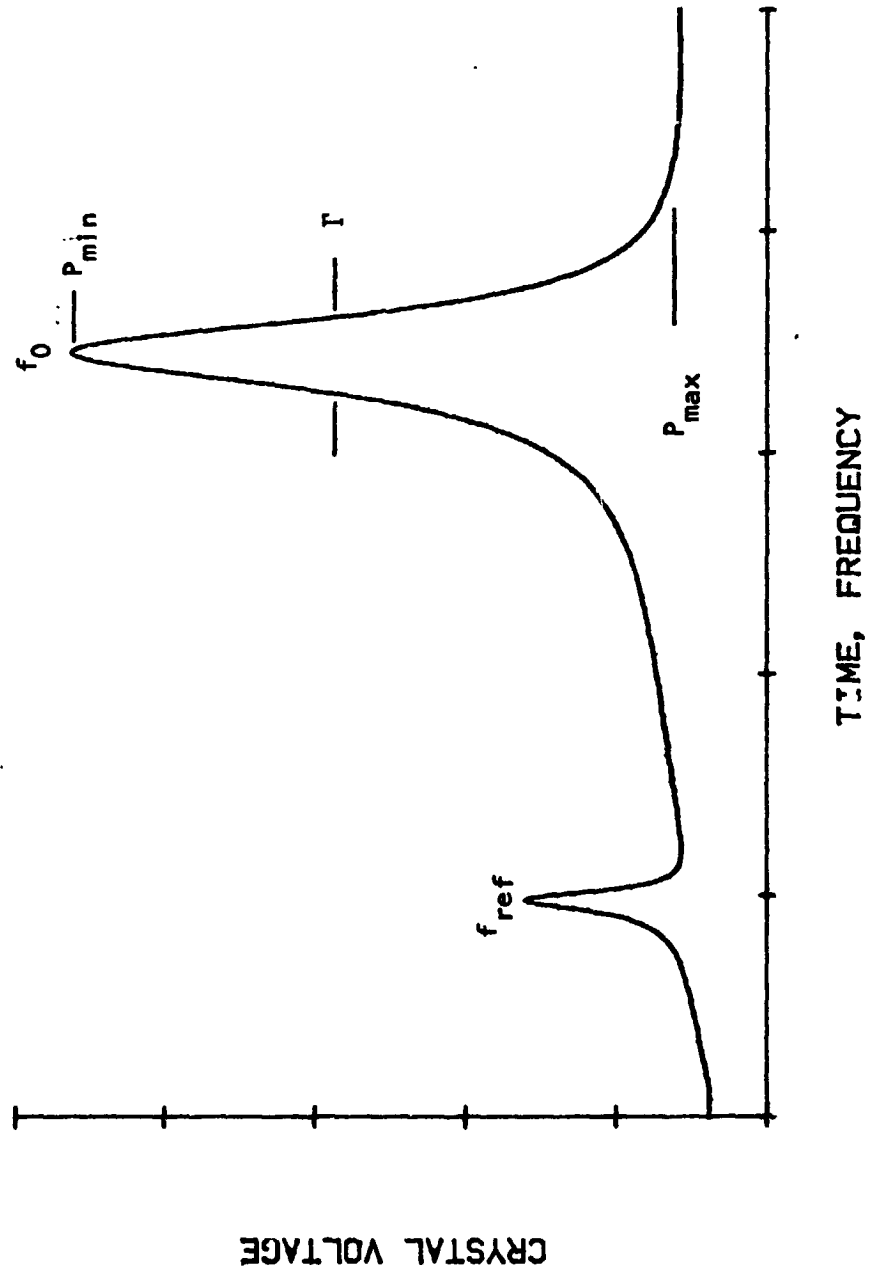
Figure 3.7   Resonant Cavity Assembly.

supported horizontally on a vee block in direct contact with a
thermometer to measure cavity temperature.

Drops of distilled water were supported by surface tension on a
quartz fiber with a radius less than .1 mm.   An example is shown in
Figure 3.8.   Drops were placed on the fiber by a syringe and dimensions
were measured in situ by a direct-read measuring microscope.   The fiber
was oriented along the z-axis of the cavity and ran through the holes
in the end plates.   It was held on axis by plexiglass supports on
either end of the cavity.   The entire cavity assembly was portable so
that it could be moved in and out of a -20°C cold box without disturbing
the drop or the microwave circuit.   Typical cooling and warming curves
are shown in Figure 3.9.

The resonant frequency and Q of the empty cavity were measured.
The resonant frequency was 10.65 GHz and the Q was 8990, which are
very close to the design values of 10.66 GHz and 9000.   The differences
are attributed to the end plate holes and imperfect cavity surfaces.
It should be noted that the empty Q varied somewhat due to oxidation
on the interior cavity surfaces, resulting from exposure to moisture
and the thermal cycling of the cavity.   In order to correct for this,
the cavity was polished periodically and the empty Q was measured
prior to each drop run.

3.3   Experimental Results

The experimental results of absorption measurements for water drops
are presented in this section.   The measured cross-sections for room-
temperature drops are found to agree with the Rayleigh values in
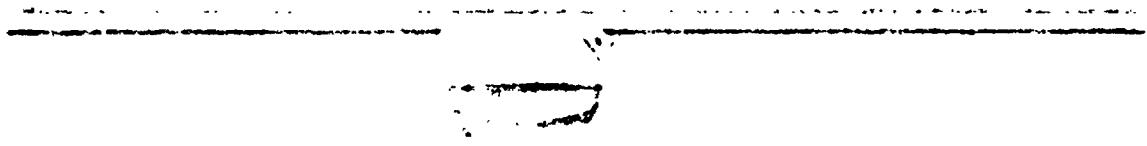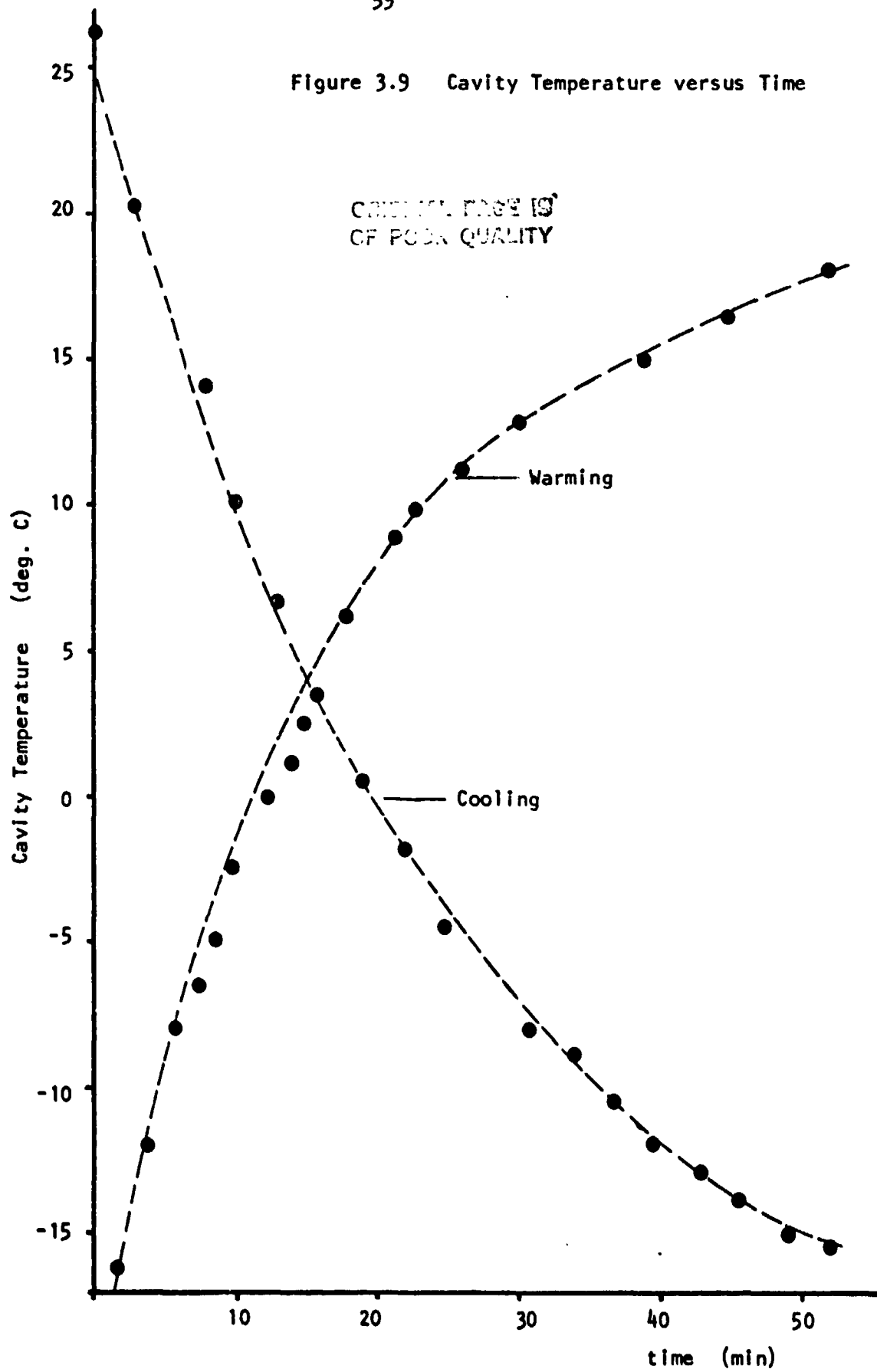
Figure 3.8   Water droplet supported on a quartz fiber.

Figure 3.9   Cavity Temperature versus Time

Section 3.3.1.   In Section 3.3.2 some measurements of the dielectric

constant for supercooled water are presented.   Finally, Section 3.3.3

contains absorption data for spherical and non-spherical hydrometers

during melting and freezing.

3.3.1   Absorption Cross-Sections for Warm Drops

Absorption cross-sections were measured for distilled water

drops at a room temperature of 20°C using the techniques described in

Section 3.2.   The resonant frequency of measurement was 10.64 GHz

$\pm$ .01 GHz.   Drops with diameters varying from 0.5 mm to 2.0 mm were

measured.   The measured absorption cross-section is plotted against

drop volume V in Figure 3.10.   The straight line is a plot of the

Rayleigh absorption cross-sections

$$\sigma_a = \frac{6\pi V}{\lambda} \; \text{Im}(-K) \tag{3.23}$$

with Im(-K) taken from Ryde[17] at 20°C to be 0.01883.   The data agrees

well with Rayleigh theory for these small essentially-spherical drops.

The scatter in the data is mainly attributed to uncertainty in

measurement of V.

3.3.2   Dielectric Parameters of Supercooled Water

With the confidence in the measurements of Rayleigh absorption

cross-sections gained from the results of Section 3.3.1, measurements

were made of σ_a as a function of cavity temperature T   in order

to infer the dielectric parameter Im(-K)   from the Rayleigh

cross-sections in equation 3.23.   Measurements of $|K|^2$, which can be

Figure 3.10   Absorption cross-section versus volume for warm (20°C) drops.
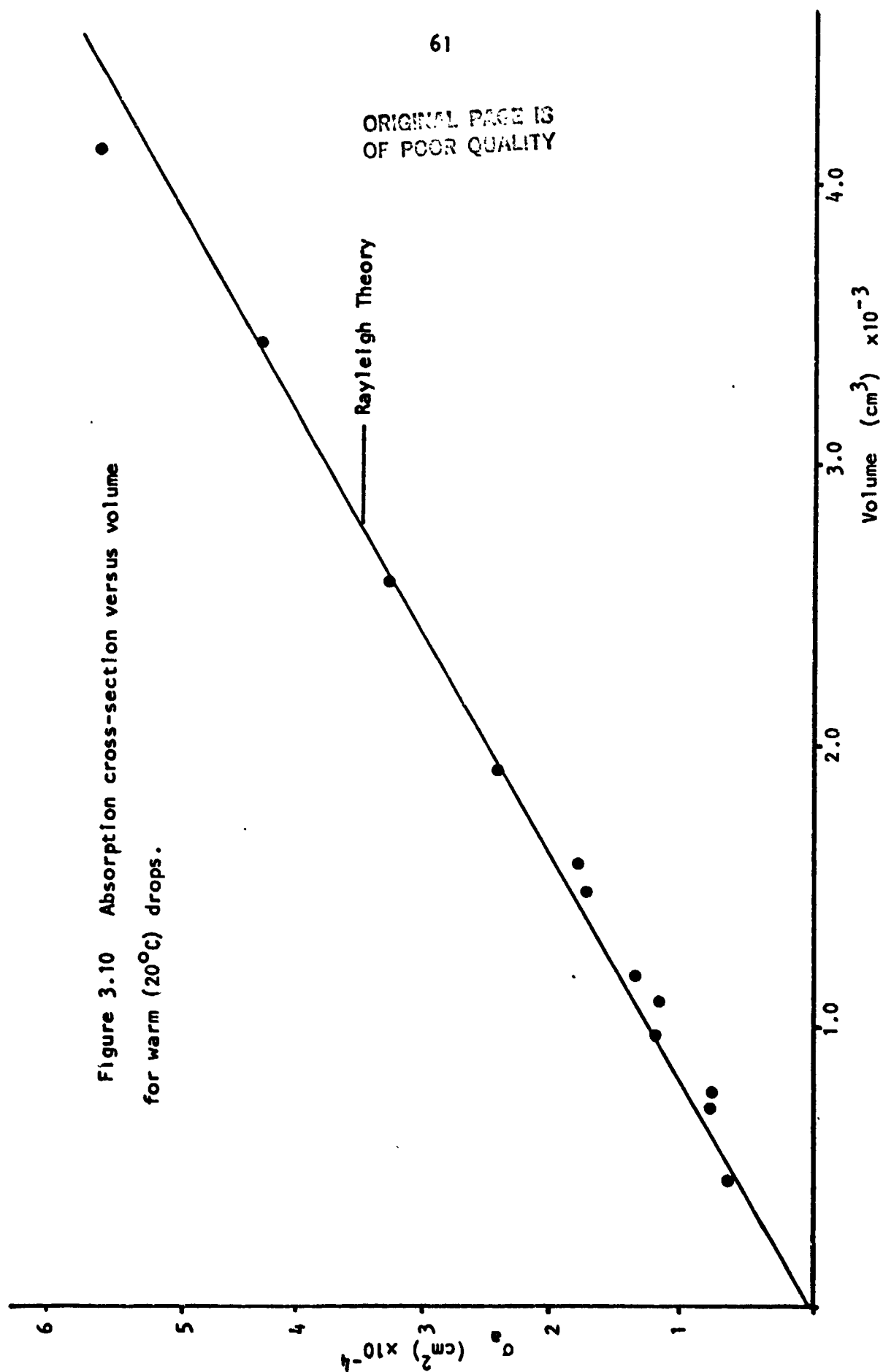
linearly related to the shift in the resonant frequency f_0 by perturbation theory, were also attempted. Measurements of $|K|^2$, however, were unsuccessful because the very small changes in $|K|^2$ with temperature were masked by relatively large changes in the resonance frequency due to thermal expansion of the cavity. Lack of $|K|^2$ measurement is not considered too important as, in applications, $|K|^2$ is generally assumed to be constant with temperature.

Measurements of the supercooled temperature dependence of $Im(-K)$ were made by inserting distilled water drops in a warm cavity and placing the cavity assembly in the $-20^{\circ}C$ cold box. The drops were assumed to remain in thermal equilibrium with the cavity. Microwave heating of the drop was neglected because of the low power of the sweeper (less than 1 mW) and the low duty cycle on resonance (less than 0.001). Liquid drops were observed at temperatures as low as $-17^{\circ}C$ before crystallization.

Values of $1/Q_d$ and cavity temperature T versus time for a typical cooling run are shown in Figure 3.11. The drop cooled with increasing absorption to $-17^{\circ}C$ where it nucleated and the absorption dropped to the value for ice. At 16 minutes into the run there was a sudden jump in $1/Q_d$ which lasted for 12 minutes. Similar jumps were observed on subsequent runs, although occurring at slightly different times and temperatures. These anomalously-high values of $1/Q_d$ are not thought to be physically related to changes in $Im(-K)$, but rather to some thermal effect in the microwave circuit. In the following, therefore, such values will be omitted.

Figure 3.12 is a plot of the observed values of $Im(-K)$ as
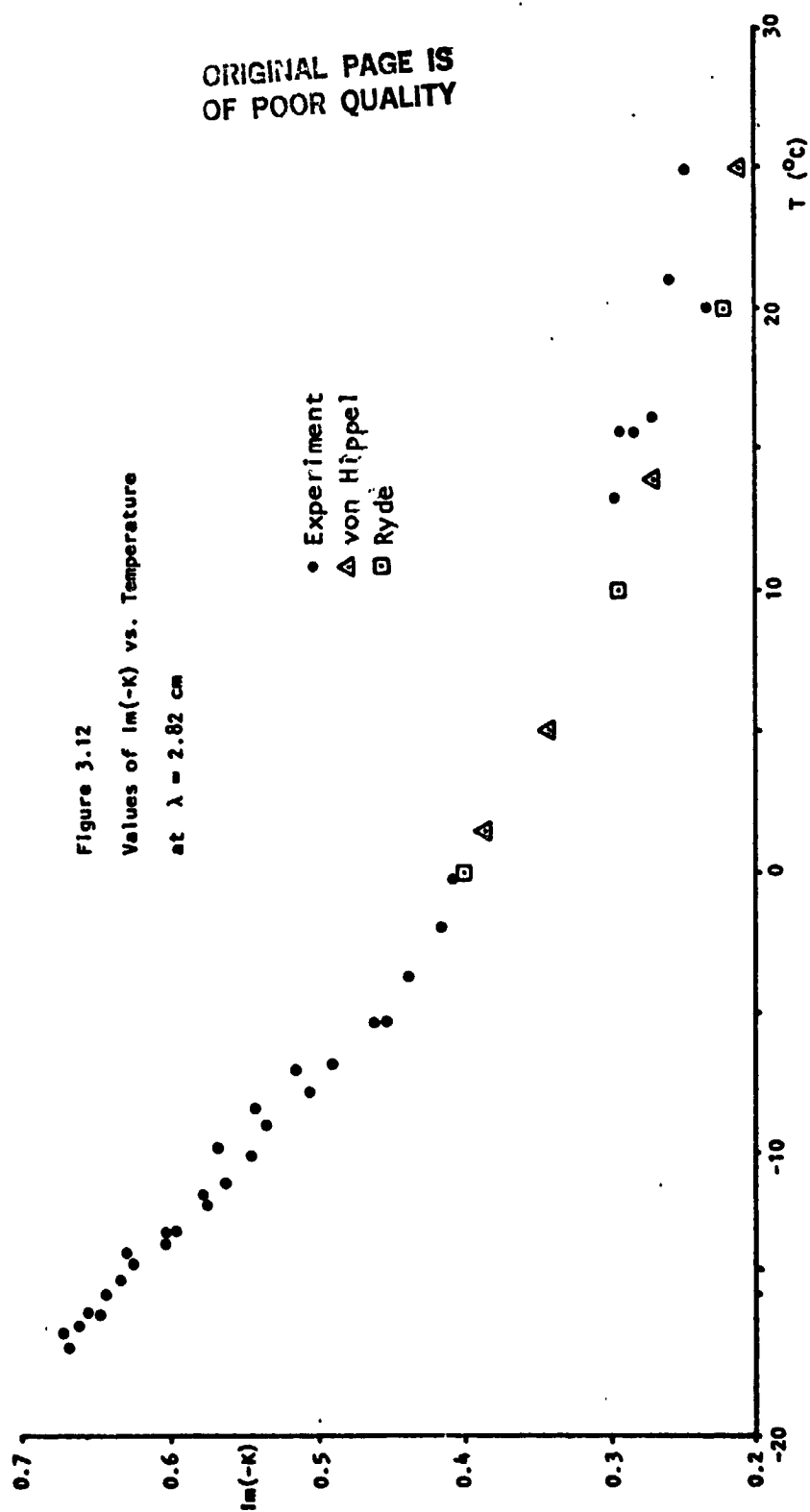
Figure 3.11 Temperature and $1/Q_d$ versus time for cooling spherical drop.
$D_{eq} = 1.6mm$
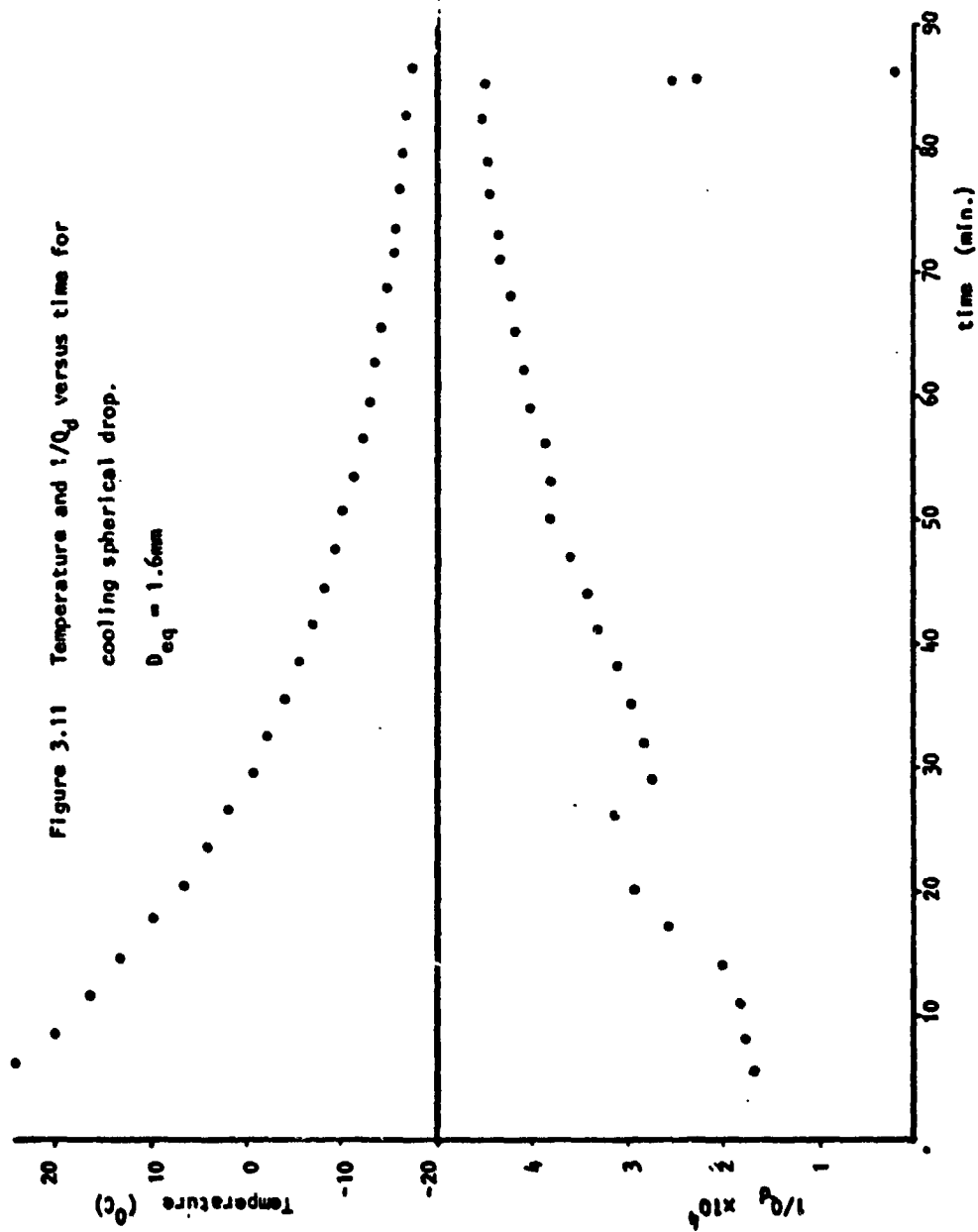
Figure 3.12

Values of Im(-K) vs. Temperature

at λ = 2.82 cm

ORIGINAL PAGE IS
OF POOR QUALITY

• Experiment
△ von Hippel
▢ Ryde

calculated by equation 3.22, along with the values of $Im(-K)$ calculated from the dielectric data of von Hippel[16] and Ryde.[17] The measured data is a fairly smooth fit to the previous values and extends well into the supercooled range. The real and imaginary parts of the dielectric constant could be calculated from $Im(-K)$ by assuming $|K|^2$ is constant with its value for $0^{\circ}C$. The above technique could be used to measure $Im(-K)$ at even lower temperatures if a very clean cold box environment was maintained. Values at other frequencies could be measured if a suitable cavity was constructed.

3.3.3   Absorption Cross-Sections During Phase Transition

In Figure 3.11 of the previous section, a supercooled drop is observed to crystallize. The value of $1/Q_d$ dropped linearly in time from a value for liquid water to that of ice in less than 1 minute. This is the behavior predicted in Section 3.1 for a freezing supercooled drop. The melting behavior of ice particles is expected to be more complicated.

Observations of the melting cross-sections were made by placing an ice particle onto the fiber and into the cavity while the cavity was in thermal equilibrium with the cold box at $-20^{\circ}C$. The cavity assembly was then removed from the cold box and allowed to warm. A typical example of the behavior of $1/Q_d$ with time is shown in Figure 3.13 for an ice sphere of equivalent melted diameter D_{eq} of 1.15 mm. The absorption behaved qualitatively as was predicted in Section 3.1. At 12:30 minutes the drop began to melt. The value of $1/Q_d$ quicly rose to a maximum at 16 minutes. The absorption then

Figure 3.13 $1/\alpha_d$ versus time for melting spherical drop.

$D_{eq} = 1.15mm$
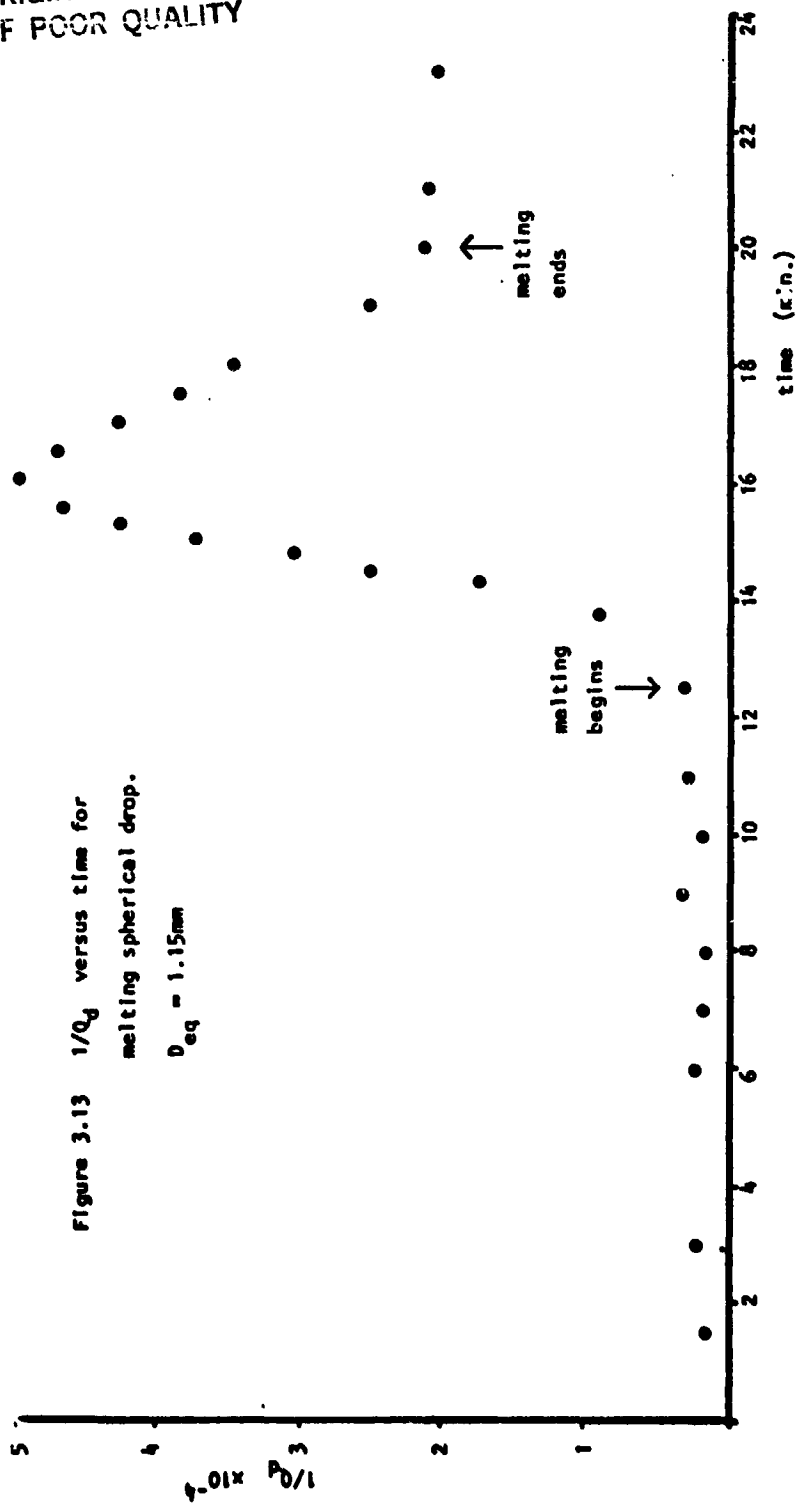
began to decay and at 20 minutes reached the melted value, which was less than half the peak value.

In order to quantitatively compare the measurements with theory, $1/Q_d$ must be converted to the normalized cross-section $\frac{\sigma_a}{\sigma_{melted}}$ and some relation must be assumed between time and the mass fraction

$$f_w = \frac{M_w}{M_w + M_i} \qquad (3.24)$$

To relate f_w to time T, assume that the droplet temperature is zero during melting. Also assume that melting begins at time t_0 and ends at time t_f. The heat loss from the drop is

$$\frac{dQ}{dt} = \text{const. } T(t) \qquad (3.25)$$

where $T(t)$ is the time-dependent cavity temperature and the constant is dependent only on the cavity geometry. From the warming curve in Figure 3.9, it is assumed that the cavity temperature increases linearly with time near zero. Therefore

$$\frac{dQ}{dt} = \text{const. } t \qquad (3.26)$$

The change in water mass can be related to the heat loss by the latent heat of fusion L_{iw}.

$$\frac{dM_w}{dt} = \frac{1}{L_{iw}} \frac{dQ}{dt} \qquad (3.27)$$

Since the total mass $M_w + M_i$ is constant and noting that $M_w = 0$ at time t_0

$$f_w(t) = \frac{M_w(t)}{M_w + M_i} = const. \int_0^t (t - t_0)\, d(t - t_0) \qquad (3.28)$$

$$f_w(t) = const.\,(t - t_0)^2 \qquad (3.29)$$

Noting that $f_w = 1$ at time $t = t_f$, then

$$f_w(t) = \frac{(t - t_0)^2}{(t_f - t_0)^2} \qquad (3.30)$$

which is the required relation between mass fraction and time.

Figures 3.14, 3.15 and 3.16 show the experimental and theoretical normalized cross-sections $\dfrac{\sigma_a}{\sigma_{a\,melted}}$ as functions of f_w for ice spheres equivalent melted diameters D_{eq} of 1.15, 1.6 and 2.0 mm. The general behavior is in good agreement with theory, although the theory underestimates the absorption cross-sections by as much as 25% at peak value in the worst case. The discrepancy is due to the fact that the Aden and Kerker theory assumes dielectric values for water on a wavelength of 3 cm and a temperature of $18^{\circ}C$. The dielectric constant at these values is less absorptive than the actual experimental conditions of 2.8 cm and $0^{\circ}C$. The increased absorption, along with slight deviations from sphericity, could account for the observed difference.

The absorption cross-sections for melting non-spherical ice particles were observed, to check for the multiple phase behavior predicted in Section 3.1.2. Shaped ice particles were constructed by

69

Figure 3.14 Normalized absorption cross-section versus mass fraction.

$D_{eq} = 1.15mm$
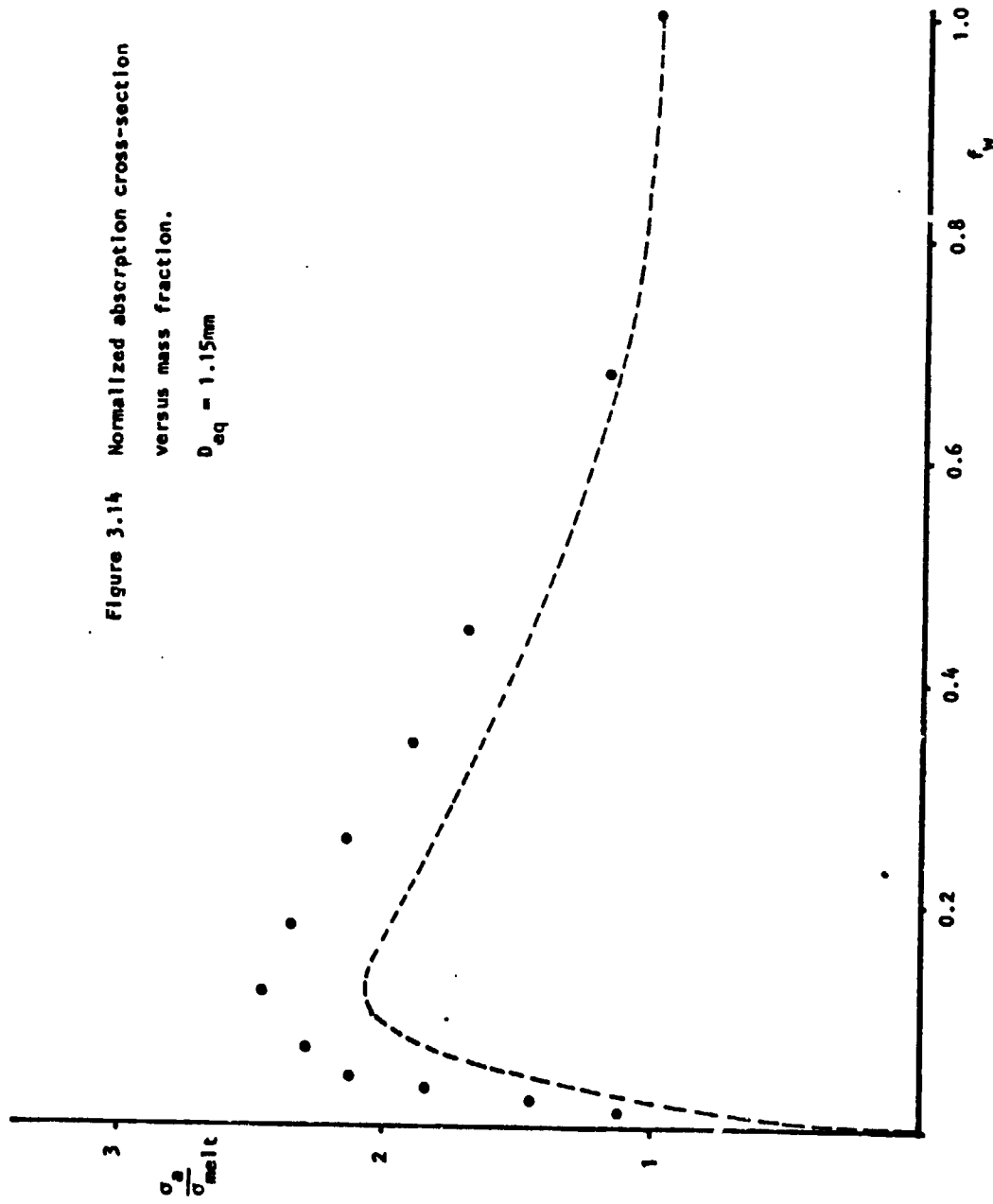
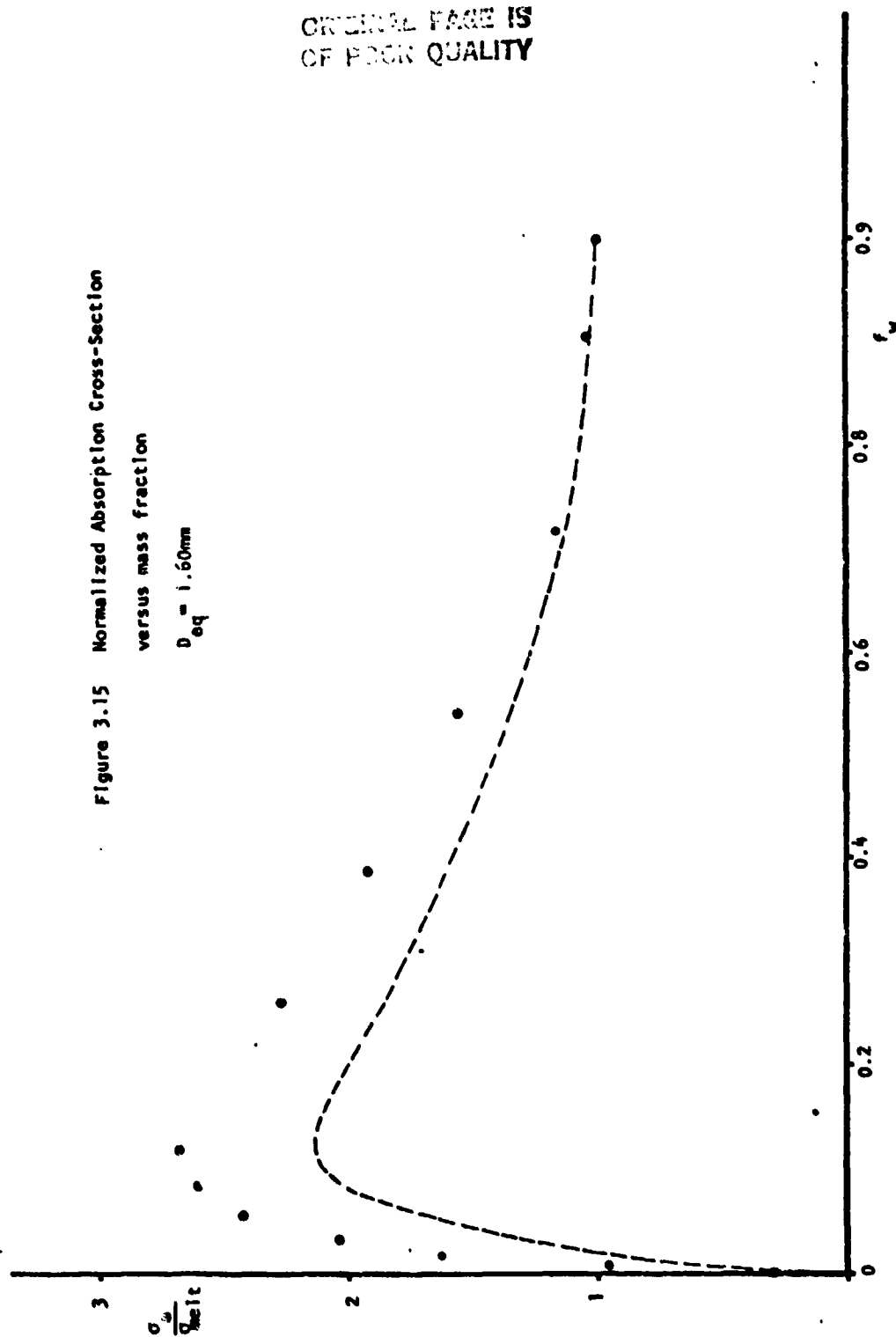Figure 3.15 Normalized Absorption Cross-Section

versus mass fraction

$D_{eq} = 1.60mm$

Figure 3.16 Normalized absorption cross-section
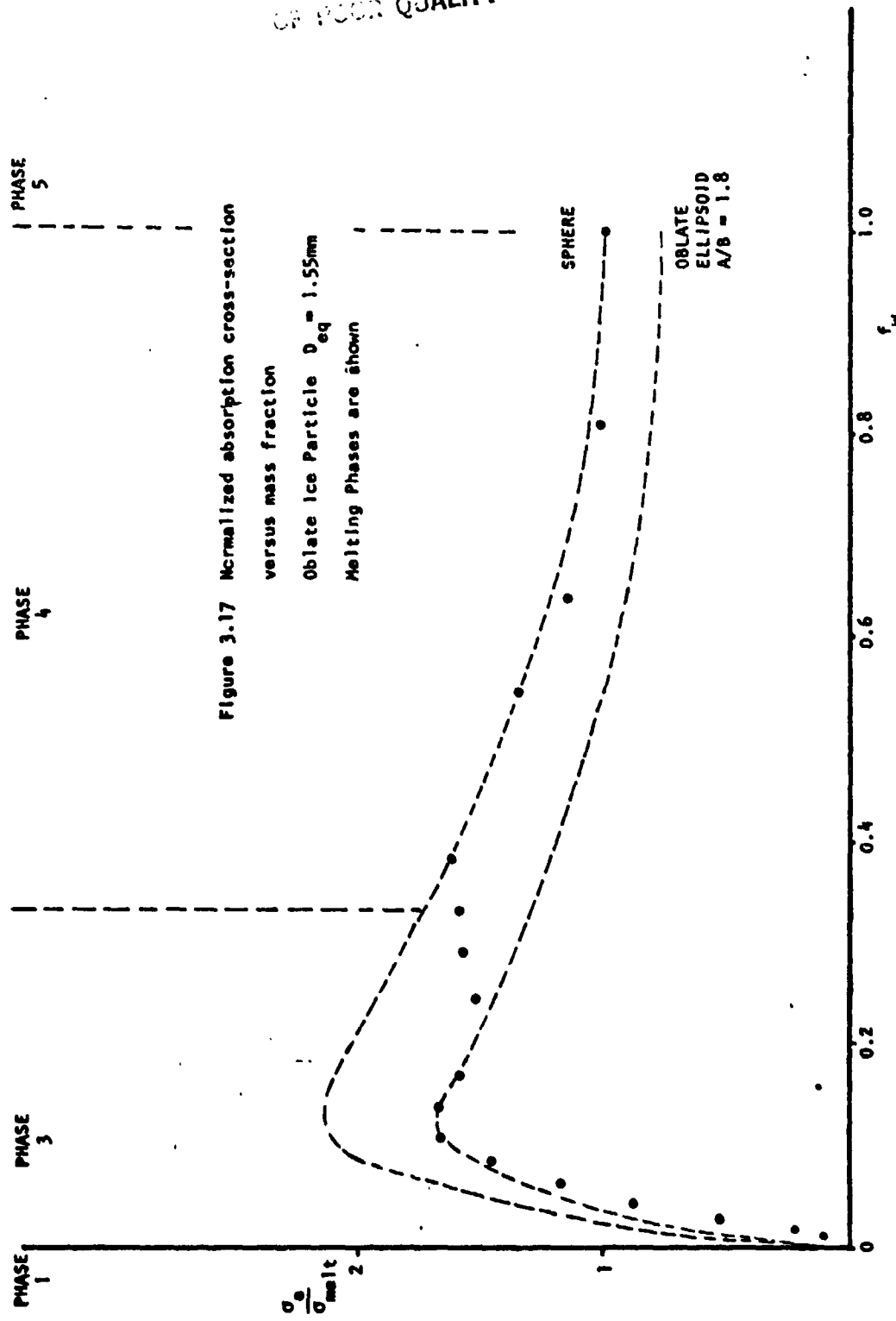versus mass fraction

$D_{eq} = 2.00mm$
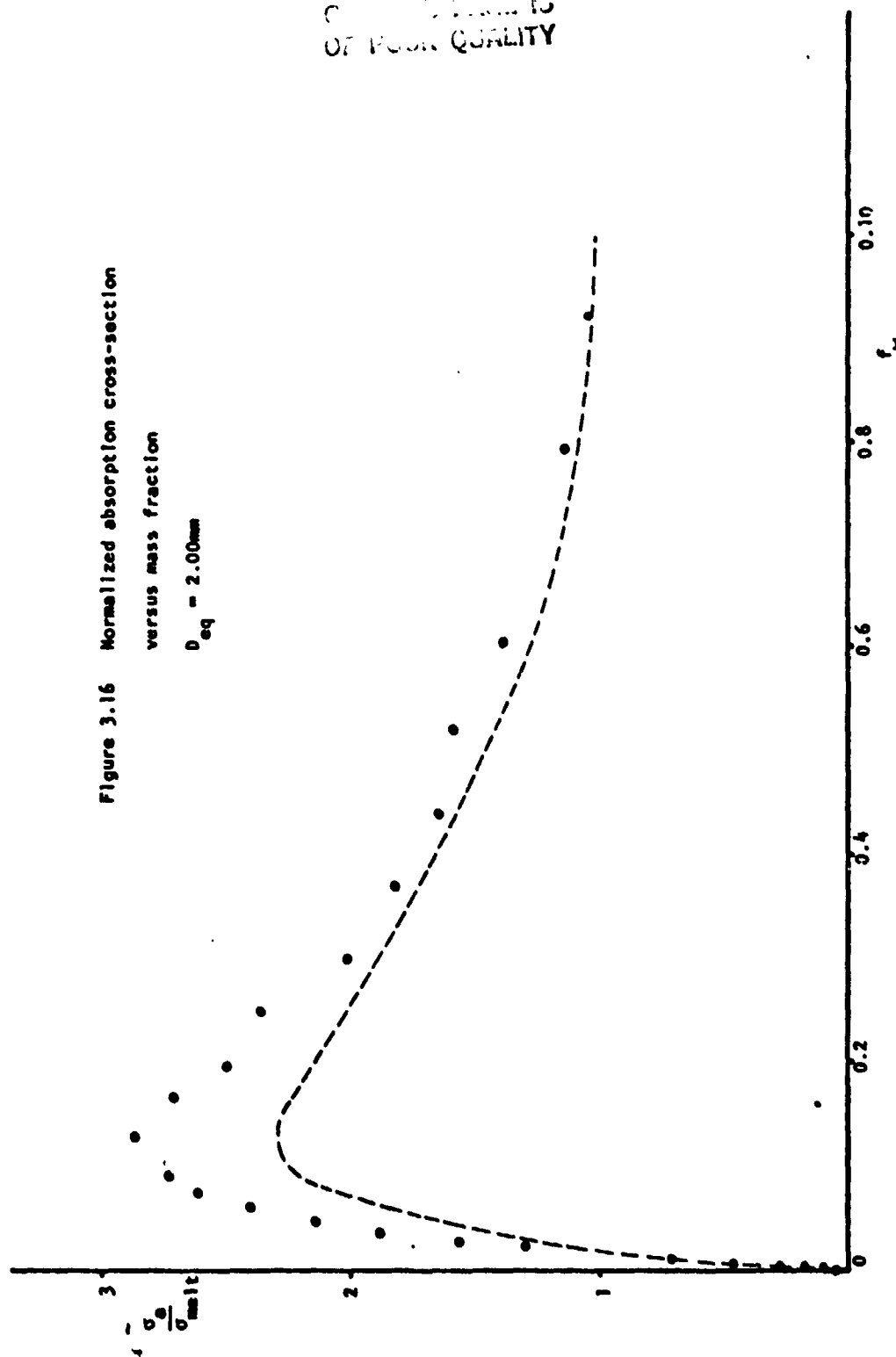
placing a small water drop on a fiber and immersing the drop in a liquid nitrogen bath. After the drop froze, it was removed from the bath and an additional drop was added. The procedure was repeated until the required shape was achieved. The major disadvantage of this method was the inability to create sharp edges due to surface tension smoothing of the water drops.

Figures 3.17 and 3.18 show examples of ice particles which were roughly oblate and prolate ellipsoids oriented with their axis of revolution along the electric field. For the oblate case in Figure 3.17, four of the five melting phases are visible. The absorption cross-section started in Phase 1 like that of an ice sphere. Once melting began, the cross-section skipped Phase 2 because of the relatively smooth surface and absorbed in Phase 3 like an oblate water-coated ice ellipsoid with axes ratio $A/B = 1.8$. At a mass fraction of 0.2, the drop began to collapse into Phase 4 of a water-coated ice sphere and at a mass fraction of 1.0 the drop absorbed like a water sphere in Phase 5.

In Figure 3.18 an example of a prolate ellipsoid is shown (note the change in scale). In this case there was sufficient surface irregularity to show a non-uniform melting Phase 2 up to a mass fraction of approximately 0.2 where the very strong absorption, in Phase 3, of an oriented prolate ellipsoid with $A/B = 2.5$ prevailed. Phase 3 lasted up to a mass fraction of 0.6 which is artificially high due to the structural support of the quartz fiber. Above $f_w = 0.6$ the drop collapsed into the spherical shape of Phases 4 and 5.

Figure 3.17 Normalized absorption cross-section

versus mass fraction

Oblate Ice Particle D_{eq} = 1.55mm

Melting Phases are shown

Figure 3.18 Normalized absorption cross-section versus mass fraction. Prolate ice Particle $D_{eq} = 1.4mm$ Melting Phases are shown. (note change in scale)
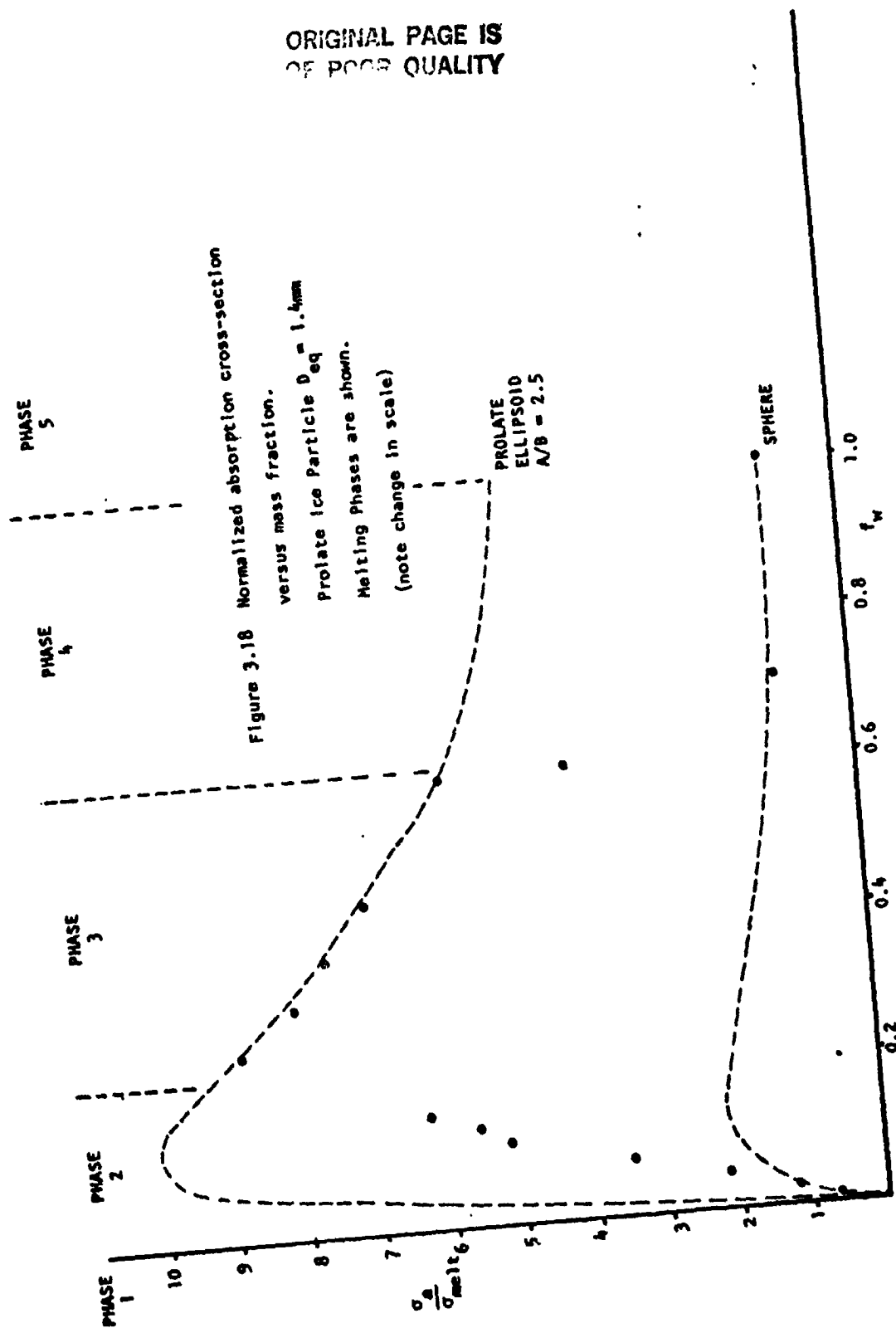
In conclusion, the experimental measurements of the absorption cross-sections seem to support the theory for water-coated ice spheres and ellipsoids and the model for atmospheric melting. The observed cross-sections were found to be greater than or equal to the theoretical values for water-coated ice spheres. The greatest differences occurred at the peak of the melting curve, where for one case the theoretical cross-section underestimated the measured value by 25%. The difference is thought to be the result of discrepancies between the theoretical and experimental values of the dielectric constant.

CHAPTER 4

HYDRODYNAMICS OF ACCELERATED DROPS

The absorption and scattering cross-sections of water drops were shown, in Chapters 2 and 3, to be strong functions of droplet shape. In order to accurately predict cross-sections, therefore, it is necessary to have some model of the expected droplet shape. The Cloud Physics community has done a great deal of theoretical and experimental work on droplet shape and break-up in the quasi-steady-state case of drops falling in the earth's gravitational field.[38-46] In Section 4.1 this work is briefly reviewed and the generalization to accelerated drops is made.

In Section 4.2 experimental techniques, employing high-speed photography, for measuring droplet shapes and velocities in the wind tunnel, are discussed. In Section 4.3 the results of experiments on drop deformation and stability are discussed.

4.1   Hydrodynamic Theory of Water Drops

For very small water droplets, where surface tension is the dominant surface force, the droplets assume a spherical shape. Section 4.1.1 discusses deformations from spherical shape as a result of hydrodynamic acceleration of the droplets by another fluid. Section 4.1.2 presents the oscillations which result from the restoring nature of the surface tension. Finally, in Section 4.1.3 the instabilities which arise when the surface tension is no longer sufficient to maintain the drop are presented.

4.1.1   Drop Deformation

The steady-state shape of a water drop being accelerated hydrodynamically by another fluid, in this case air, can, in principle, be found by balancing all forces acting on the surface.   These forces are:

> Surface tension
>
> Centrifugal force from internal circulation of the water
>
> > inside the drop
>
> Aerodynamic force from air flowing around the drop
>
> Hydrostatic pressure gradient within the drop resulting
>
> > from acceleration

Investigators have attempted to model droplets by including surface tension with different combinations of the above forces.[38-42]   The most complete, although reasonably complicated, method was that of Purppacher and Piter in 1970.[38]   They included each of the above forces, either analytically or semi-empirically, into Fourier expansion coefficients in elevation angle detailing the change in radius of the drop.   The results agreed well for quiescent freely-falling drops with equivalent diameter D_{eq} less than 5 mm with the experimental results of Pruppacher and Beard,[39] including such second-order effects as the dimple observed on the bottom of large drops.   For drops larger than 5 mm, the Pruppacher and Piter model underestimates the deformation somewhat.

If it is sufficient to approximate the deformed drop as an oblate ellipsoid, which is certainly adequate for calculations of Gans absorption and scattering cross-sections, then the simpler approach of

Green[46] provides accuracy equivalent to that of Pruppacher and Piter.
Green's approach, in 1975, was to neglect flow effects altogether and
include only the surface tension and hydrostatic forces.   Using this
approach, the diameter of an equivolumetric sphere D_e can be written
in terms of the major-to-minor axis ratio A/B of the ellipsoid and the
acceleration a as

$$\left(\frac{a}{g}\right)^{1/2} D_{eq} = \left(\frac{4\sigma}{g\rho_w}\right)^{1/2} \frac{[(A/B)^2 - 2(A/B)^{1/3} + 1]^{1/2}}{(A/B)^{-1/6}} \tag{4.1}$$

where g is the acceleration due to gravity, σ is the surface
tension (n.b., σ is also used to denote cross-sections), ρ_w is the
density of water and a/g is the acceleration of the drop in g units.
Green originally assumed that the drops were falling at terminal
velocity and therefore a/g was unity.   The more general case for any
quasi-steady-state acceleration is included here.   Equation 4.1 is
plotted in Figure 4.1 for water at 20°C.

4.1.2   Drop Oscillations

When drops are perturbed from their equilibrium shape, surface
tension acts as a restoring force.   This restoring force results in
drop oscillations.   The oscillations can be characterized by a discrete
set of normal modes.   These modes were first identified by Rayleigh,
who identified the allowed frequencies for a sphere as [6,47]

$$f_n = \left[\frac{2n(n-1)(n+2)\sigma}{\pi^2 \rho_w D_{eq}^3}\right]^{1/2} \tag{4.2}$$

Figure 4.1 Axis ratio versus equivalent accelerated diameter at 20°C from Green.

ORIGINAL PAGE IS
OF POOR QUALITY
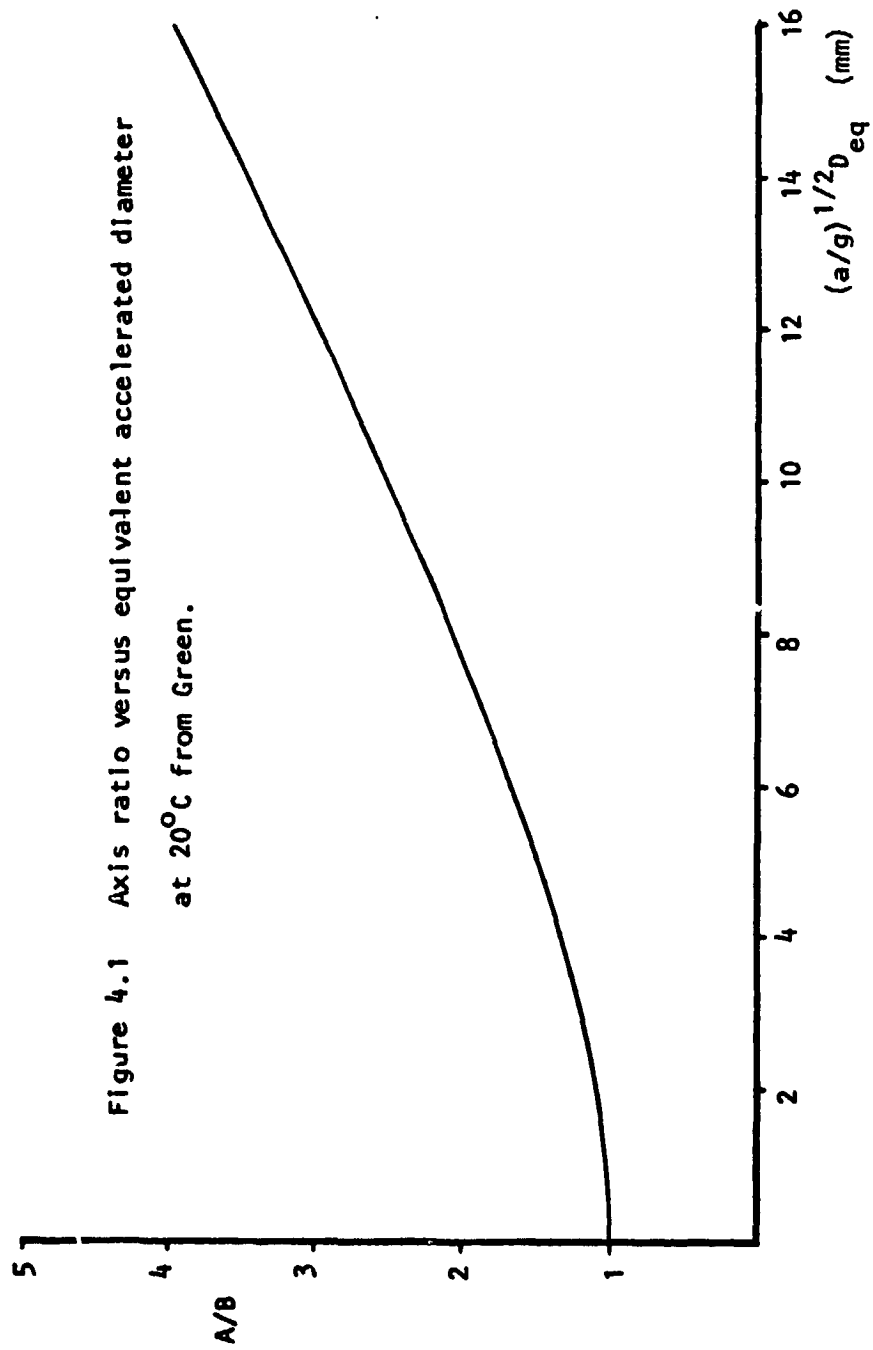
where n is the mode number.   The fundamental mode is n = 2 with a frequency

$$f_2 = [\frac{16\sigma}{\pi^2 \rho_w D_{eq}^3}]^{1/2} \qquad (4.3)$$

The fundamental frequency is plotted against D_{eq} in Figure 4.2 for millimeter-size drops.

In the fundamental mode the drop is flattened along one axis initially.   A quarter-cycle later, the drop is spherical.   After one-half of a cycle, the drop is flattened along an axis perpendicular to the original.   At three-quarters of a cycle, the drop is again spherical, and after one full cycle the drop is back to its original shape.

The validity of the steady-state drop deformations described in Section 4.1.1 after a change in acceleration is related to the fundamental frequency in equation 4.3.   For time scales less than one fundamental period $1/f_2$ the steady-state behavior will not accurately predict the transient drop deformation.   For time scales of several periods the steady-state behavior will be the average deformation in time.   After many oscillations, viscous damping will cause the oscillations to decay and the drop deformation will be accurately determined by the steady-state solution.

It is instructive to consider the possible effect on the backscatter cross-section of the fundamental oscillation.   The change in drop shape will cause a change in the backscatter cross-section via the Gans theory.   The cross-section will oscillate at the frequency of the

Figure 4.2

Fundamental oscillation frequency

versus D_{eq}.
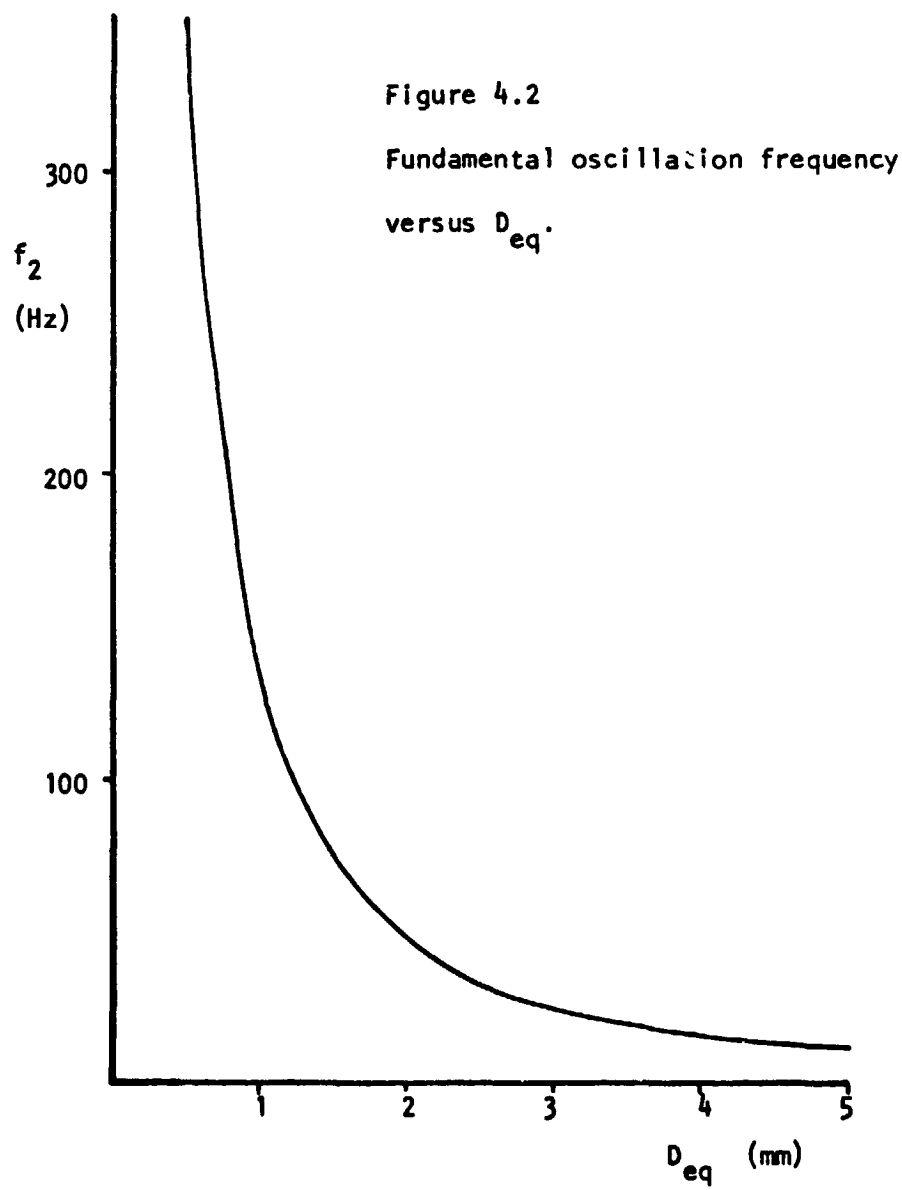
drop oscillation. An example of a periodic axis ratio A/B and the resulting backscatter cross-section σ_b is shown in Figure 4.3.

The oscillation of σ_b is a potential source of doppler noise in meteorological doppler radar. The σ_b oscillation results in sidebands shifted by $^\pm f_2$, as is shown in Figure 4.4. This is a source of confusion in that f_2 is of the same order as the doppler shift from particles moving at meteorological velocities. These false sideband signals could cause a broadening in the velocity distribution function observed in conditions, such as turbulence, which could excite drop oscillations.

4.1.3 Instability and Drop Break-Up

In the previous section it was indicated that surface tension is the primary restoring force maintaining droplet equilibrium. When other forces, such as the hydrostatic pressure resulting from aerodynamic acceleration by another fluid, becomes comparable to the surface tension, then the possibility of droplet instability and break-up must be considered. Drop break- p is important to models of atmospheric precipitation as a limit on the maximum size of drops and, as Langmuir pointed out,[48] that the small droplets resulting from break-up are a major source of condensation nuclei in warm rain.

Observations of drop break-up have been made by Mathews and Mason[49] and others[50] on drops falling at terminal velocity. Drops were stable in their roughly-oblate shape until they reached a certain critical base diameter, where a small concave depression in the base deepened until the resulting bag-like shape eventually burst. This

Figure 4.3   Axis ratio and backscattered power
from oscillating drop.
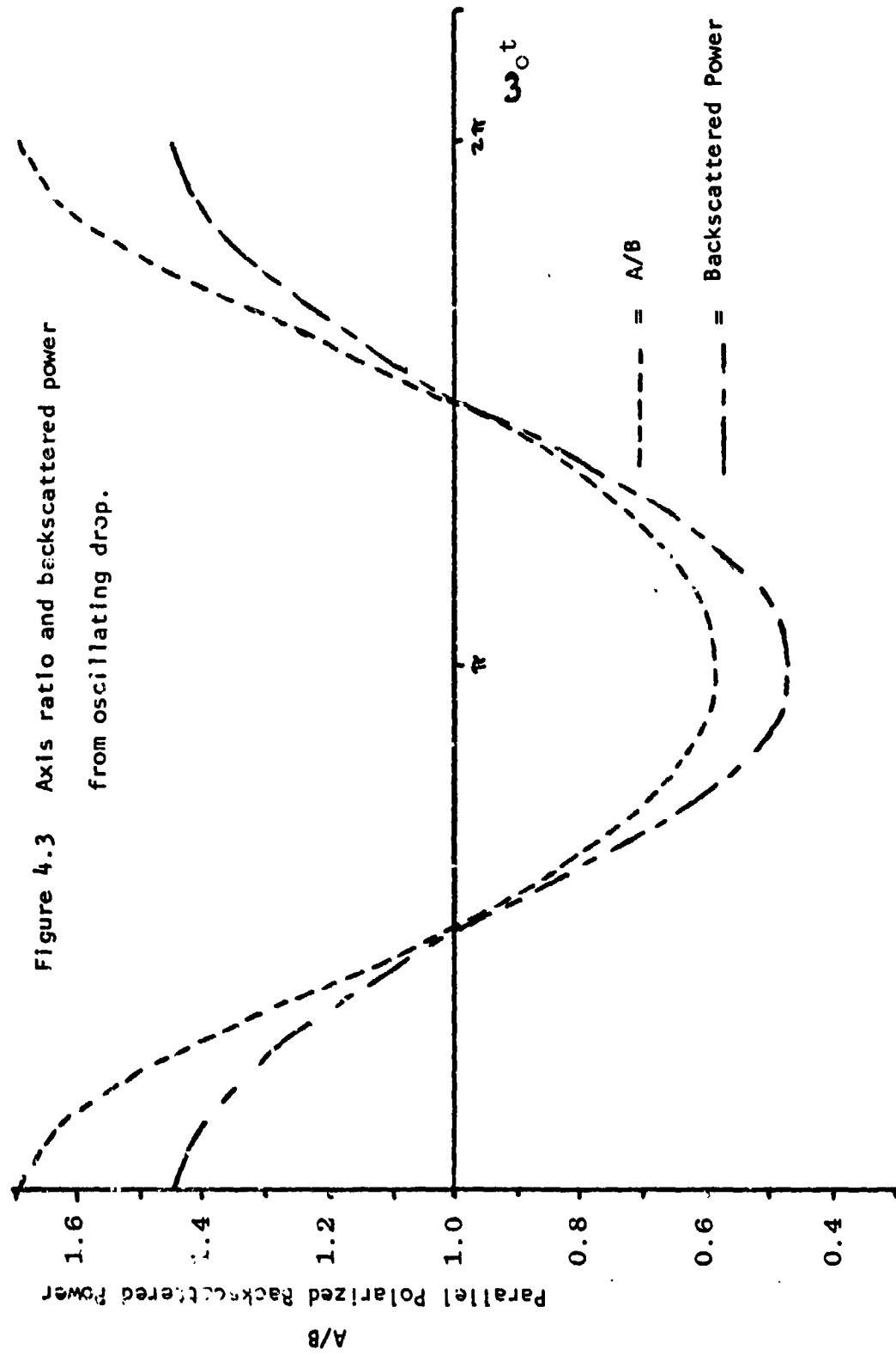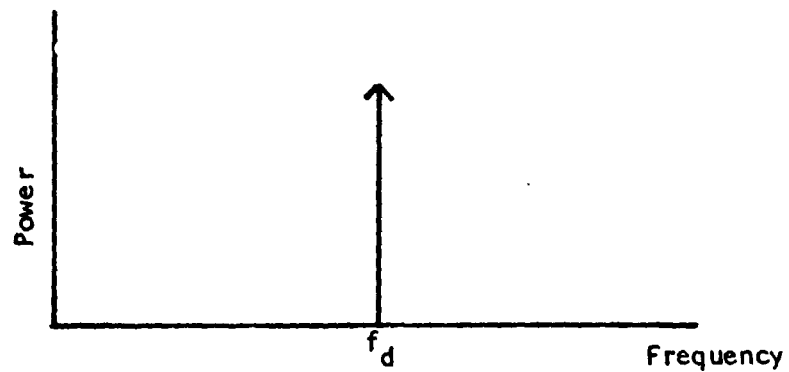
Quiescent drop

Drop oscillating at the fundamental frequency f_2.

Figure 4.4   Doppler spectra for quiescent and

oscillating drops.

process is known as the "bag break-up mechanism" and is shown schemati-
cally in Figure 4.5. Measurements of the maximum stable base diameter
at terminal velocity vary between 6 and 9 mm depending on factors such
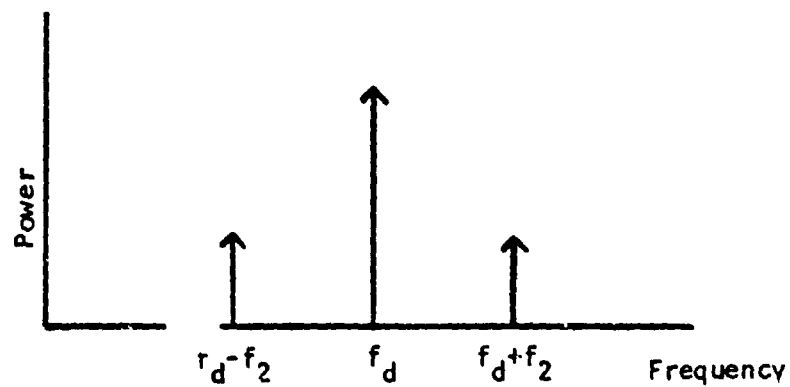as turbulence.

Theoretically, there are two basic approaches to the break-up
problem. The first is essentially dimensional. It defines the Weber
number N_{we} as the ratio of the aerodynamic pressure on the drop to
the surface tension stress.

$$N_{we} = \frac{\rho_a A V^2_{rel}}{\sigma} \tag{4.4}$$

where V_{rel} is the relative wind velocity, ρ_a is the density of air
and A is the diameter of the base of the drop. For values larger
than some critical Weber number the drops are considered to be unstable.
The critical value of N_{we} has been measured to be of order 10.[49,50]

The second theoretical approach, which is also in good agreement
with experimental results, is somewhat more elegant in that it considers
the physical mechanism for break-up. In 1964 Komabayasi et al.[43]
recognized that the bottom surface of a large drop falling at terminal
velocity was in a metastable state with a heavier fluid (water) being
supported in a gravitational field by pressure over a lighter fluid
(air). The bottom surface would, therefore, be subject to gravitational
or Rayleigh-Taylor instabilities when perturbations occurred at the
bottom surface.

Komabayasi et al. assumed that the perturbations would occur as
linear capillary-gravitational waves and that the critical size for

Relative Wind
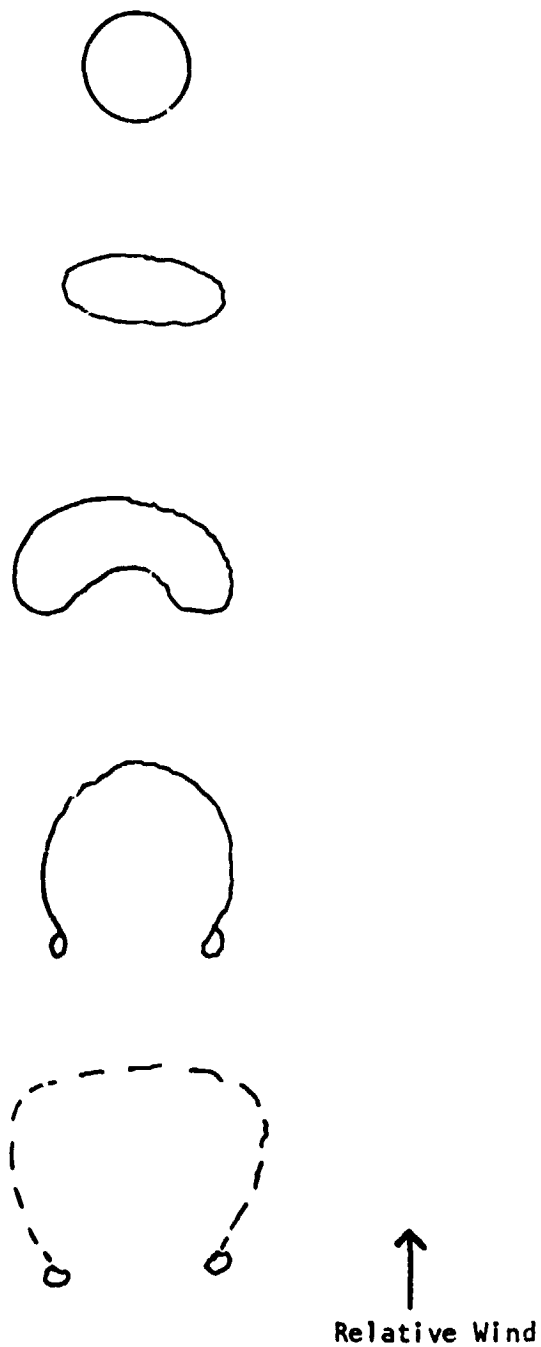
Figure 4.5   Schematic representation of the

"Bag Breakup Mechanism".

drop break-up was when the base diameter A was equal to half the capillary-gravitational wavelength. For typical values of the surface tension, the above predicts a critical base diameter of 8.55 mm for freely-falling drops.

The Komabayasi model was further refined by Klett in 1970,[45] who recognized that, in general, drops flatten with axial symmetry and, therefore, instability should occur when the base diameter A matches the resonances of circular gravitational waves on the bottom surface. Following the notation of Yih[51] in cylindrical coordinates, the equation for the perturbation of the bottom surface of the drop $S(t, \rho \, \phi)$ is

$$S(t,\rho,\phi) = C \; J_n(k_g\rho) \; \cos(n\phi) \; \exp(\alpha t) \tag{4.5}$$

where C is a constant, α is the initial growth rate of the instability and J_n is the Bessel function of nth order. The eigenvalue k_g is the wave number of the surface wave and is determined by the following boundary conditions at the drop edge

$$J_n(k_g\rho) = 0 \qquad \rho = \frac{A}{2} \tag{4.6}$$

$$\frac{dJ_n}{d} = (k_g\rho) = 0 \qquad \rho = \frac{A}{2} \tag{4.7}$$

The allowed solutions for the perturbations, therefore, are the Bessel function modes for a circular membrane. Values of the zeroes $\frac{k_g A}{2}$ are shown for different modes in Table 4.1.

The growth rate for each mode can be found by balancing forces

Table 4.1   The zeroes of Bessel functions and their derivatives
            (kgA), from Abramowitz and Stegun

| Zero # | Bessel Function # | $\frac{k_g A}{2}$ | |
		$J_n(x) = 0$	$\frac{d}{dx} J_n(x) = 0$
1	0	2.405	0.000
2	0	5.520	3.832
1	1	3.832	1.841
2	1	7.016	5.331
1	2	5.136	3.054
2	2	8.417	6.706
1	3	6.380	4.201
2	3	4.761	8.015

at the lower surface of the drop.   Assuming the drop is being accelerated
at a rate a, the growth rate can be written as[51]

$$\alpha^2 = \frac{\sigma(k_g A/2)}{(\rho_w + \rho_a)(A/2)^3} \left[\frac{a(\rho_w - \rho_a)(A/2)^2}{\sigma} - (k_g A/2)^2\right] \quad (4.8)$$

Negative values of α^2 imply oscillatory solutions for the pertur-
bation while positive values imply instability.   The most unstable
mode is therefore the one whose eigenvalue $k_g A/2$ maximizes equation 4.8.

Once instability occurs, the perturbations grow quickly and the
perturbation function $S(t,\rho,\phi)$ is no longer valid; however, the general
characteristics of the Bessel function origins should be observable
even in severely-perturbed drops. The "bag break-up mechanism" is,
therefore, considered to be generated from a perturbation consisting
of the mode which corresponds to the first zero of the axisymmetric
Bessel function J_0.   It should be noted that the J_0 mode is not
necessarily the most unstable, as predicted by equation (4.8). This is
due to internal flow in the drop, which has been shown to occur with
axial symmetry.   This flow tends to suppress modes which are non-
symmetric.   The J_0 is, indeed, the most unstable axisymmetric
mode predicted by equation 4.8 for those conditions where "bag break-up"
was observed.

Inspection of equation 4.8 indicates that for larger values of
acceleration or droplet sizes, higher-order symmetric modes should
become unstable and that, if internal droplet circulation can be
suppressed, then non-symmetric modes should also become unstable.

Some of these modes have, indeed, been observed and are presented in Section 4.3.

4.2   Experimental Techniques for Wind Tunnel Observations of Droplet Shape and Velocity

In order to validate the extension, to arbitrary acceleration, of the theories of drop deformation and instability, experiments were carried out to measure these phenomena for various accelerations. Drops were observed photographically in a wind tunnel. The small drop sizes and short time scales required the application of techniques of high-speed stroboscopic photography. The experimental setup and photographic techniques will be described here.

Experiments were carried out in the MIT low-turbulence wind tunnel located in Building 17A. The tunnel has cross-sectional dimensions of 1 ft. by 1 ft. in the test section and is capable of velocities from 0 to 80 mph. An optically-clear plexiglass test section was construed to allow photographic measurements. Tunnel velocity was measured by a pitot-static probe just upstream of the location where droplets were introduced into the flow.

The photographic setup is shown schematically in Figure 4.6. Drops were photographed using a shadowgraph technique to minimize exposure time. The strobe had a maximum intensity on-center of 18×10^6 lux at one meter and had a full width at half maximum of either .8 or 3 μsec, depending on the intensity setting. The strobe output was diffused by a buffed mylar diffuser screen which backlit the drops. The photographs were taken by a 35 mm. camera with a "macro" lens
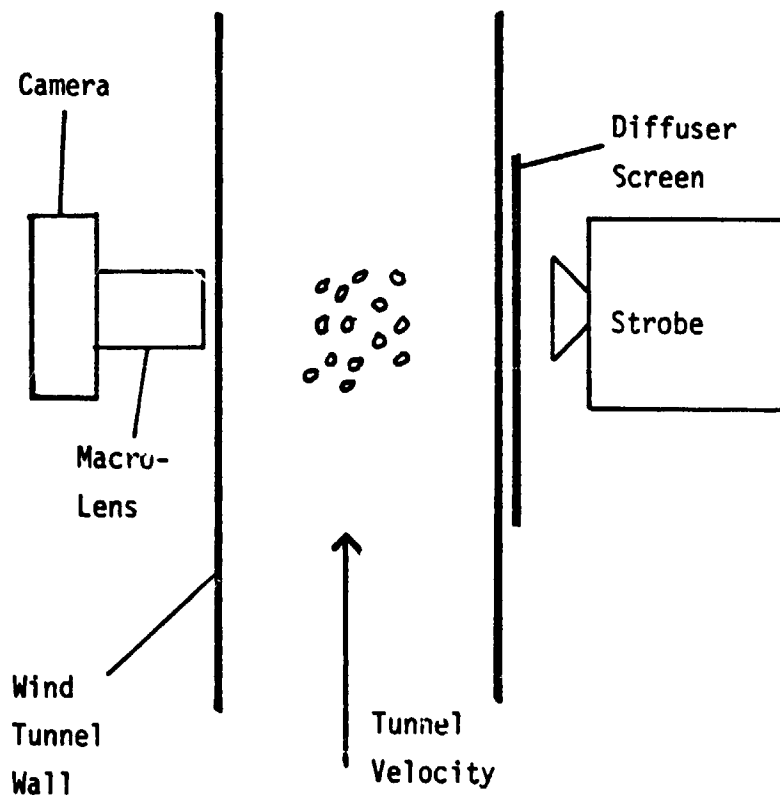
Figure 4.6   Schematic diagram of the Photographic Set-Up.

capable of 1 to 1 magnification. To provide maximum resolution, an extremely-fine-grain aerial-photography film was used (trade name: Kodak Technical Pan) with a high-contrast developer (D-19). The resolution combined with this setup was measured to better than 5 mm for high-contrast objects.

The strobe was triggered by a signal from a firing circuit. For measurements of droplet velocity, two strobes could be fired sequentially to provide time of flight information. The delay between strobes could be set at 12, 24, 64, 93, or 124 μsec, as was appropriate to the velocities to be measured.

The camera was generally operated with the shutter held open (bulb setting) to avoid focal-plane shutter effects. The f-stops were determined experimentally and a range of f-stops were shot on each photographic run. At the beginning of each roll of film, the alignment grid on the diffuser screen, used to help determine camera position, was photographed. A millimeter scale was also photographed in the focal plane prior to each run to provide length calibration. The photographic data was analyzed by microscopic measurement directly from the film.

In the experiments discussed in the following section, a stream of water droplets was injected vertically into the horizontal flow. The setup is shown in Figure 4.7a, which schematically views the injection apparatus along the photographic axis. The droplet stream was generated by the nozzle, shown in Figure 4.7b, which consisted of a 1.27 mm beveled orifice in a flat plate. The bevel was located on the water side of the plate to suppress nozzle instabilities which
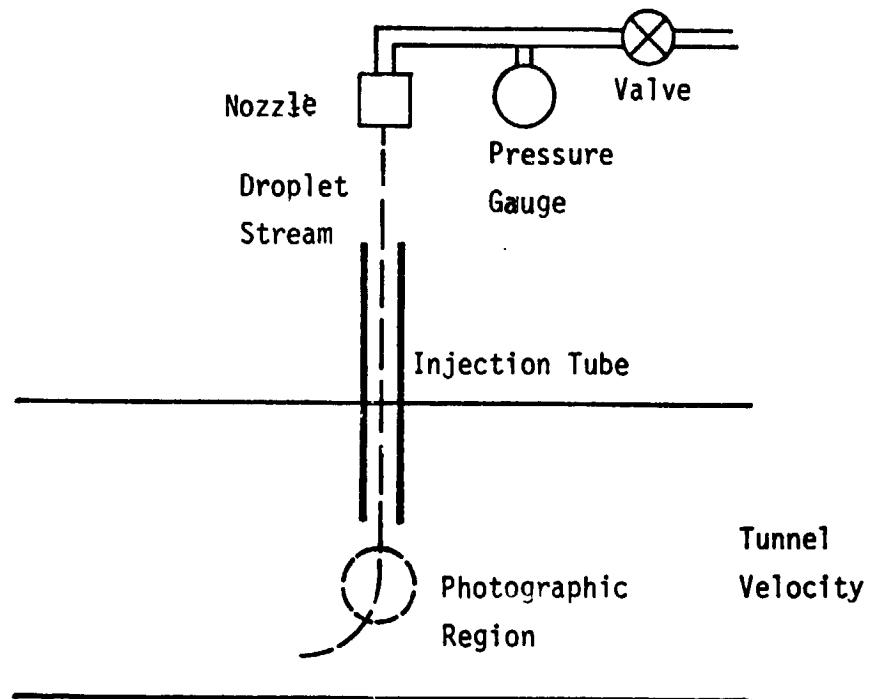
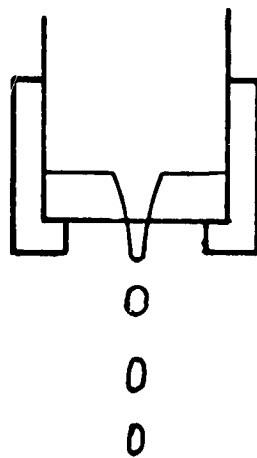Figure 4.7a   Experimental Set-Up to photograph droplet deformation.

Figure 4.7b   Schematic detail of nozzle used in deformation experiment.

caused the stream to wander out of the focal plane. The stream was shielded from the tunnel flow until the midpoint of the tunnel by a 1.9 cm plexiglass injection tube. This was done to avoid flow effects near the wall.

The nozzle was run with tap water at either 15 or 30 PSI and located 55.5 cm above the bottom of the injection tube. The velocity of the drops at the bottom of the tube was measured to be 10.4 m/sec at 15 PSI and 15.6 m/sec at 30 PSI. The mean equivalent droplet diameters were 1.41 and .98 mm, respectively. The drops were not particularly quiescent at injection due to the lack of sufficient fall distance between the nozzle and the injection point for oscillations, generated at the nozzle, to be damped.

The velocity shear below the injection tube was measured by a movable pitot-static probe. The results for all velocities were very similar to those shown in Figure 4.8 for a free-stream velocity of 60 mph. The velocity increases with distance below the injection tube until, at 1 cm, the flow velocity is at the free-stream value.

Droplets were observed between 1 and 3 cm below the injection tube in the photograph region shown in Figure 4.7a. In this region, the drops have not had time to acquire appreciable horizontal velocity. Droplet acceleration is inferred, therefore, by assuming that the horizontal velocity is zero and that the velocity of the relative wind that the droplet feels, V_{rel}, is the sum of the injection velocity V_{inj} and the free stream tunnel velocity U

Figure 4.8   Flow velocity versus distance
below the injection tube.
(Free Stream Velocity = 60mph
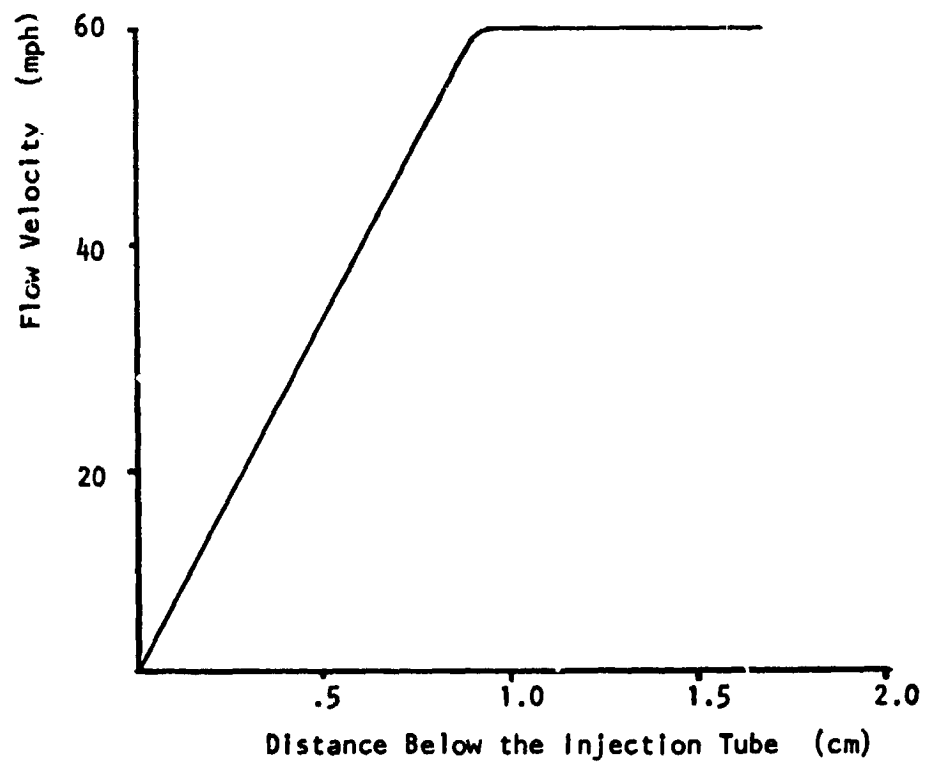
$$V_{rel}^2 = V_{inj}^2 + U^2 \tag{4.9}$$

The acceleration a can be calculated from the hydrodynamic force equation

$$M_w a = \frac{\pi}{2} \left(\frac{A}{2}\right)^2 C_d \rho_a V_{rel}^2 \tag{4.10}$$

where M_w is the mass of the drop, A is the base diameter and C_d is the drag coefficient.   The drag coefficients are extrapolated from the measured values for falling drops and are discussed in more detail in Chapter 5.   The value of M_w is obtained from the photographically-measured dimensions of each drop by assuming that the drops are oblate ellipsoids.

4.3   Experimental Results

Drops observed in the photographic region, described in Section 4.2, 1 to 3 cm below the injection tube, were found to exhibit two types of behavior.   For small drops or low tunnel velocities, the drops flattened into oblate ellipsoids with the axis of revolution aligned with the direction of acceleration resulting from the relative flow velocity V_{rel}.   For larger drops or higher velocities, the drops also deformed initially into oblate ellipsoids but the ellipsoids became unstable and the drops broke up.   Drops of the first kind are described in Section 4.3.1 and the unstable drops are described in Section 4.3.2.

4.3.1   Drop Deformation

The axis ratios A/B of drops deformed into oblate ellipsoids

is plotted against the equivalent accelerated diameter $(a/g)^{1/2}D_{eq}$

in Figure 4.9.   The deformations are much greater than those which

were predicted by the steady-state theory of Section 4.1.   The reason

for the discrepancy can be seen by considering that the time the drops

are in the photographic region is approximately 2 msec.   By comparison,

the fundamental frequency of the mean size drop (D_{eq} = 1.41 mm) is

205 Hz which corresponds to a period of 4.9 msec.   The drops are,

therefore, in the photographic region for less than one-half of a cycle.

The observed behavior of the drops is, therefore, clearly transient

in nature rather than steady-state.

Given the above, some interesting conclusions can be drawn from

the data in Figure 4.9.   While there is quite a bit of scatter in the

data due to the transient behavior of the drops, there seems to be a

clearly-defined limit to the transient deformations.   This is

indicated in Figure 4.9.   This limit is the maximum value of the

oscillating axis ratio A/B of a drop which has suddenly been

accelerated at a rate a.   The maximum axis ratio is just what is

required to calculate the absorption and scattering cross-sections

for drops which experience sudden acceleration due to velocity shear,

such as in turbulence or near an airfoil.

4.3.2   Instability and Drop Break-Up

At tunnel velocities above 40 mph, droplets were observed to

become unstable in the photographic region.   Due to the high velocity

Figure 4.9   Axis ratio versus equivalent accelerated diameter.
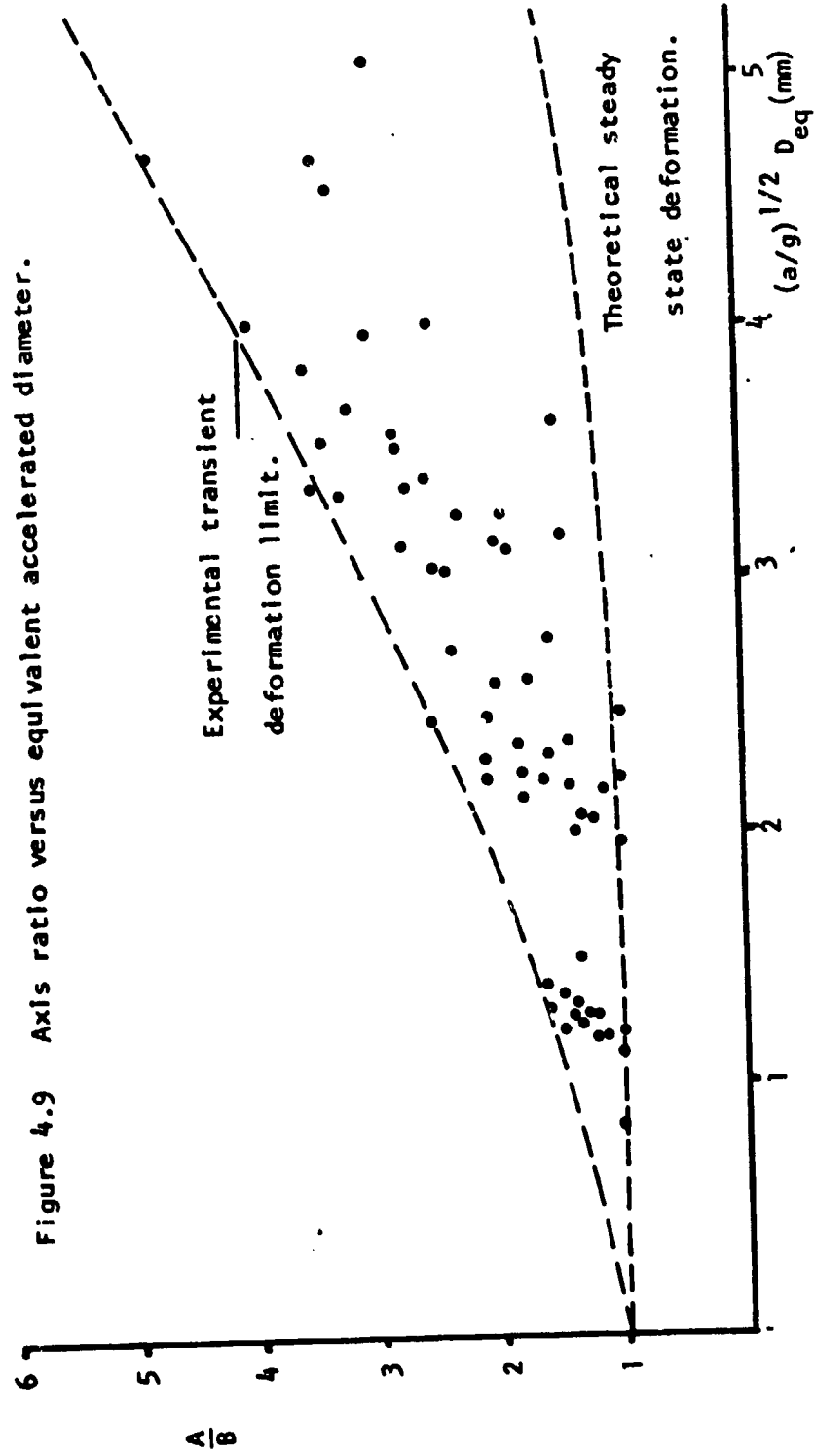
Shear and the resulting acceleration felt by the droplets, higher-order Bessel function perturbations, predicted by Klett[31] were observed along with the "bag break-up" mode observed by others. The theoretical modes are discussed in Section 4.1.3.

At least six different perturbation modes were positively identified. These Bessel function modes are denoted by letters in Table 4.2 along with the boundary conditions and the eigenvalues $k_g A/2$ at the boundary. Photographs of each of the six modes are shown in Figure 4.10 where the relative wind is vertical in the photographs.

The axisymmetric modes A and C correspond to the first and second zeroes of the J_0 Bessel function at the droplet edge. The B mode corresponds to the first nontrivial zero of the derivative of J_0 on the edge. In Figure 4.11 a plot of the $J_0(k\rho)$ surface is provided to aid in visualization.

Mode D corresponds to the first zero of the non-symmetric function $J_1(k\rho)\cos \phi$. A surface plot of this function is provided in Figure 4.12. The periodic dependence with azimuthal angle, $\cos \phi$, is clearly visible in the photograph. Modes E and F correspond to the $J_2(k\rho)\cos 2\phi$ and $J_3(k\rho)\cos 3\phi$ functions. They are also most clearly discerned by their periodic dependence on ϕ. Mode E is twice periodic in one azimuthal revolution, while Mode F is three times periodic in one revolution.

The instability threshold for each mode can be determined from the growth rate equation 4.8. It is
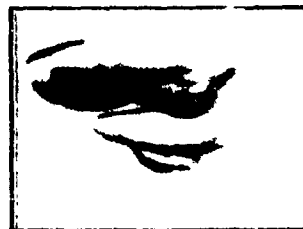
MODE A

MODE D

MODE B

MODE E

MODE C

MODE F

Figure 4.10   Photographs of droplets becoming unstable
in the six observed Bessel function modes.
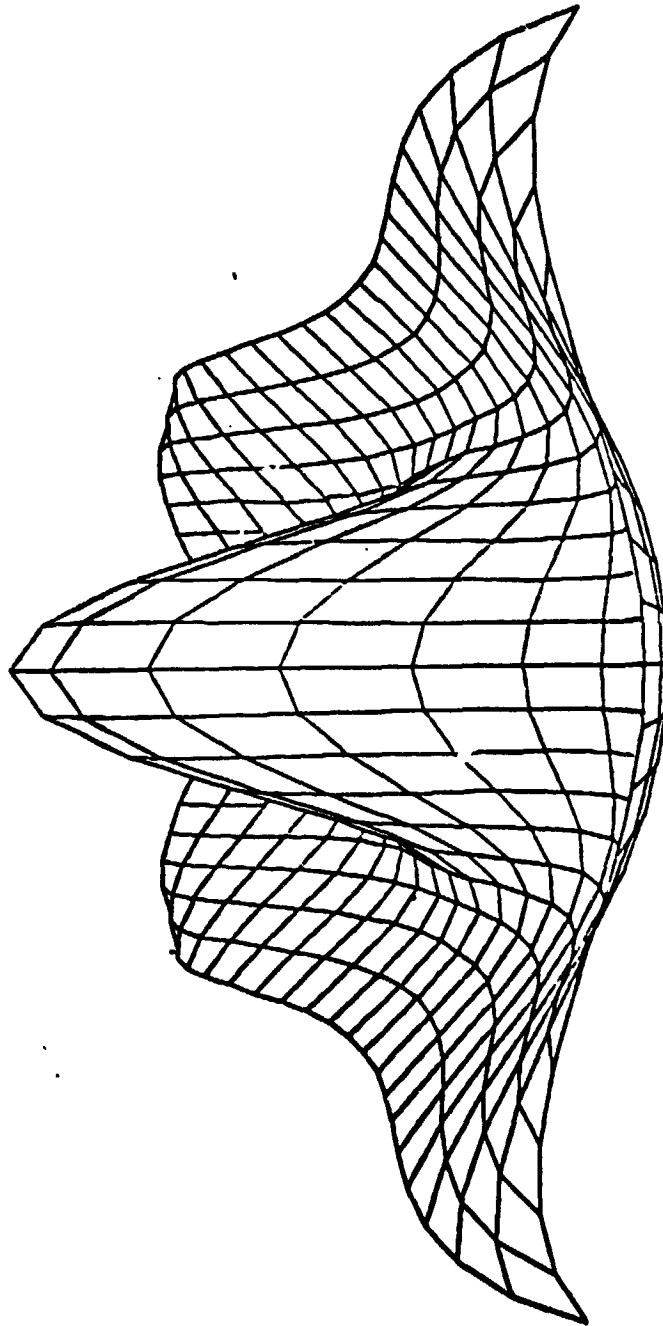
Figure 4.11 Computer generated plot of the $J_o(k\rho)$ surface.
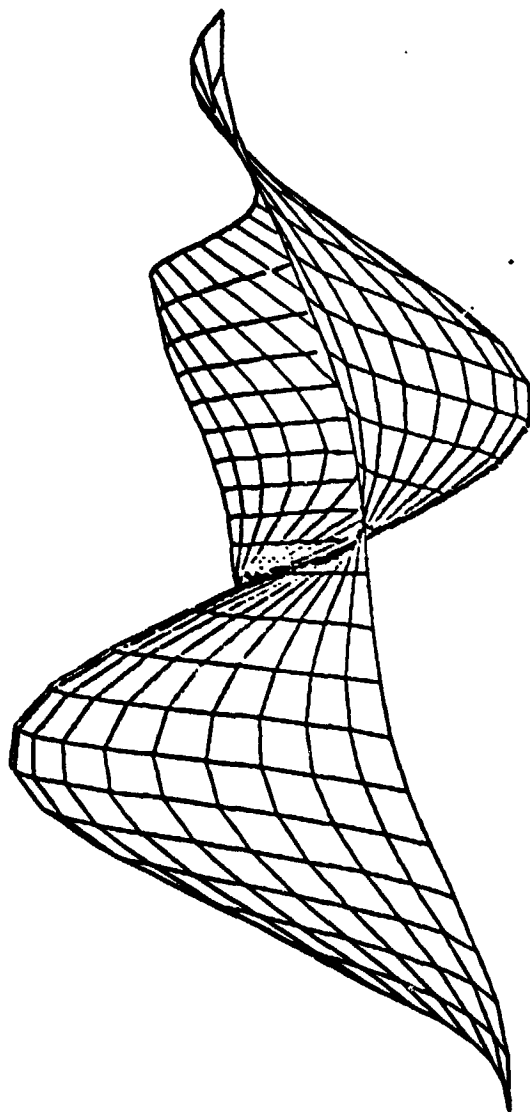
Figure 4.12   Computer generated plot of the $J_1(k\rho)$ $\cos\phi$ surface.

$$\frac{a(\rho_w - \rho_a)A^2}{4\sigma} \geq (k_g A/2)^2 \qquad (4.11)$$

where $k_g A/2$ is the eigenvalue for the particular mode, listed in
Table 4.2. The acceleration can be found from the force equation
4.10. This yield, a relationship for the minimum unstable base
diameter A in terms of the relative wind velocity V_{rel}.

$$A \geq 2 \left[\frac{2}{\pi C_d \rho_a (\rho_a - \rho_w)}\right]^{1/4} [k_g A/2]^{1/2} [V_{rel}]^{-1/2} \qquad (4.12)$$

Observed values of A and V_{rel} are plotted for the three
asymmetric modes along with the instability threshold (equation 4.12)
in Figures 4.13, 4.14, and 4.15. The threshold was calculated
assuming $C_d = 1$ and M_w was equal to the mean value corresponding to
a 0.98 mm diameter drop. There is good agreement with the theoretical
threshold as all observed drops exceed the critical base diameter
for their particular mode. It should be noted that the reason that
the three axisymmetric modes were chosen for analysis was simply
the prevalence of data for these modes, due to their ease of
identification. The non-symmetric modes which were observed also
fulfilled the instability condition (equation 4.11) but less data was
available due to mode identification ambiguities at certain viewing
angles.

In conclusion, the steady-state predictions of drop deformation
were seen to underestimate the observed values of axis ratio A/B.
A maximum transient value of A/B was determined and is shown in

Table 4.2   Surface functions, boundary conditions, and eigenvalues
of observed modes

Mode	Surface Function	Boundary Condition	Eigenvalue $(kA/2)$
A	$J_0(k\rho)$	$J_0(\frac{kA}{2}) = 0$	2.405
B	$J_0(k\rho)$	$\frac{dJ_0}{d\rho}(\frac{kA}{2}) = 0$	3.832
C	$J_0(k\rho)$	$J_0(\frac{kA}{2}) = 0^{*}$	5.520
D	$J_1(k\rho)\cos$	$J_1(\frac{kA}{2}) = 0$	3.832
E	$J_2(k\rho)\cos 2$	$J_2(\frac{kA}{2}) = 0$	5.136
F	$J_3(k\rho)\cos 3$	$\frac{dJ_3}{d\rho}(\frac{kA}{2}) = 0$	4.201

* This boundary condition corresponds to the second zero of
the J_0 Bessel function

Figure 4.13   Instability threshold and odserved values of base diameter versus V_{rel}.

MODE A

Figure 4.14   Instability threshold and observed values
of base diameter versus V_{rel}.

MODE B

Figure 4.15 Instability threshold and observed values of base diameter versus V_{rel}.

MODE C
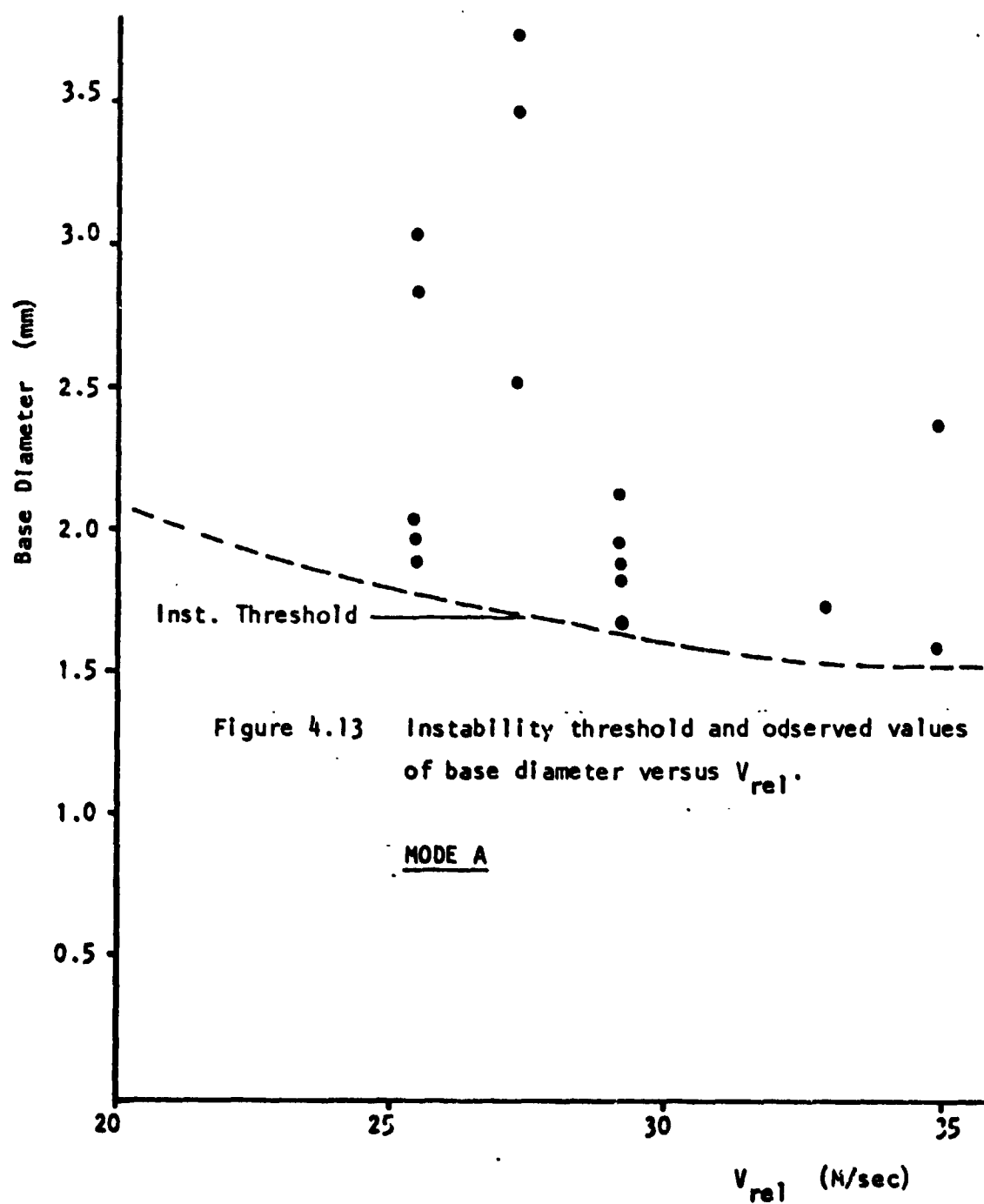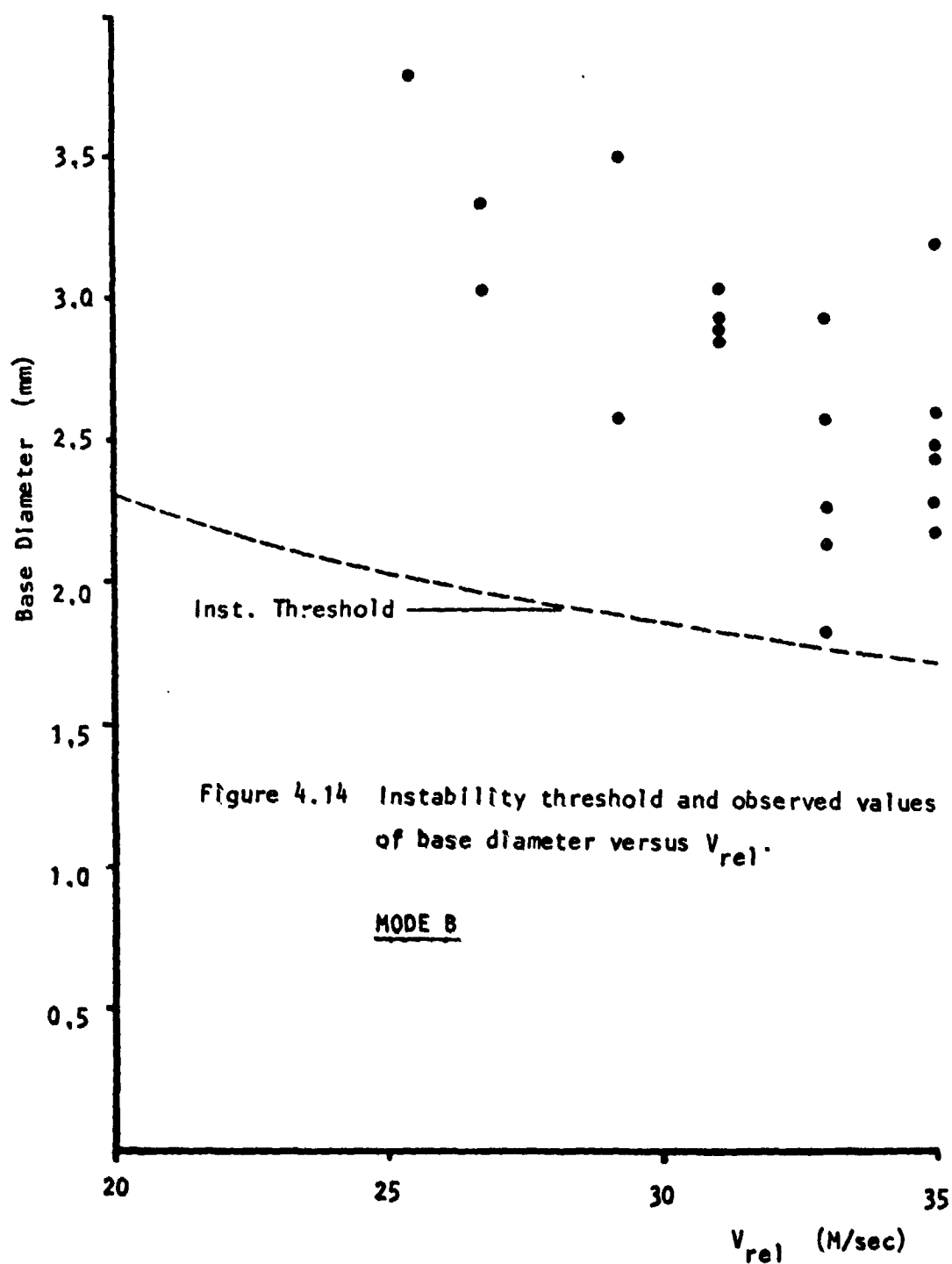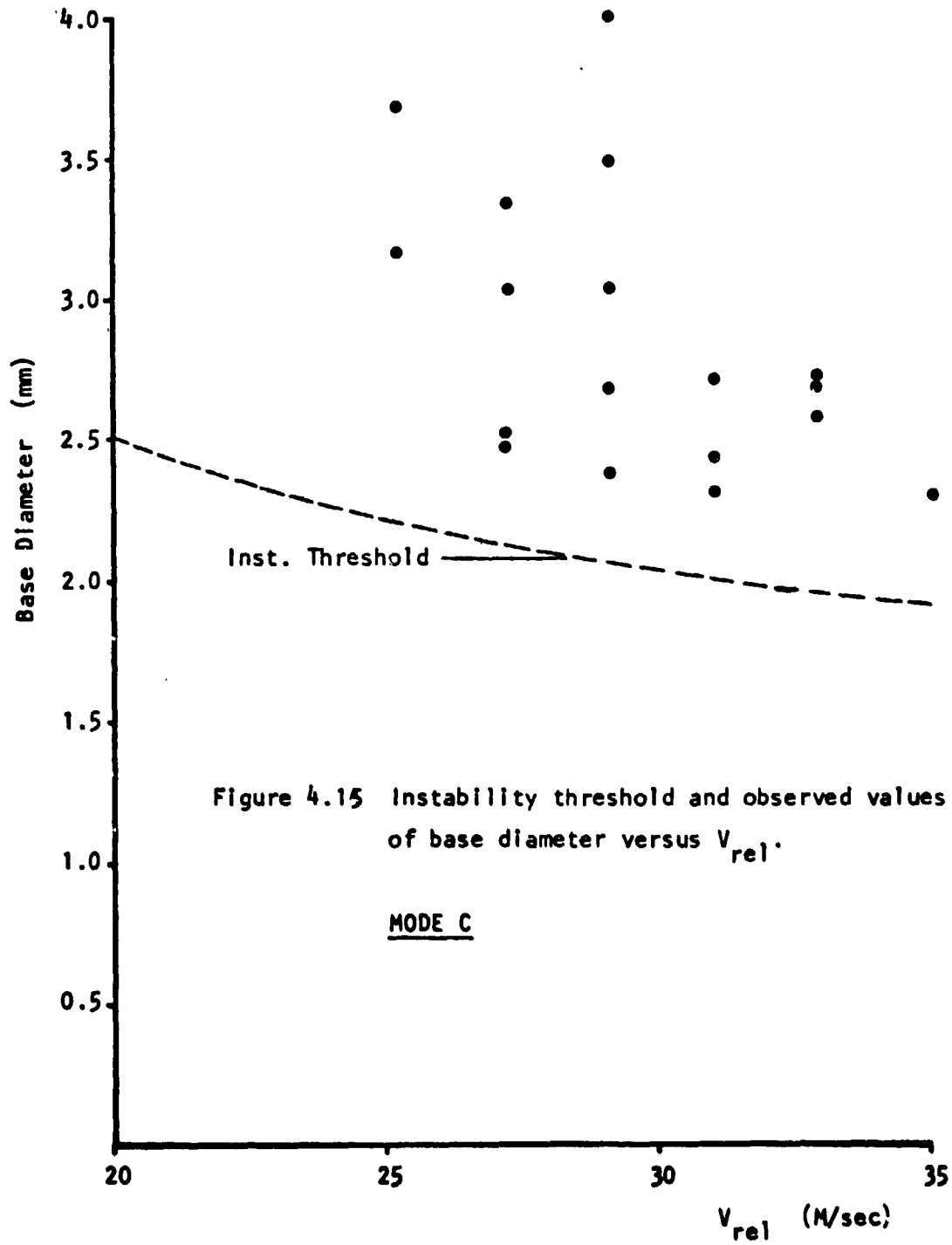
Figure 4.9.   The Bessel function perturbations giving rise to drop instability predicted by Klett[45] have been observed experimentally. The perturbed shapes and the conditions for instability were found to agree well with the predicted values.

CHAPTER 5

DROPLET TRAJECTORIES

The assessment of the trajectories of droplets driven by another fluid is an important part of many fields such as aircraft icing, cloud physics and combustion physics. A computer code which simulates two-dimensional droplet trajectories, either in a freely-flowing fluid or near an object such as an airfoil, has been written and is described in this chapter. In Section 5.1 the computer code is described. In Section 5.2 wind tunnel experiments designed to validate the simulation are discussed. In Section 5.3 some results of calcu'ations for trajectories near an airfoil are presented. The simulation is extended further in Chapter 6, where the microwave heating of droplets near an airfoil is considered.

5.1   Computer Simulation of Droplet Trajectories

The first attempts to calculate droplet trajectories in flowfields perturbed by objects were made in 1940. Glauert[53] studied trajectories near circular cylinders which became the basis of instrumentation to measure the liquid water content of clouds. Kantrowitz[54] studied trajectories and their relationship to aircraft icing. Both Glauert and Kantrowitz integrated the droplet differential equation of motion analytically. The approximations required to do this limited the usefulness of the solutions. In 1945, Langmuir and Blodgett[55] developed a more general approach for the trajectories near simple geometrical shapes which required the use of a differential analyzer.

The technique of iteratively solving the droplet equations of motion, by finite difference techniques, applicable to arbitrary two-dimensional flow fields, was proposed by Bergrun[56] in 1947. The computations were done by hand, which made calculating even one trajectory a major effort. In 1953 a group led by Brun and Rinaldo developed an analog computer which mechanically integrated droplet trajectories.[57-59] They computed trajectories near cylinders and NACA 65,-200 series airfoils. These analog computations, while impressive, were limited due to the difficulty in modifying the programmed flow fields.

The calculation of droplet trajectories, by the iterative solution of the droplet equation of motion, is well-suited to the capabilities of modern digital computers. Very little work has, however, been done in this area. Those codes which do use digital computers have generally been developed by aircraft companies privately and are proprietary.

A computer code to calculate droplet trajectories in an arbitrary two-dimensional flow field has been written and is described in this section. Section 5.1.1 discusses the droplet equation of motion. In Section 5.1.2 the iteration algorithm is presented with a flow chart of the code. Finally, in Section 5.1.3 a discussion of the appropriate drag coefficients, to be used for water droplets, is presented.

5.1.1   Droplet Equations of Motion

The equation of motion for a droplet being driven by another fluid can be written from the hydrodynamic drag equation as

$$M_w \vec{a} = \frac{C_d}{2} \rho_a A_\perp |\vec{u} - \vec{v}| (\vec{u} - \vec{v}) \tag{5.1}$$

where $\vec{a}$ and $\vec{v}$ are the acceleration and velocity vectors of the drop, $\vec{u}$ is the velocity vector of the fluid, M_w is the mass of the drop, ρ_a is the density of air, $A_\perp$ is the area of the drop perpendicular to the relative wind and C_d is the drag coefficient of the drop. It is noted that

$$V_{rel} = |\vec{u} - \vec{v}| \qquad (5.2)$$

is the magnitude of the relative wind felt by the drop, as was discussed in Chapter 4. The drop mass is

$$M_w = \frac{4}{3} \pi \rho_w \left(\frac{D_{eq}}{2}\right)^2 \qquad (5.3)$$

where D_{eq} is the diameter of an equivolumetric sphere and ρ_w is the density of water.

In order to simplify the use of equation 5.1, it is assumed that the area $A_\perp$ of the droplet is the value for an equivolumetric sphere and that any deviation from sphericity will be included in the drag coefficient C_d. Therefore

$$A_\perp = \pi \left(\frac{D_{eq}}{2}\right)^2 \qquad (5.4)$$

Combining equations 5.2, 5.3, and 5.4 with equation 5.1 yields

$$\vec{a} = 3 \, C_d \frac{\rho_a}{\rho_w} \frac{V_{rel}}{D_{eq}} (\vec{u} - \vec{v}) \qquad (5.5)$$

The Reynolds number Re for droplets is defined as:

$$Re = \frac{\rho_a}{\mu} D_{eq} V_{rel} \qquad (5.6)$$

where μ is the dynamic viscosity of air plotted against temperature in Figure 5.1 from the values in the Smithsonian Meteorological Tables.[60] The equation of motion (equation 5.5) can be written in the simplified form as

$$\vec{a} = (\frac{C_d Re}{24}) \frac{1}{K_a} (\vec{u} - \vec{v}) \qquad (5.7)$$

where

$$K_a = \frac{1}{18} \frac{\rho_w}{\mu} D_{eq}^2 \qquad (5.8)$$

which is constant over a particular trajectory.

Equation 5.7 is the equation of motion used in the trajectory code. It has a form similar to the equation of motion first proposed by Langmuir and Blodgett.[55] The coefficient $(\frac{C_d Re}{24})$ is presumed to be a function of the Reynolds number and is discussed in section 5.1.3; K_a is constant (assuming D_{eq} remains constant); and $(\vec{u} - \vec{v})$ is the relative wind felt by the droplets.

Figure 5.1   Dynamic viscosity versus
temperature.
(from Smithsonian Met. Tables)
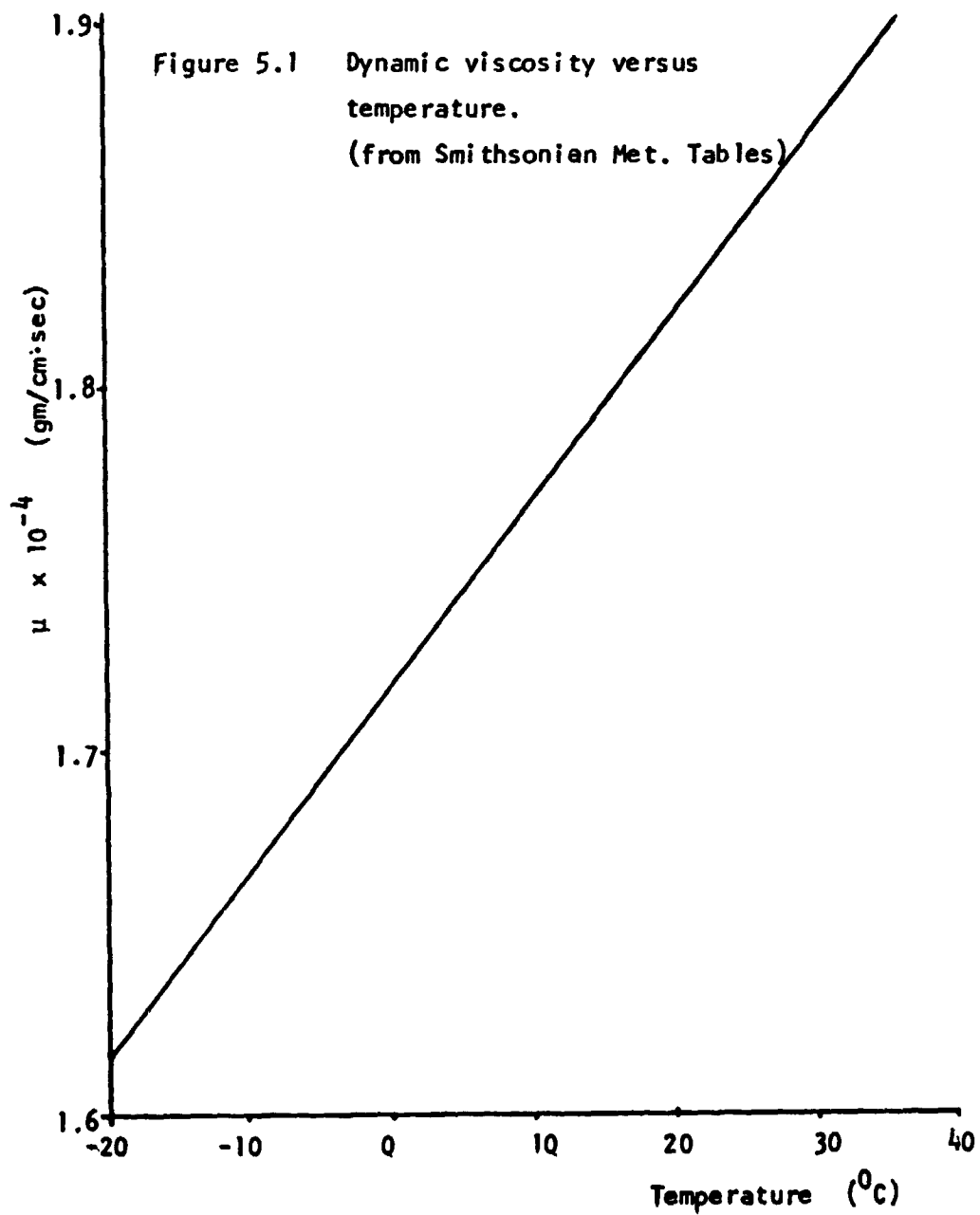
5.1.2   Iteration Algorithm

A flow diagram for the iterative computation of two-dimensional droplet trajectories is shown in Figure 5.2.   Three groups of input parameters are required.   They are the flow field, the initial droplet conditions and the atmospheric conditions.   The code calculates trajectories for an arbitrary known two-dimensional flow field.   The velocity field $\vec{u}(\vec{x})$, where $\vec{x}$ is position, must be input either through flow equations or by means of tabulated values.   If trajectories near bodies are being calculated, then the position of the body surfaces must be included.

The initial conditions for the droplets are the equivalent diameter D_{eq}, the initial position $\vec{x}_0$ and the initial velocity $\vec{v}_0$.   The atmospheric temperature and pressure are required to compute air density, viscosity, and K_a.

Once the initial conditions have been determined, the equation of motion (equation 5.7) is solved at the initial position.   The velocity $\vec{v}$ and position $\vec{x}$ are then incremented one time step Δt by the first order Euler integration equations

$$\vec{x}_{i+1} = \vec{v}_i \, \Delta t + \vec{x}_i \tag{5.9}$$

$$\vec{v}_{i+1} = \vec{a}_i \, \Delta t + \vec{v}_i \tag{5.10}$$

The value of Δt was taken to be 10 microseconds in most of the simulations, although it could be varied as necessary.

Once the position and velocity have been incremented, the code checks for hydrodynamic stability of the drop (as determined by the
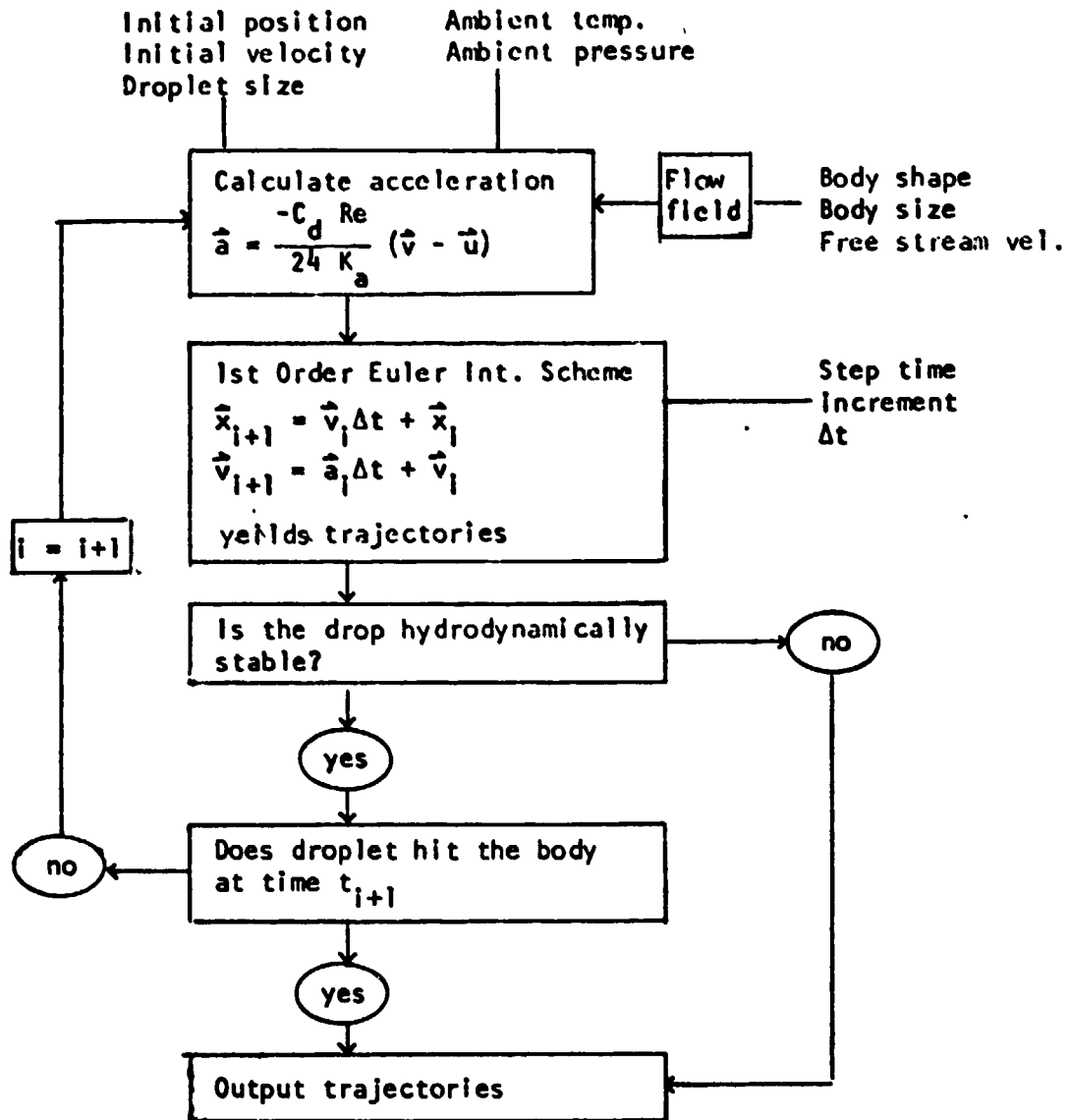
Figure 5.2   Flow diagram for trajectory code.

stability conditions in Chapter 4) and for collision with the body. If
either of the above conditions occur, then the code kicks out of the
iteration loop and outputs trajectories to that point. If the drop
remains stable and no collisions occur, then the code cycles back and
calculates acceleration at the new droplet position. The code then
progresses through the loop. Values of droplet velocity and
acceleration can also be output along with the trajectories. Additional
forces such as gravity can be included in the acceleration equation.

5.1.3   Drag Coefficients

In previous calculations of droplet trajectories, investigators have
used a variety of drag coefficients. Glauert[53] and Kantrowitz[54] assumed
Stokes (viscous) flow around spherical droplets. Langmuir and Blodgett[55]
observed that at aircraft velocities and meteorological droplet diameters,
Stokes' law does not hold. They proposed using drag coefficients
measured for solid spheres.

In order to check the validity of the Langmuir and Blodgett drag
coefficients C_d, or equivalently $(\frac{C_d Re}{24})$, the code was used to compute
the terminal fall velocity of drops in the earth's gravitational field.
The results are shown in Figure 5.3, along with the well-accepted
experimental results of Gunn and Kinzer.[61] The Langmuir and Blodgett
coefficients predict a higher terminal velocity than is observed
experimentally. The reason for the discrepancy is that the Langmuir
and Blodgett coefficients neglect such effects as drop deformation and
the increased drag due to turbulent eddies downstream of the drop. These
effects increase C_d and reduce the terminal velocity.

In order to improve on the Langmuir and Blodgett coefficients, it

ORIGINAL PAGE IS
OF POOR QUALITY

Figure 5.3

Terminal velocity of drops (M/sec)

versus diameter (mm).

O Gunn and Kinzer (exnt.)

___ Calculated by the code

using Langmuir and Blodgett

drag coefficients.

D_{eq} (mm)
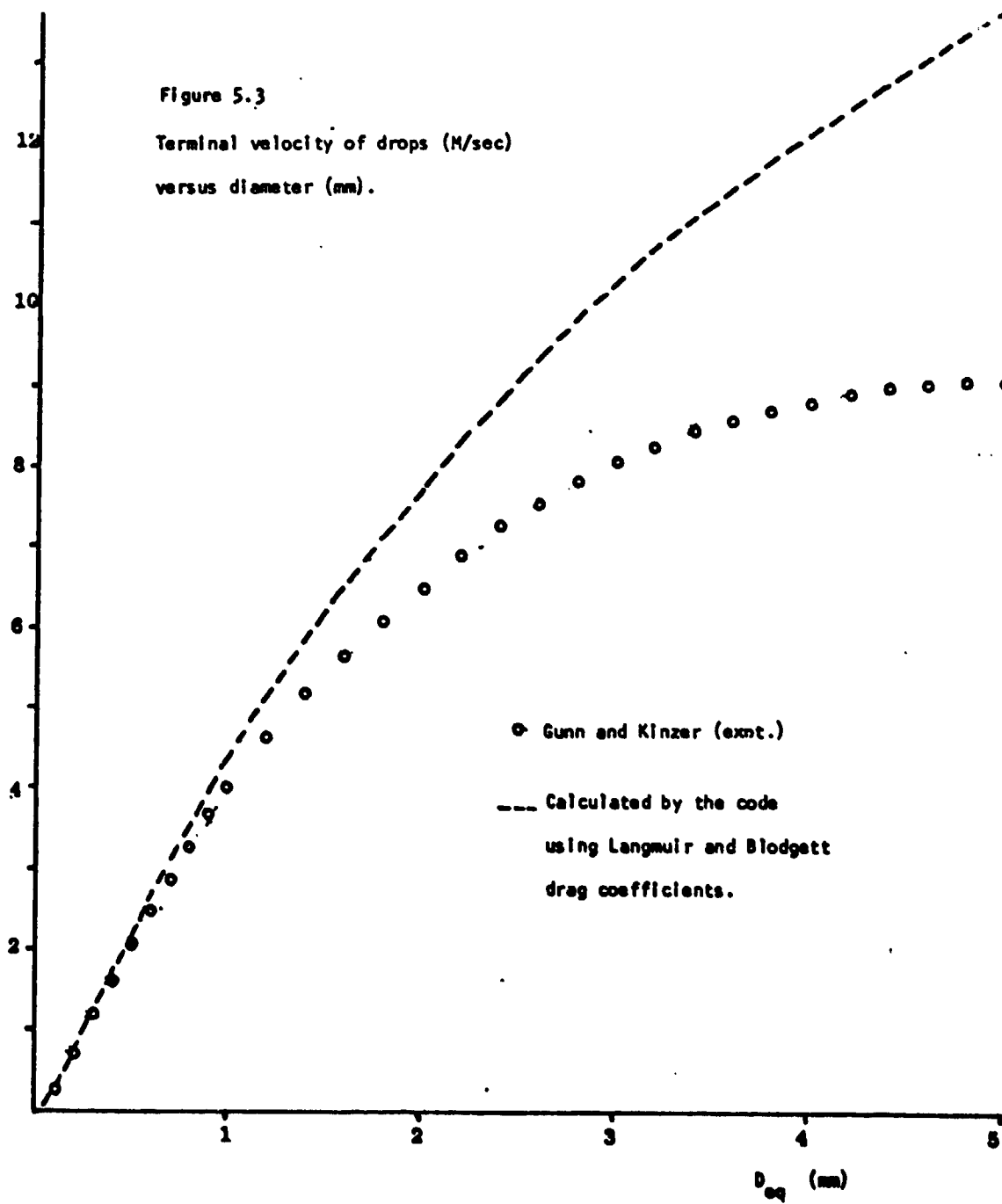
was decided to invert the Gunn and Kinzer experimental results to determine a set of empirically modified drag coefficients. The modified values of $(\frac{C_d Re}{24})$ are plotted against Reynolds number in Figure 5.4 along with the Langmuir and Blodgett values. The experimental values cut off at Re = 3500, due to drop break-up. It is assumed that the values of $(\frac{C_d Re}{24})$ can be extrapolated to higher Reynolds numbers. Therefore, from Figure 5.4

$$\frac{C_d Re}{24} = 1.699 \times 10^{-5} \, (Re)^{1.92} \qquad Re > 3500 \qquad (5.11)$$

Using the modified drag coefficients, the terminal velocity was calculated by the code and is plotted in Figure 5.5. The values, as expected, agree well with the Gunn and Kinzer data for the atmospheric conditions under which the experiments were performed. The values of 1080 mb pressure and 20°C are typical surface conditions. Figure 5.5 also includes terminal velocities calculated for typical icing conditions of 750 mb and 0°C, where the lower air density causes less drag and a resultingly higher terminal velocity. The above modified drag coefficients have been incorporated into the trajectory code. For Reynolds numbers greater than 3500, equation 5.11 is used. For Reynolds numbers less than 3500, the code interpolates between tabled values of $(\frac{C_d Re}{24})$. The values which have been used are listed in Table 5.1 for reference.

Figure 5.4   Drag coefficient versus Reynolds number.

Figure 5.5

TERMINAL FALL VELOCITY OF DROPS (METERS/SEC)
VERSUS DIAMETER (mm.)

○ ○ ○ Gunn & Kinzer (expt.)
       1080mb 20°C ν=.1485cm^2/s

- - - - Code (modified C_d) Surface Conditions
       1080mb 20°C ν=.1485cm^2/s

- · - · Code (modified C_d) Icing Conditions
       760mb 20°C ν=.1785cm^2/s

D_{eq} (mm)
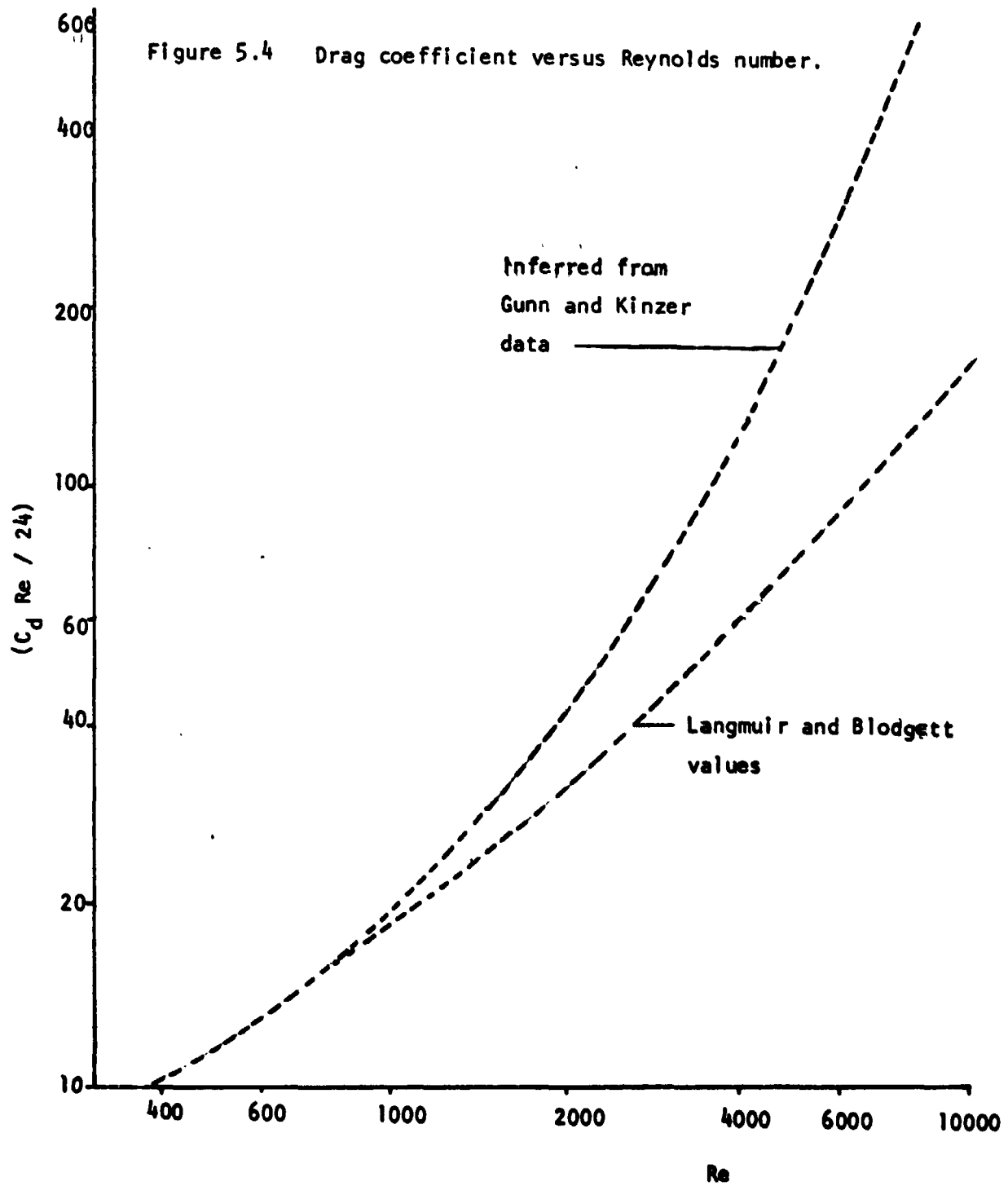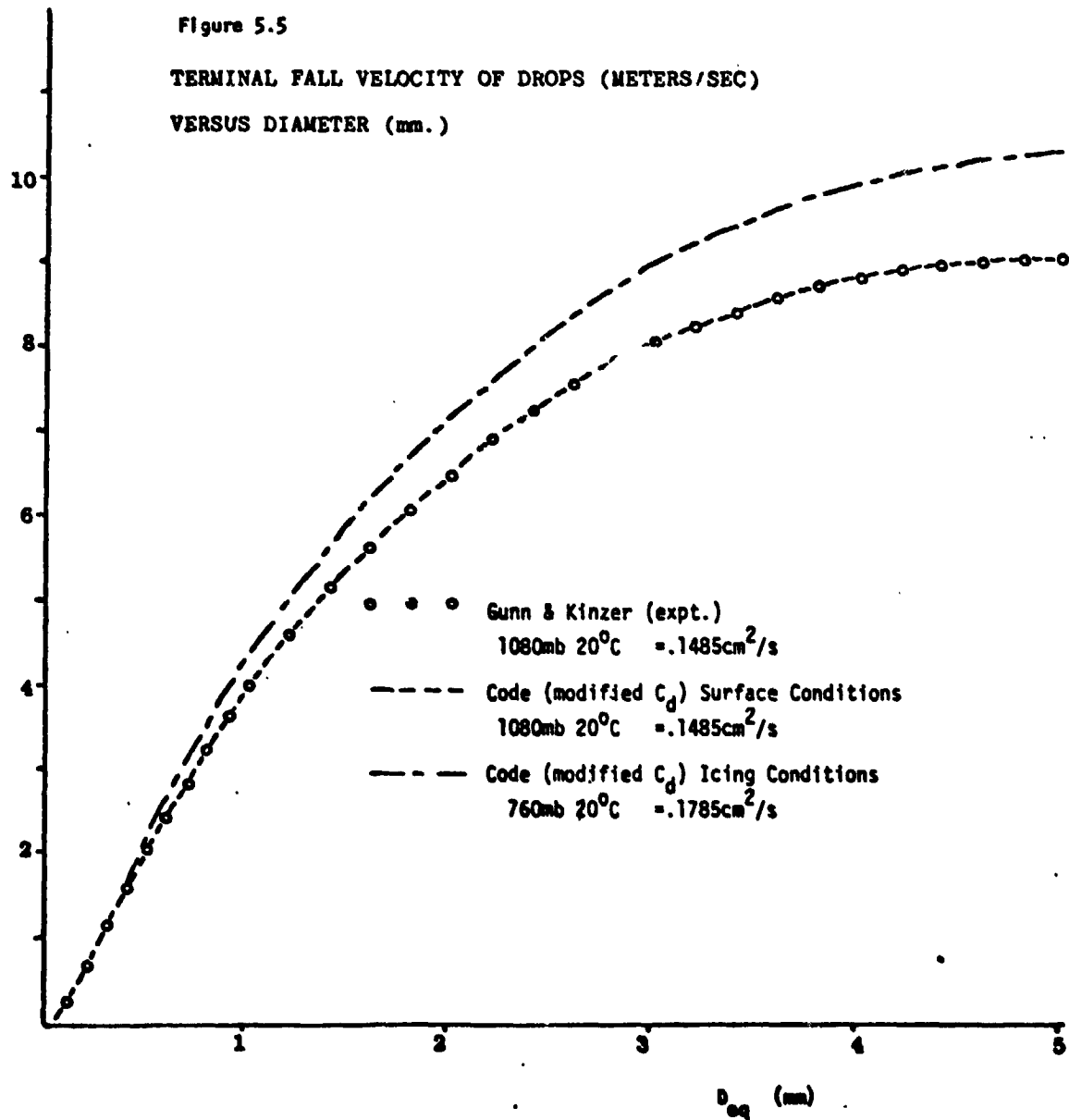
Table 5.1   Values of $(C_d \, Re/24)$ as a function

of Reynolds number.

Re	$C_d \, Re/24$	Re	$C_d \, Re/24$
0.00	1.00	68.7	3.664
0.05	1.009	98.9	4.409
0.1	1.013	134.0	5.170
0.2	1.037	175.0	5.943
0.4	1.073	220.0	6.683
0.6	1.103	269.0	7.520
0.8	1.142	372.0	9.480
1.0	1.176	483.0	11.47
1.2	1.201	603.0	13.69
1.4	1.225	731.0	16.08
1.6	1.248	866.0	18.66
1.8	1.267	1013.0	21.27
2.0	1.285	1164.0	24.01
2.5	1.332	1313.0	27.03
3.0	1.374	1461.0	30.32
3.5	1.412	1613.0	33.81
4.0	1.447	1764.0	37.56
5.0	1.513	1915.0	41.49
6.0	1.572	2066.0	45.54
8.0	1.678	2211.0	50.12
10.0	1.782	2357.0	54.83
12.0	1.901	2500.0	59.89
14.0	2.009	2636.0	65.24
16.0	2.109	2772.0	71.03
18.0	2.198	2905.0	76.86
20.0	2.291	3033.0	83.41
25.0	2.489	3164.0	89.78
30.0	2.673	3293.0	96.05
35.0	2.851	3423.0	103.69
40.0	3.013	3549.0	111.05
50.0	3.327		

5.2   Wind Tunnel Validation of Computer Trajectories

The computer-generated droplet trajectories have been checked by
comparison with wind tunnel measurements of droplet velocity.   In
Section 5.2.1, velocity measurements of droplets injected into a freely-
flowing wind tunnel are compared with predicted values.   In Section
5.2.2 droplets are observed just upstream of a cylinder where the
flow field is spatially varying but well known.   The measured
velocities are compared with the predicted values and good agreement is
obtained.

5.2.1   Droplets Injected into a Uniform Flow

In order to verify the computer-predicted trajectories, droplets
were observed in the set-up shown in Figure 5.6.   Droplets were
injected into a freely-flowing tunnel perpendicular to the flow.
Droplet velocity components along the tunnel axis were measured
125 cm downstream of the injection site.   The measurements were made
by the double strobe photographic technique discussed in Section 4.2
and the wind tunnel was the MIT 1 ft. x 1 ft. facility described in
that section.

The observed droplet velocities for three values of the tunnel
free-stream velocity (45 mph, 60 mph., 75 mph) are shown in Figure 5.7
along with the computer-calculated values.   There is good agreement
over the observed 0.15 to 1.0 mm range of equivalent droplet diameters.
At the observation site the small droplets, due to their low inertia,
are close to the free-stream velocity, while the larger droplets are
slower and still accelerating.   The discrepancy between observed and
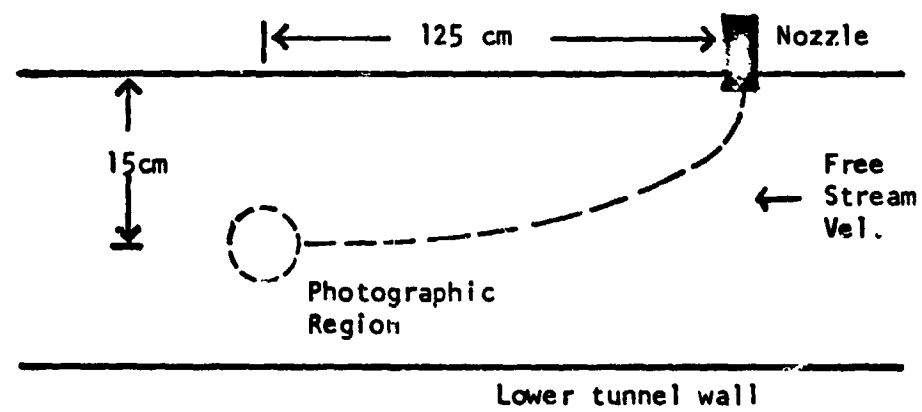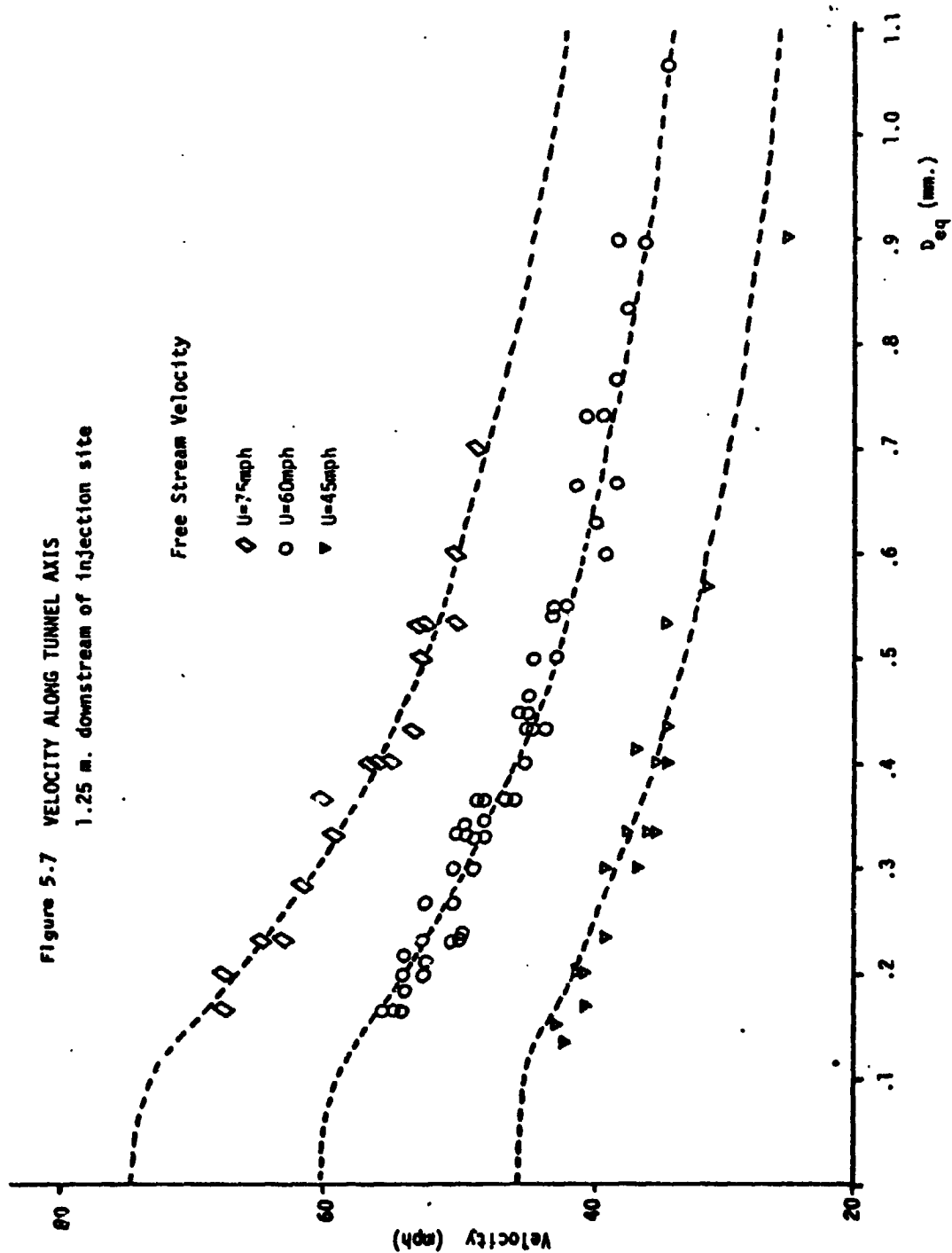predicted values of velocity are attributed to difficulty in measuring

Figure 5.6   Experimental set up for droplet velocity

measurements in a uniform flow.

Figure 5.7 VELOCITY ALONG TUNNEL AXIS
1.25 m. downstream of injection site

D_{eq}, slight variations in the tunnel velocity, and perturbed initial conditions due to droplet break-up or other injection effects.
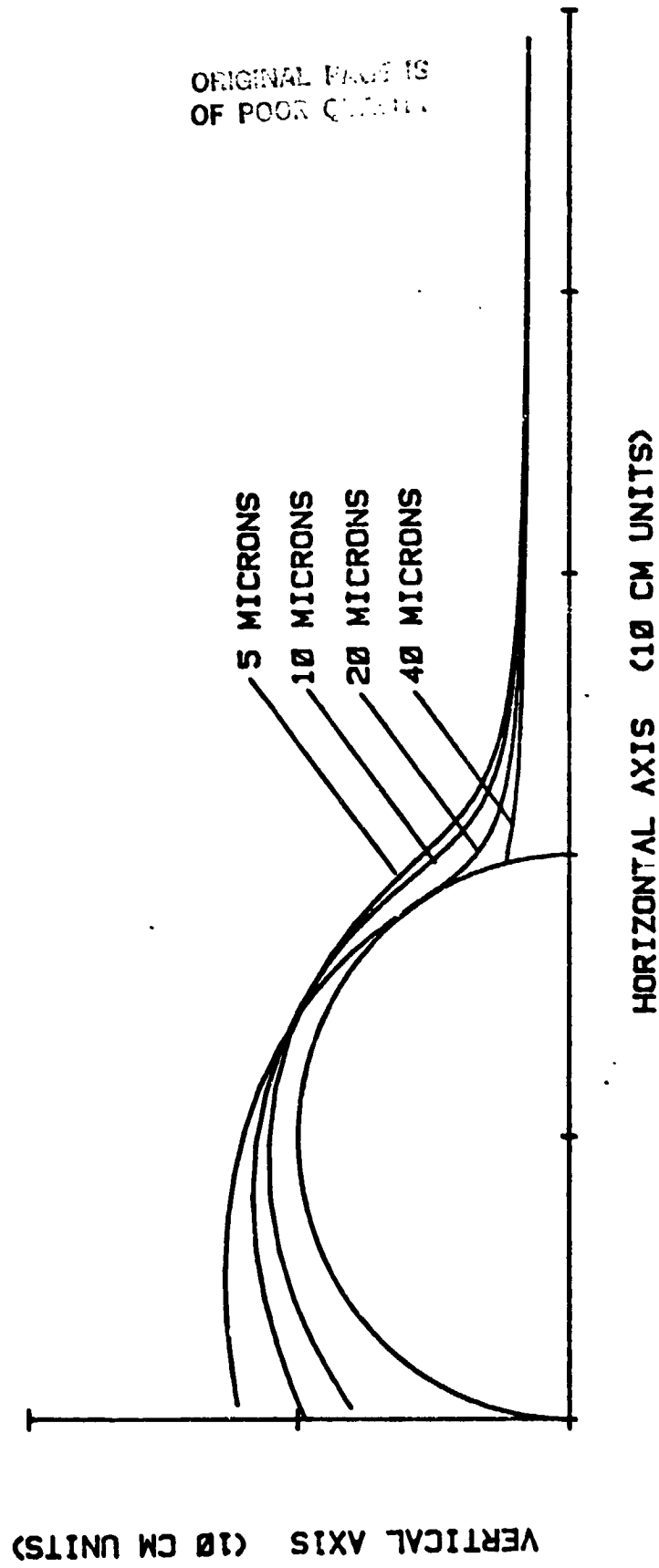
5.2.2 Droplet Trajectories Near a Cylinder

In order to confirm that the comptuer code accurately predicted trajectories, in regions of spatially-varying flow, observations of droplet velocity just upstream of a cylinder were made in the wind tunnel. A cylinder was chosen because the two-dimensional flow ahead of a cylinder is well known to have a simple analytical form.

An example of the trajectories generated by the code is shown in Figure 5.8. In this case the cylinder had a 10 cm radius and the free-stream velocity was 60 m/sec flowing to the left. Four droplets with diameters of 5, 10, 20 and 40 microns were incident on the cylinder from a position 1.25 cm above the stagnation streamline. The effects of inertia can be clearly seen as the smaller droplets are turned by the flow, while the 40-micron drop continues on and impacts the cylinder. The effects of inertia on the impingement trajectories will be discussed further in Section 5.3.

The experimental set-up used to measure velocities near the cylinder was very similar to that described in Section 5.2.1 and is shown in Figure 5.9. The photographic region was centered above the stagnation streamline ahead of the cylinder. Trajectories ahead of two cylinders of diameters 11.25 and 2.4 cm were observed. The cylinders were painted black to minimize stray reflections in the photographs. The free-stream velocity was varied from 45 to 75 mph. Droplets were injected perpendicular to the flow 125 cm upstream of the

FIGURE 5.8

DROPLET TRAJECTORIES NEAR CYLINDER

ORIGINAL PAGE IS
OF POOR QUALITY

5 MICRONS
10 MICRONS
20 MICRONS
40 MICRONS

HORIZONTAL AXIS (10 CM UNITS)
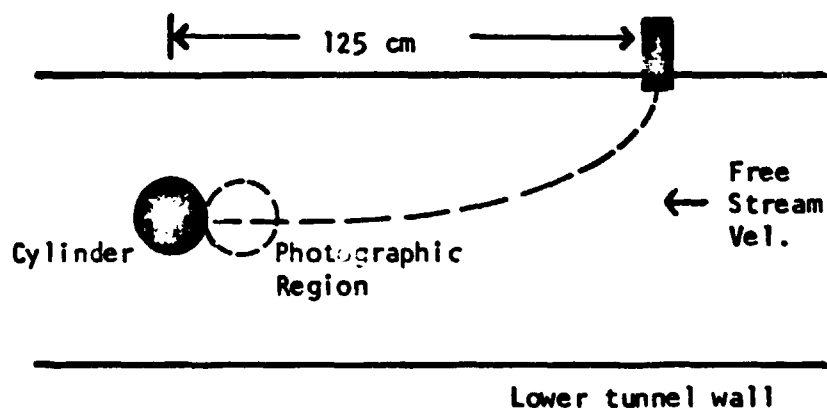
VERTICAL AXIS (10 CM UNITS)

Figure 5.9   Experimental set-up for droplet
velocity measurements ahead of
a cylinder.

cylinder axis and the velocities were measured by the double strobe technique.

Several hundred droplet velocities were observed and compared to the computed values. The measured and computed drop velocities were found to agree with a standard deviation of less than 3% of the predicted velocity for accurately-photographed droplets.

As an aside, it was observed that when large droplets impacted the cylinder, they splashed in rather constant patterns. An example is shown in Figure 5.10a. The result of the impact of a large drop was a collection of smaller residual droplets with velocities of order one-tenth of the free-stream velocity directed radially away from the point of first contact with the cylinder. Splash patterns of this sort are thought to be the cause of the double-horned ice build-up sketched in Figure 5.10b observed on airfoils under certain icing conditions.

In conclusion, the experimental evidence supports the results of the computer simulations. The code, can, therefore, be applied to other situations of interest with some confidence in the results.

5.3   Simulation Results Near the Leading Edge of an Airfoil

In this section, results of droplet trajectory computations near an airfoil are presented. The airfoil leading edge is simulated by a two-dimensional half body, an example of which is shown in Figure 5.11. The half body was chosen because it closely resembles the front of an airfoil and the velocity field equations have a particularly simple form. If the flow is assumed to be inviscid, then the velocity
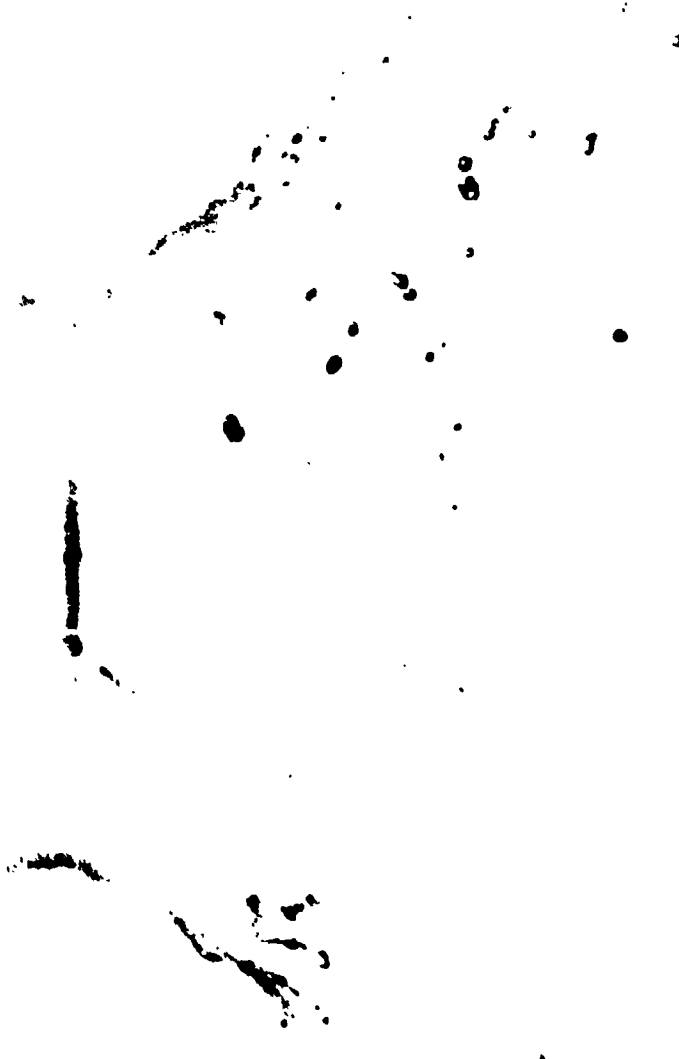
Figure 5.10a   Photograph of a
large drop impacting the cyl-
inder surface.
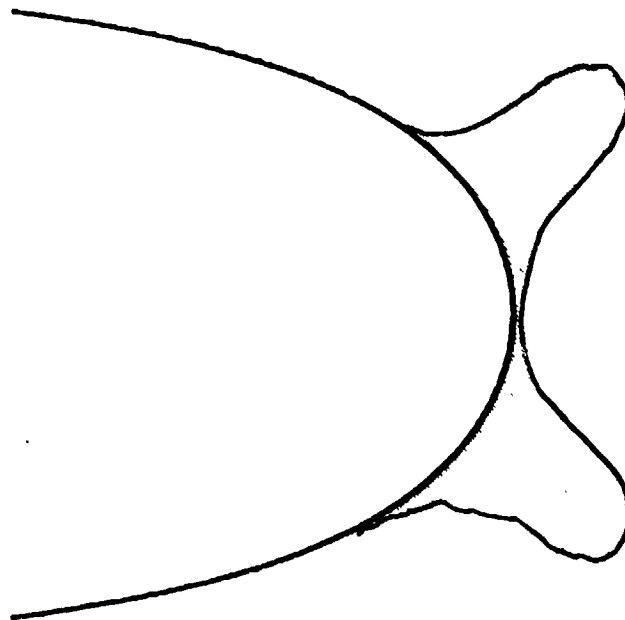
Figure 5.10b   Sketch of a "double horn" ice formation.
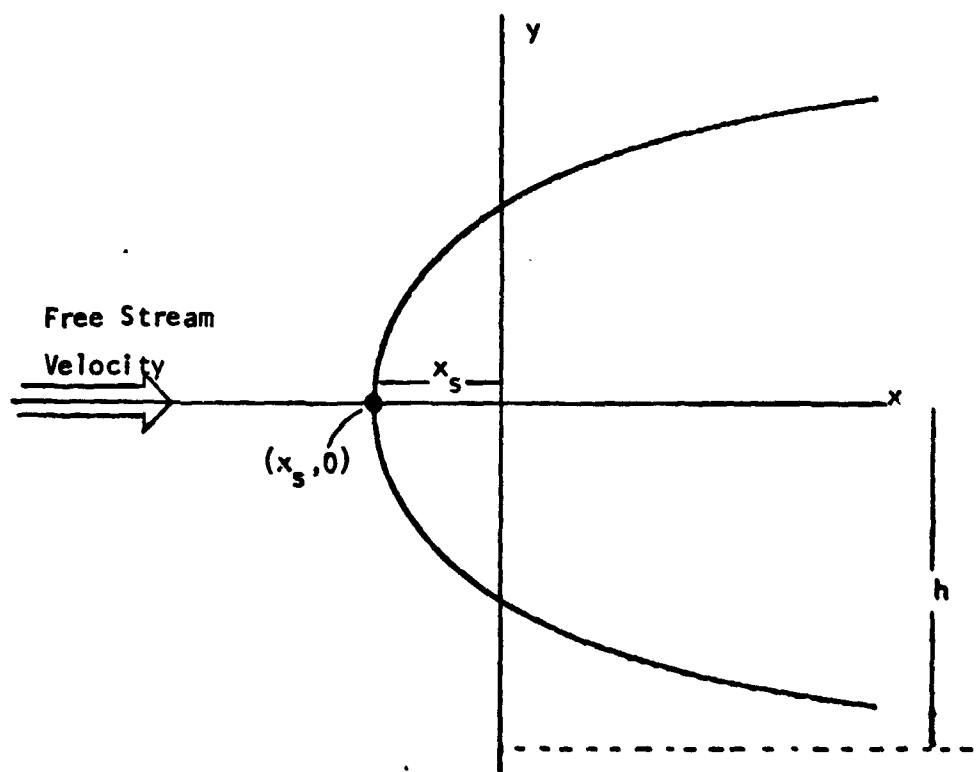
Figure 5.11   View of the 2D half body.

potential function Φ is simply the sum of uniform flow in the x-direction and a source at the origin[62]

$$\Phi(x,y) = U \left(x + x_s \ln \sqrt{x^2 + y^2}\right) \qquad (5.12)$$

where $-x_s$ is the x coordinate of the leading edge

$$x_s = h/\pi \qquad (5.13)$$

where h is the half-thickness of the body. The velocity $\vec{v}$ is related to Φ by

$$\vec{v}(xy) = \vec{\nabla}\Phi(x,y) \qquad (5.14)$$

The half body equations can be used to simulate droplet impingement onto an airfoil. The only weakness is the assumption of an 0° angle of attack α implicit in the half body flow model. Effects such as droplet inertia and droplet collection efficiency, which are weak functions of α, can be adequately investigated. In order to study effects which depend strongly on α, the particular flow field of interest must be inserted in the code.

In Section 5.3.1, some two-dimensional impingement trajectories are presented. Some results on droplet collection efficiency, and their effect on the impinging mass distribution function, are discussed. In Section 5.3.2, the effect of the airfoil on the kinematics of droplets is studied. Finally, in Section 5.3.3 some additional simulations are presented which demonstrate the flexibility of the model.

5.3.1   Two-Dimensional Impingement Trajectories

In Figure 5.12, the two-dimensional trajectories are plotted for droplets of various equivalent diameter.   The effect of droplet inertia is apparent, as it was in the case of the cylinders in Section 5.2. Small droplets are swept by the airfoil, while the inertia of the large drops causes them to resist change in direction and they impact the airfoil.   In the example in Figure 5.12, the free-stream velocity was 60 m/sec to the left, and the body thickness was 20 cm.   The atmospheric conditions were typical icing values of 750 mb pressure (equivalent altitude approximately 10,000 feet), -10°C temperature, and gravitational acceleration was neglected.   In the following, these conditions will be assumed unless otherwise noted.

In Figure 5.13, the tangential trajectory to the half body is drawn for a 20-micron droplet.   The initial vertical position of the tangential trajectory defines the height of the impingement window $h_i(D_{eq})$. The impingement window is the zone in which, for a given size, all droplets impact the body. For the symmetrical case of the half body, the impingement zone is centered around the stagnation streamline. Therefore the height of the impingement window $h_i(D_{eq})$ is just twice the separation of the tangential trajectory and the stagnation streamline well ahead of the body.   For non-symmetrical cases, the height of the impingement window is the initial separation between the upper and lower tangential trajectories.

In Figure 5.14, half the height of the impingement window is plotted against D_{eq} for a 20-cm thick half body.   The free-stream velocities studied were 40, 60 and 80 m/sec.   It is interesting to note that

ORIGINAL PAGE IS
OF POOR QUALITY

FIGURE 5.12

DROPLET TRAJECTORIES NEAR HALF BODY

5 MICRONS

10 MICRONS

20 MICRONS

40 MICRONS

HORIZONTAL AXIS (10 CM UNITS)

VERTICAL AXIS (10 CM UNITS)
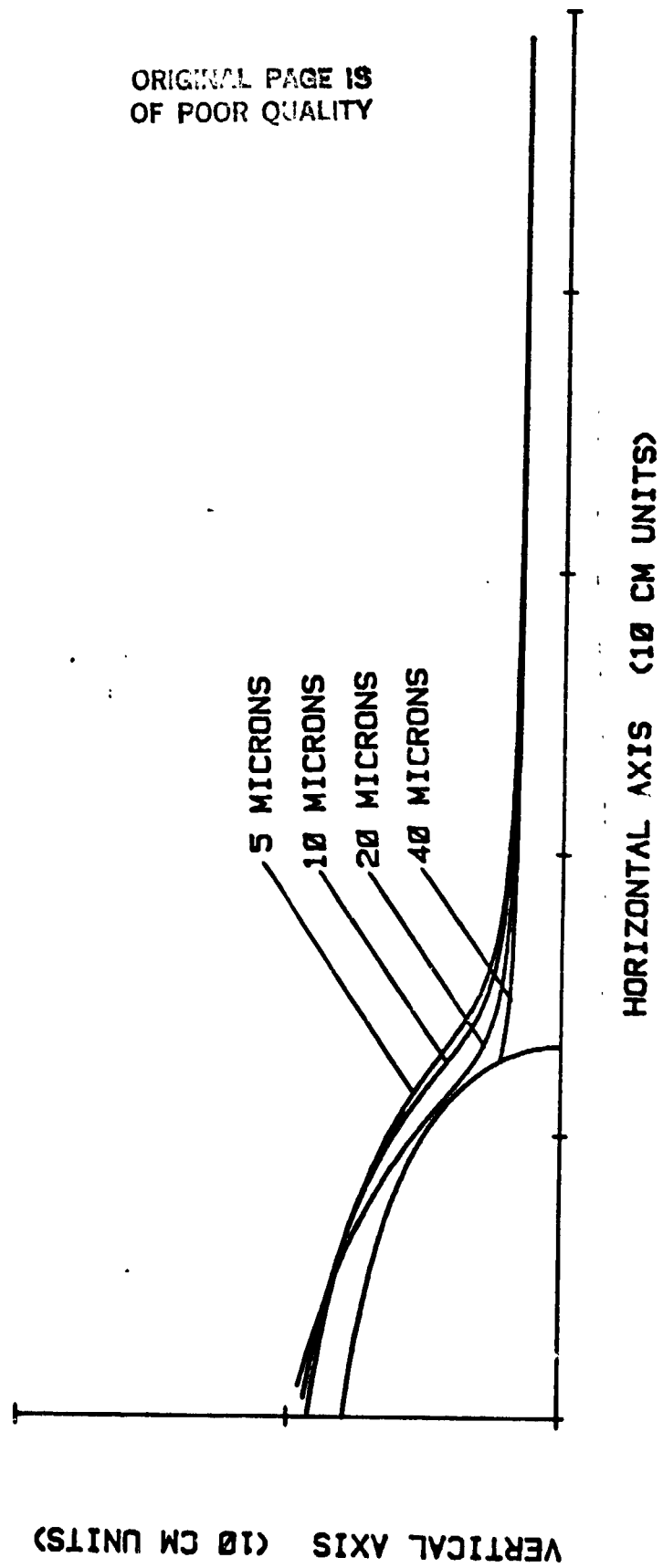
FIGURE 5.13

20 MICRON DROPLET TRAJECTORIES - TANGENTIAL TRAJECTORY

HORIZONTAL AXIS (10 CM UNITS)

VERTICAL AXIS (10 CM UNITS)
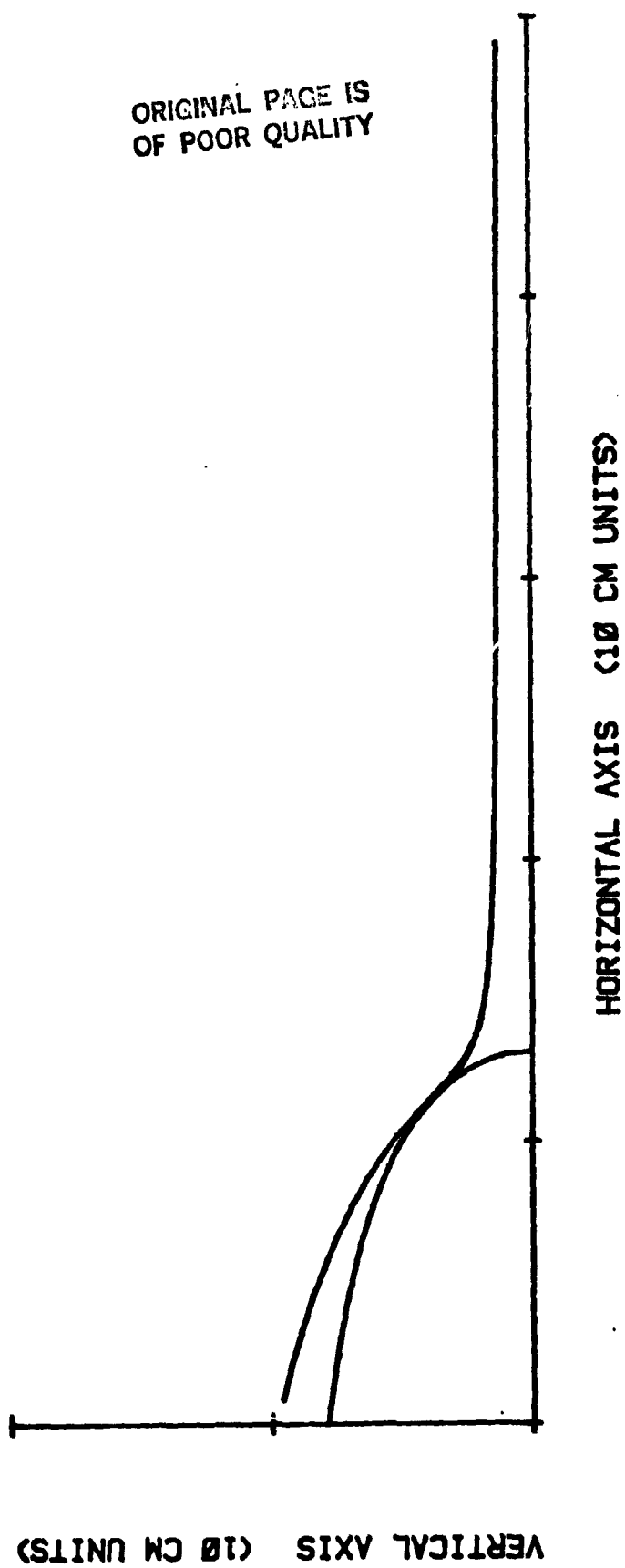
FIGURE 5.14

IMPINGEMENT WINDOW VS. EQUIVALENT DIAMETER
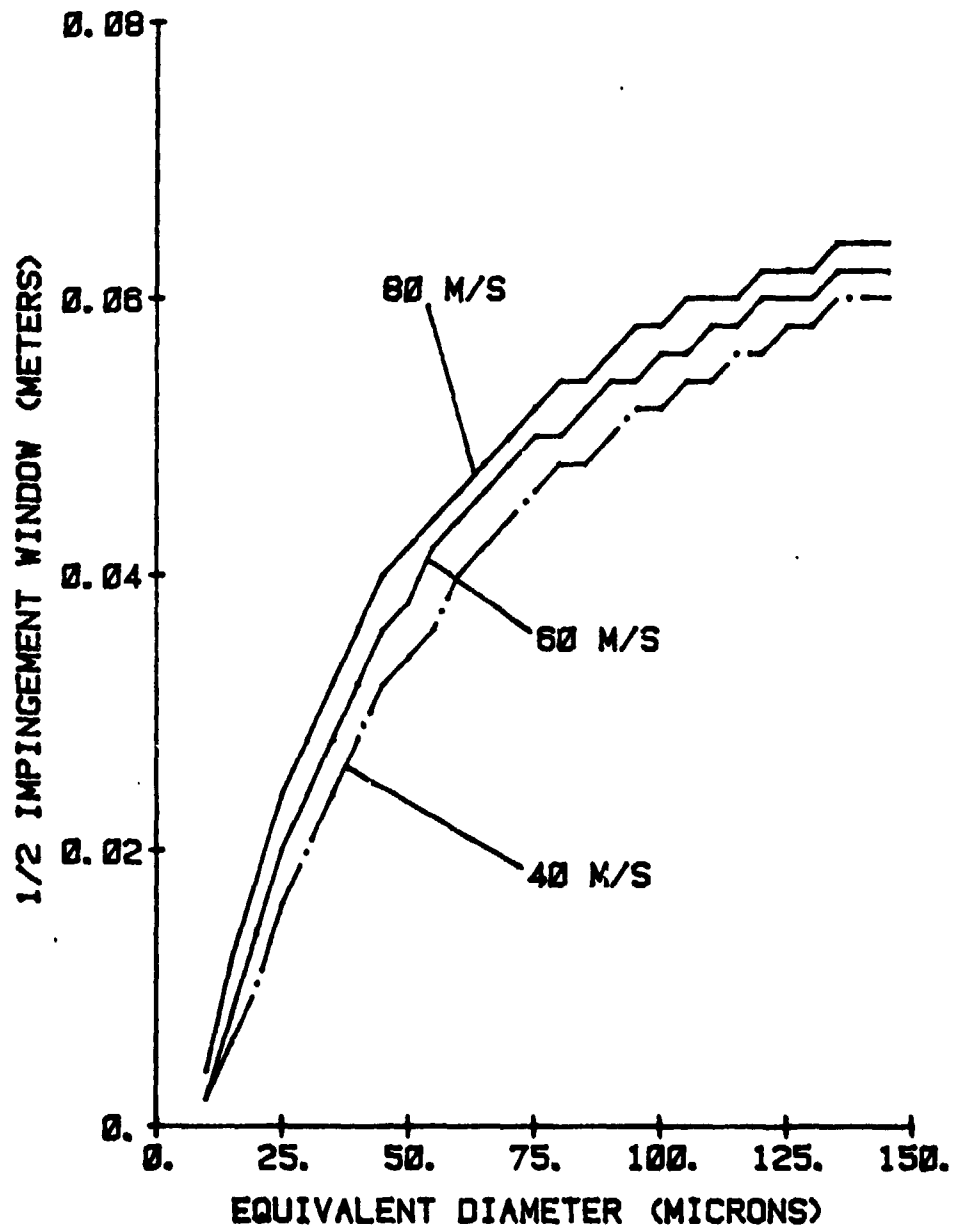
droplets with D_{eq} less than 10 microns are always swept by the half body at these velocities. Above 10 microns, the height of the impinge- ment window increases roughly linearly with diameter up to 100 microns where the $h_i(D_{eq})$ begins to taper to the asymptotic value of 10 cm. This linear behavior was also observed by Brun et al. in their simulations. The slight irregularities in the h_i curves are not physical. They are a remnant of the discrete nature of the sampling algorithm and therefore should be ignored.

A series of trajectories, with varying initial vertical positions, are shown in Figures 5.15 and 5.16 for 20 and 40 micron droplets. The limit of the impingement window is also shown. The 20-micron droplets are clearly more influenced by the flow than their 40-micron counterparts.

The differential collection efficiency of the airfoil $\dfrac{d\eta_c(D_{eq})}{dD_{eq}}$ is the ratio of number of droplets of a given size actually impacting the body to the number of drops of that size initially in the volume swept out by the body. It can be written in terms of the height of the impingement window as

$$\frac{d\eta_c(D_{eq})}{dD_{eq}} = \frac{h_i(D_{eq})}{H} \tag{5.15}$$

where H is the thickness of the body. The differential collection efficiency is related to the total collection efficiency η_c by integrating over the droplet size distribution $f(D_{eq})$

$$\eta_c = \int_0^\infty \frac{d\eta_c}{dD_{eq}} f(D_{eq}) \, dD_{eq} \tag{5.16}$$

FIGURE 5.15

2∅ MICRON DROPLET TRAJECTORIES

Impingement limit = 1.25 cm

HORIZONTAL AXIS (10 CM UNITS)

VERTICAL AXIS (10 CM UNITS)

FIGURE 5.16

10 MICRON DROPLET TRAJECTORIES

Impingement limit = 3.05 cm

HORIZONTAL AXIS (10 CM UNITS)
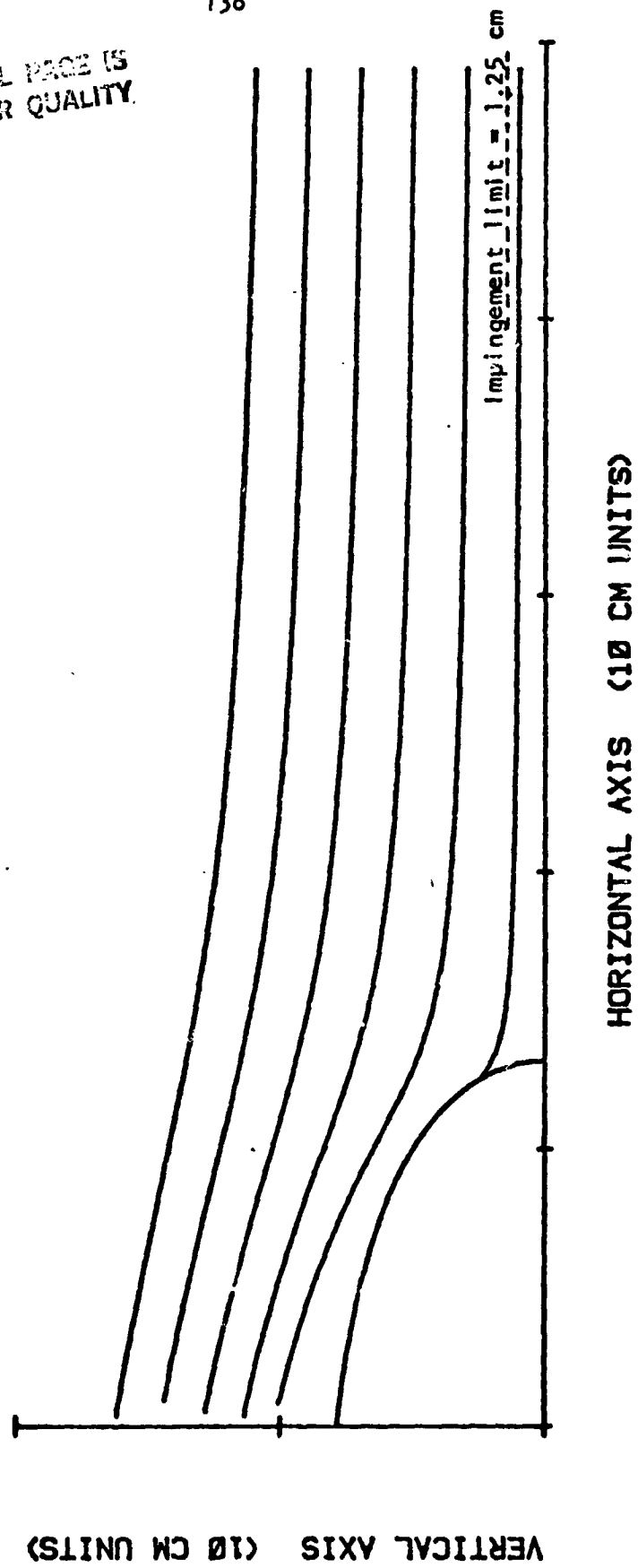
VERTICAL AXIS (10 CM UNITS)
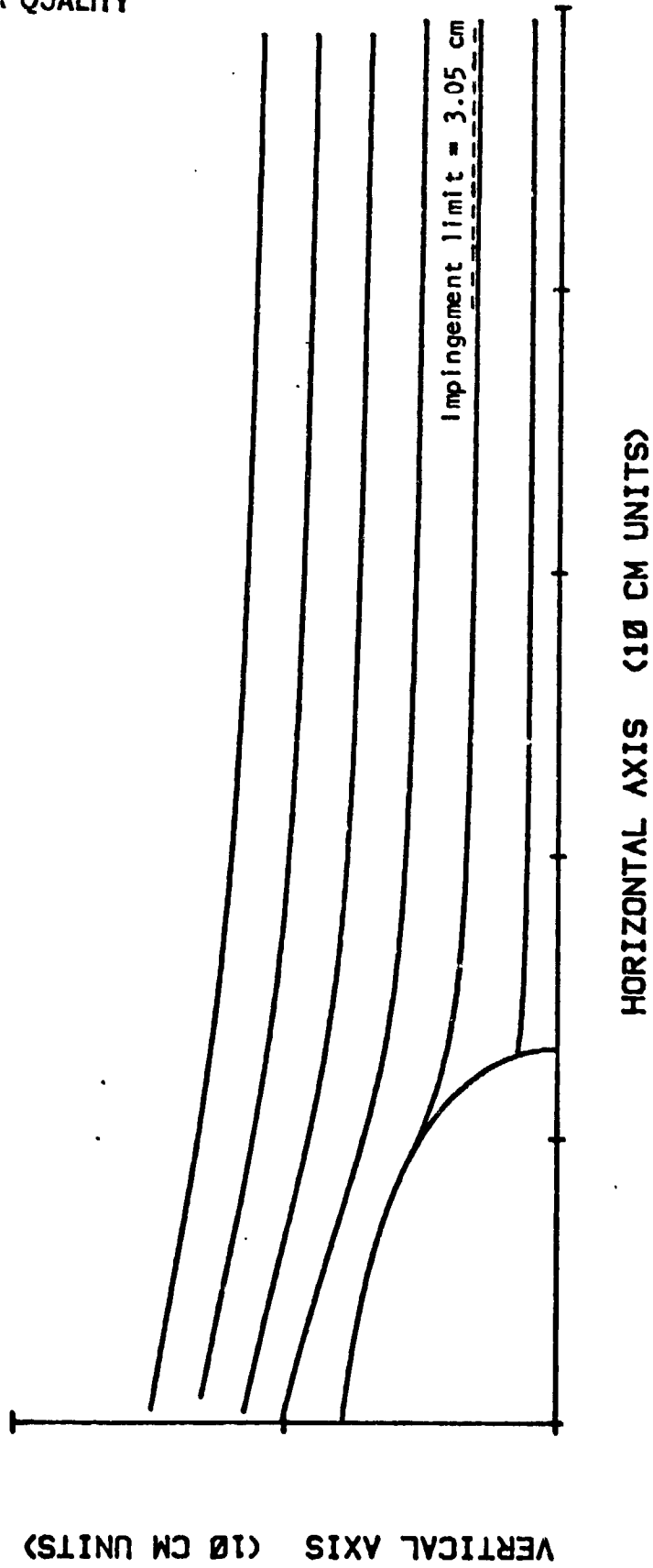
Some typical mid-cloud distribution functions are shown in Figure 5.17. For cumulus clouds, the functions are fairly sharply peaked. The mean droplet diameter is of order 20 microns and tends to increase with the size and age of the cloud. Stratus clouds tend to have broader distribution functions with similar values of the mean droplet diameter. An approximate form of the cloud distribution function is the Khrgian-Mazan distribution [6]

$$f(D_{eq}) = \text{const. } D_{eq}^2 \exp \{3 \, D_{eq}/\overline{D_{eq}} \} \tag{5.17}$$

where $\overline{D_{eq}}$ is the mean effective droplet diameter.

The distribution of impinging mass $\dfrac{dM_c}{dD_{eq}}$ can be calculated from the size distribution function, the differential collection efficiency and the volume of the drop.

$$\frac{dM_c}{dD_{eq}} = V\eta_c \, (D_{eq}) \, f(D_{eq}) \tag{5.18}$$

Combining equations 5.17 and 5.18 and noting that η_c is roughly proportional to D_{eq} for cloud-size droplets, and that the volume V is proportional to D_{eq}^3 yields:

$$\frac{dM_c}{dD_{eq}} = \text{const. } D_{eq}^6 \exp \{3 \, D_{eq}/\overline{D_{eq}}\} \tag{5.19}$$

An example of the Khrgian-Mazan distribution function and the impinging mass distribution function is shown in Figure 5.18 for $\overline{D_{eq}}$ equal to 20 microns. It is interesting to note that the peak value of the

Figure 5.17
FRACTION OF LIQUID WATER WITH DIAMETER SMALLER THAN D_{eq}

TYPICAL DISTRIBUTIONS
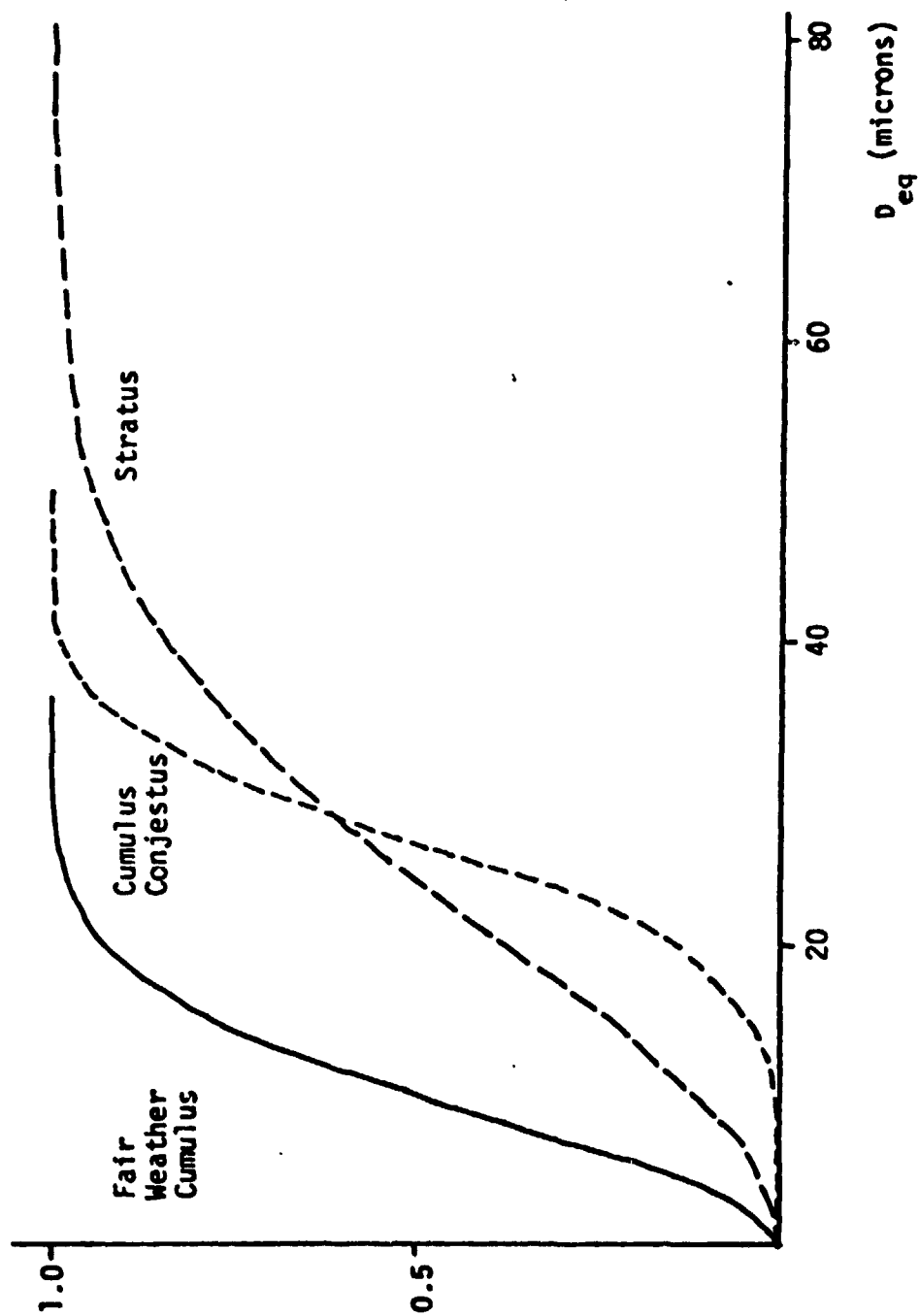
Figure 5.18

KHRGIAN-MAZAN DISTRIBUTION (Arb. Units)

--- 1. Drop size in cloud. Mean diameter 20 microns.

—— 2. Impinging mass distribution.

D_{eq} (microns)
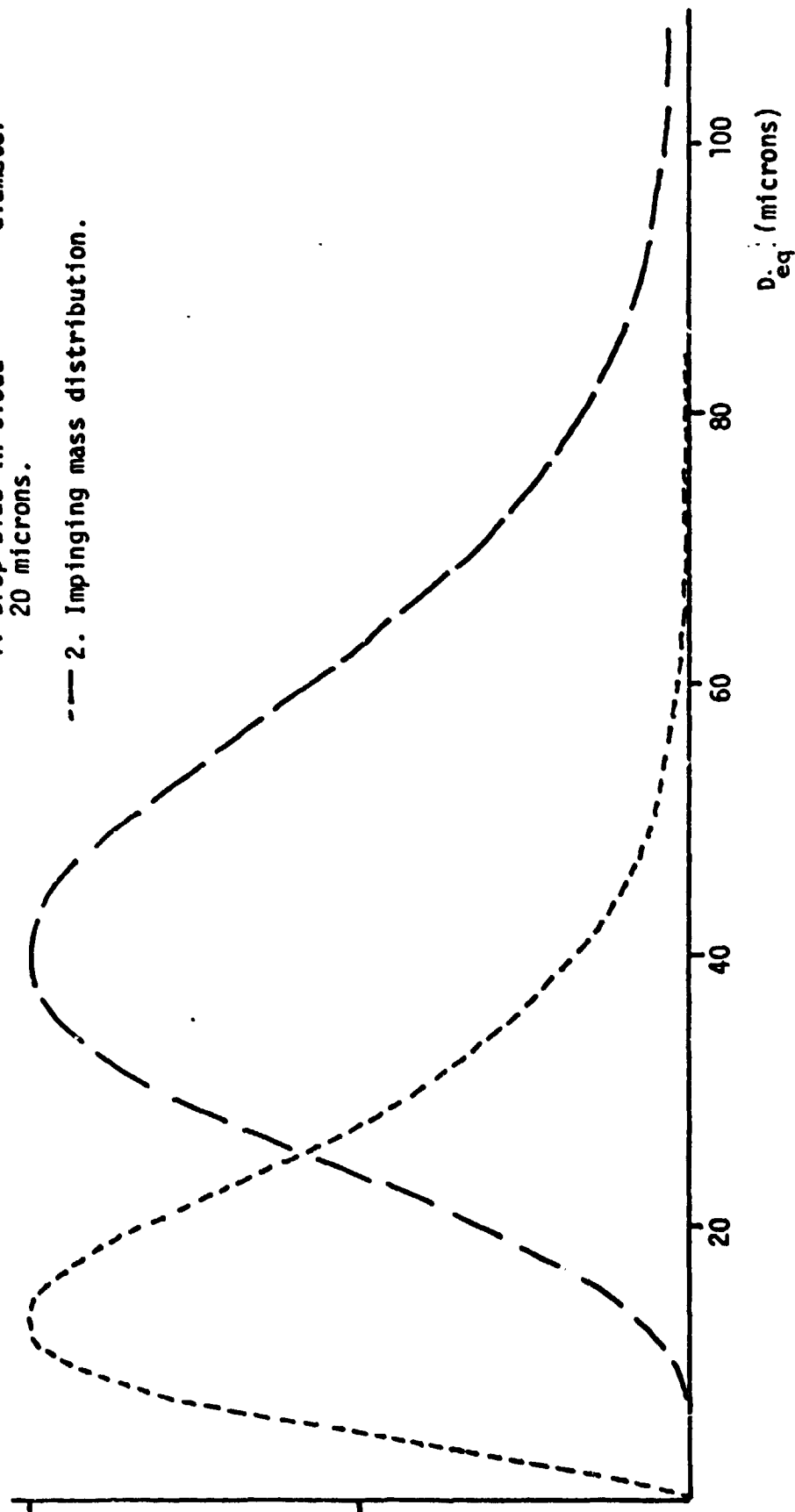
mass distribution function occurs at 40 microns, which is twice
the mean diameter $\overline{D_{eq}}$ in the cloud. Indeed, the extreme value
condition for equation 5.19 yields

$$D_{eq} \Big|_{max \frac{dM_c}{dD_{eq}}} = 2 \overline{D_{eq}} \tag{5.19}$$

For raindrops, the differential collection efficiency is approxi-
mately unity. The accepted size distribution function for rain
is the Marshall-Palmer distribution,[63] further refined by Atlas.[64]

$$f(D_{eq}) = \text{const. exp} \{-3.67\, D_{eq}/\overline{D_{eq}}\} \tag{5.20}$$

This results in an impinging mass distribution of

$$\frac{dM_c}{dD_{eq}} = \text{const.}\, D_{eq}^3 \exp\{-3.67\, D_{eq}/\overline{D_{eq}}\} \tag{5.21}$$

with the mean value of D_{eq} for rain being of order several milli-
meters.

5.3.2   Kinematics of Droplets on the Stagnation Stream. ne

The general effect of the half body flow field on the kinematics
of impinging droplets can be observed in the case of droplets which
flow on the stagnation streamline. Droplets on the stagnation
streamline are particularly convenient, in that the kinematics are
essentially one-dimensional.

In Figure 5.19, the acceleration of droplets is plotted against

FIGURE 5. 19

ACCELERATION VS DISTANCE ON STAGNATION STREAMLINE
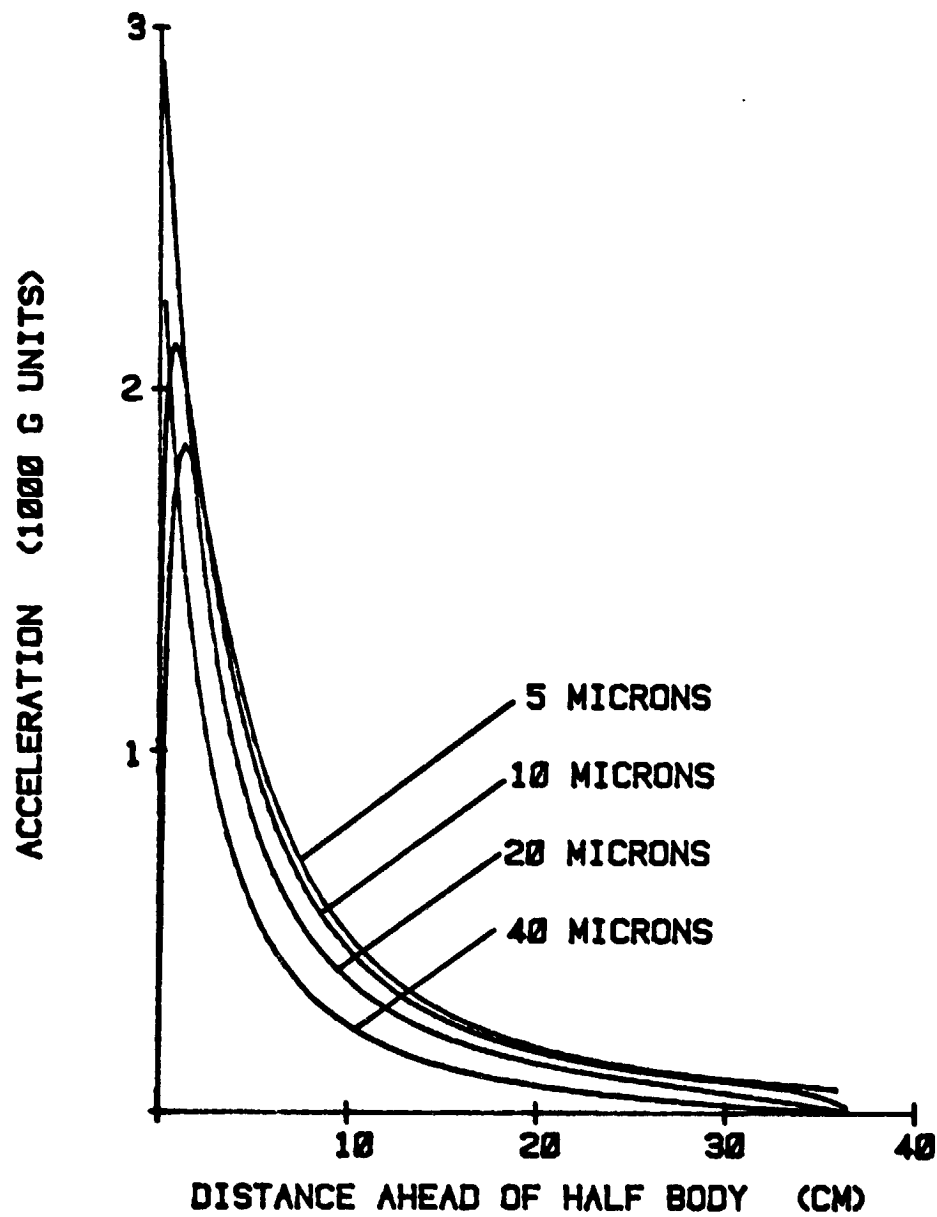
distance ahead of the half body, for equivalent diameters of 5, 10, 20 and 40 microns, for the flow conditions listed in Section 5.3.1. The acceleration, which is actually a deceleration in that it acts to slow the droplets, is the result of the slowing of the flow due to the pressure gradient ahead of the body. Droplets flowing towards the airfoil begin to feel some acceleration 30 to 40 cm ahead of the body. The acceleration increases until either the larger drops (20 and 40 microns) impact the body, or the smaller drops (5 and 10 microns) slow to approximately the flow velocity a few cm ahead of the body. The maximum value of the acceleration is on the order of several thousand g units.

The high values of acceleration that the droplets are subject to, result in two major effects. The first is hydrodynamic, in that the effective accelerated diameter $(\frac{a}{g})^{1/2} D_{eq}$, discussed in Chapter 4, is increased considerably. The value of $(\frac{a}{g})^{1/2}$ is plotted against distance in Figure 5.20, for the droplets described above. The peak values of 40 to 55 are observed, implying that factors such as drop deformation and possibly instability will become important. It should be noted that the droplets in the example in Figure 5.20 remain below the instability threshold for $(\frac{a}{g})^{1/2} D_{eq}$ of approximately 1 cm.

The second effect of the strong acceleration is to increase the dwell time of droplets in the region just ahead of the body. This can be seen in Figure 5.21 where the droplet velocity is plotted. The droplets are seen to slow appreciably several centimeters ahead of the airfoil. The dwell time and, assuming a uniform external droplet

FIGURE 5.20

DIAMETER INCREASE DUE TO ACCEL ON STAGNATION STEAMLINE
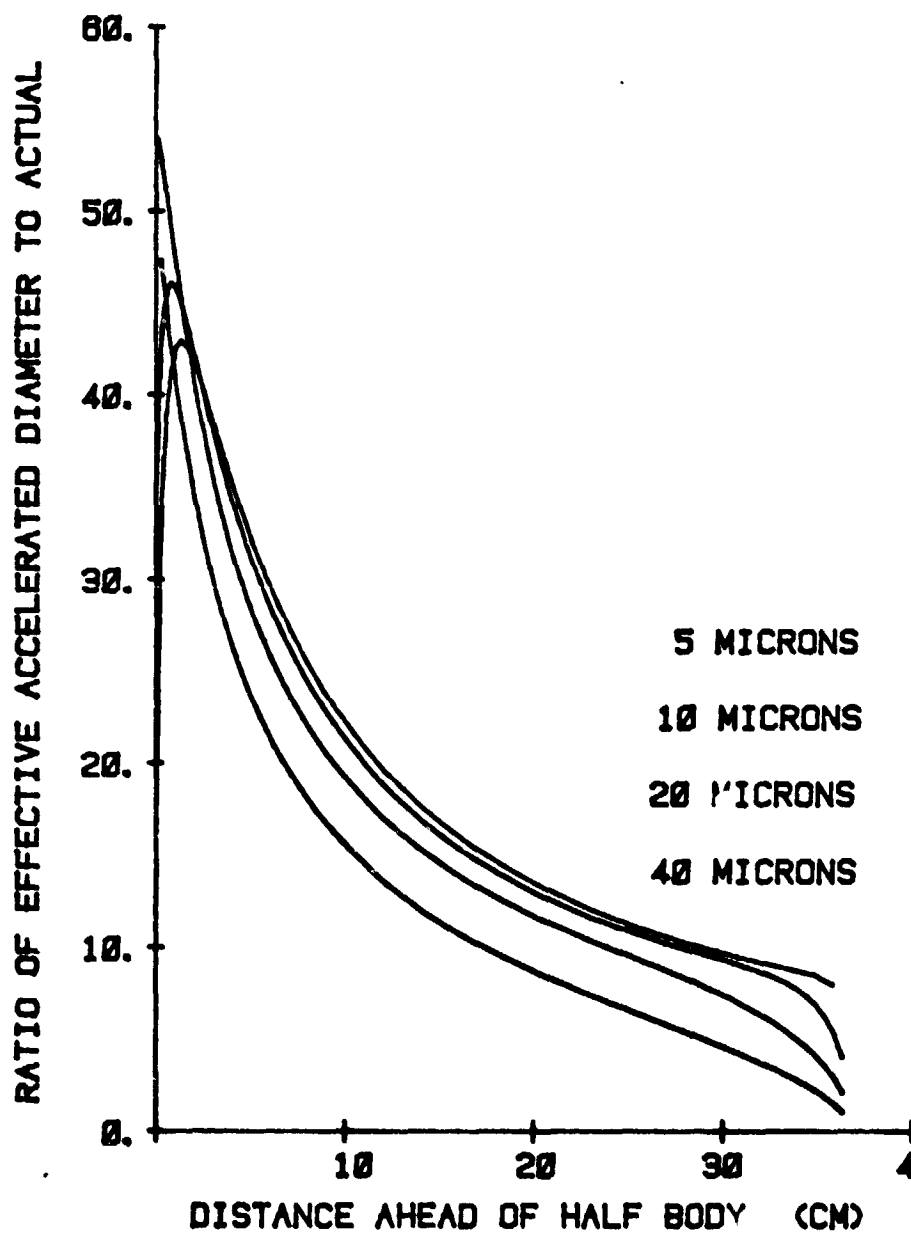
FIGURE 5.21

VELOCITY VS DISTANCE ON STAGNATION STREAMLINE
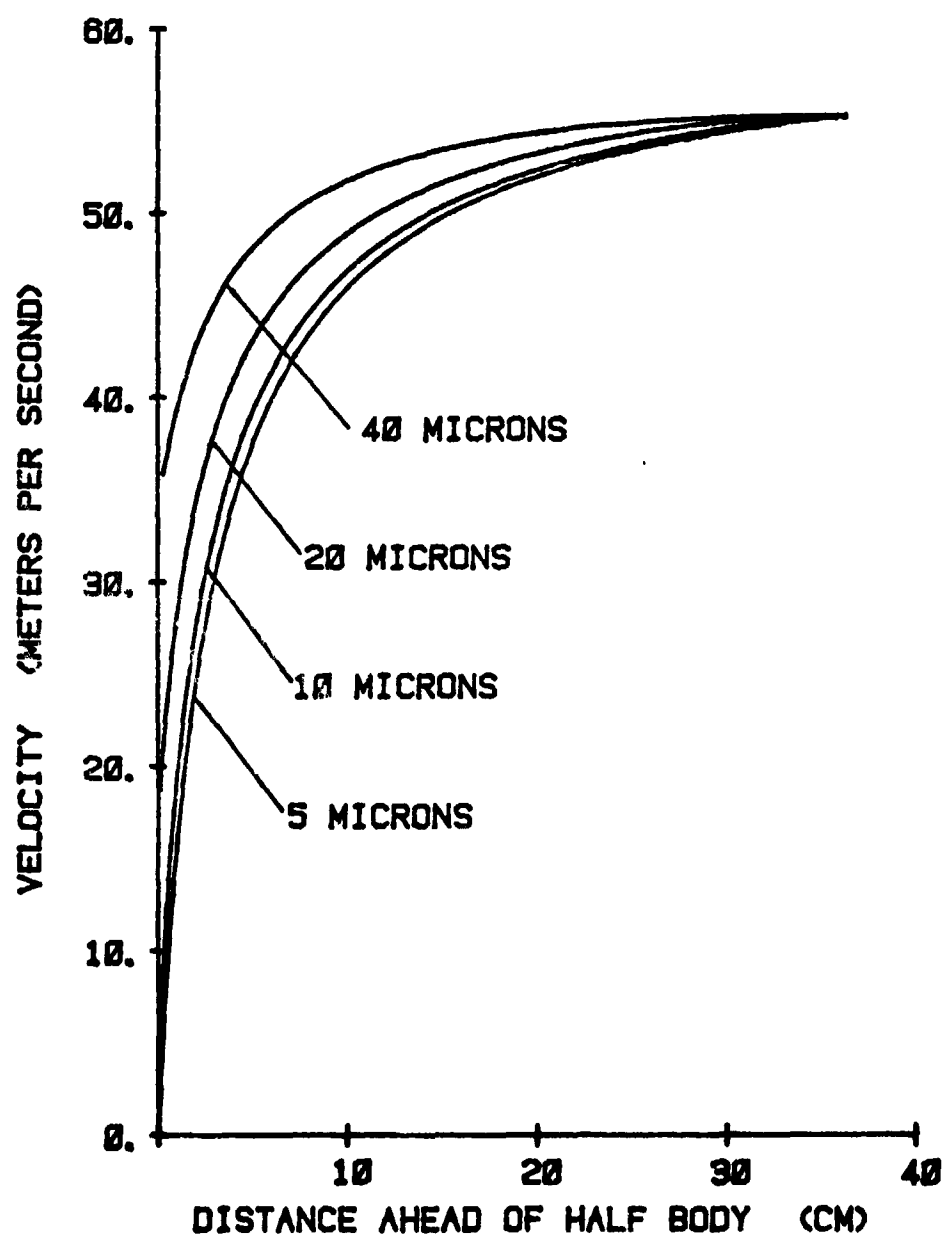
field, the droplet concentration, will therefore increase in this region.

It should be noted that the observations made for droplets on the stagnation streamline are by no means limited to that special case. Droplets in the general region ahead of the airfoil should exhibit similar behavior, although the direction of acceleration will be variable. In fact, the zone of maximum acceleration is actually located slightly off the stagnation streamline just ahead of the body.

5.3.3 Additional Simulations

In this section, some additional simulations are presented to illustrate the flexibility of the code. The first case of interest was that of a large drop impacting the body. As was noted in Section 5.2, the large drop splashes into a collection of smaller droplets with velocities of order one-tenth of the free-stream velocity directed radially away from the point of first impact.

The splash was simulated by assuming that the point of impact was the stagnation point. Simulation droplets were initiated at this point with initial velocities of 6 m/sec (one-tenth of the 60 m/sec free-stream value). The angle between the initial velocity and the stagnation streamline was varied from 0° to 90°. Examples of the resulting trajectories are shown in Figure 5.22 for the cases of 30°, 60°, and 90°. For the 60° and 90° trajectories, the droplets are clearly swept away by the flow. For the 30° trajectories, the droplets return back and just grazes the body approximately 1 cm along the body.

The origin of the double-horned icing shape shown in Figure 5.10b

FIGURE 5. 22

SPLASH TRAJECTORIES – 20 MICRON DROPLETS
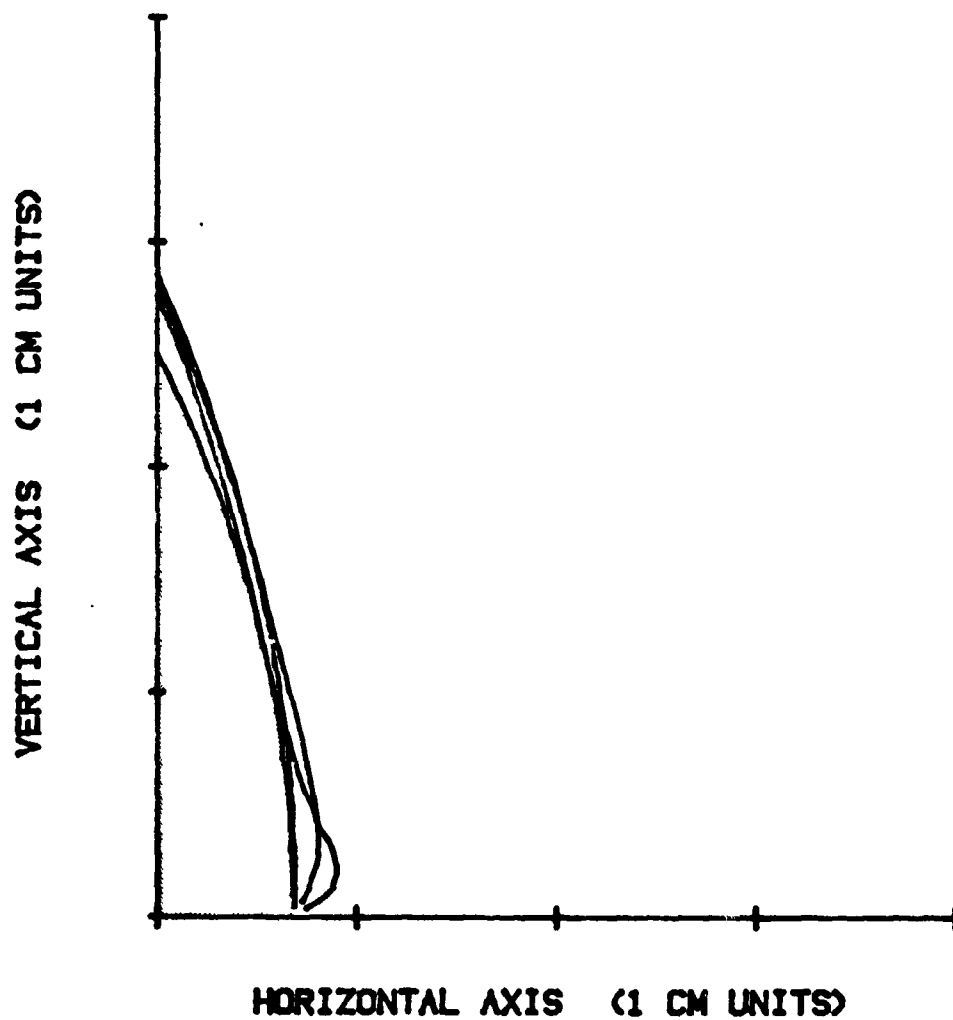
can be inferred from the simulation results.   If the droplets don't
freeze immediately on impact, most of the residual splash droplets
will be swept away until some ice begins to form off the center line.
The splash droplets, which are moving essentially tangentially to the
body, will impact at this point and the horn will begin to grow.
The second horn is simply a manifestation of the flow symmetry about
the stagnation streamline.

Another case of interest is the effect on droplet trajectories
of blowing air out the leading edge of the airfoil.   Figure 5.23
shows a series of 40-micron trajectories with and without blowing.
The blowing velocity at the leading edge is 36 m/sec in this case,
and the free-stream velocity is 60 m/sec.   From Figure 5.23 it is
clear that it is indeed possible to prevent droplets of a given size
from impinging onto an airfoil by blowing.   The feasibility of ice
prevention by such a technique requires an assessment of the aerodynamic
penalty, if any, resulting from such blowing and an assessment of the
power required.

FIGURE 5. 23

40 MICRON DROPLET TRAJECTORIES

VERTICAL AXIS (10 CM UNITS)

HORIZONTAL AXIS (10 CM UNITS)
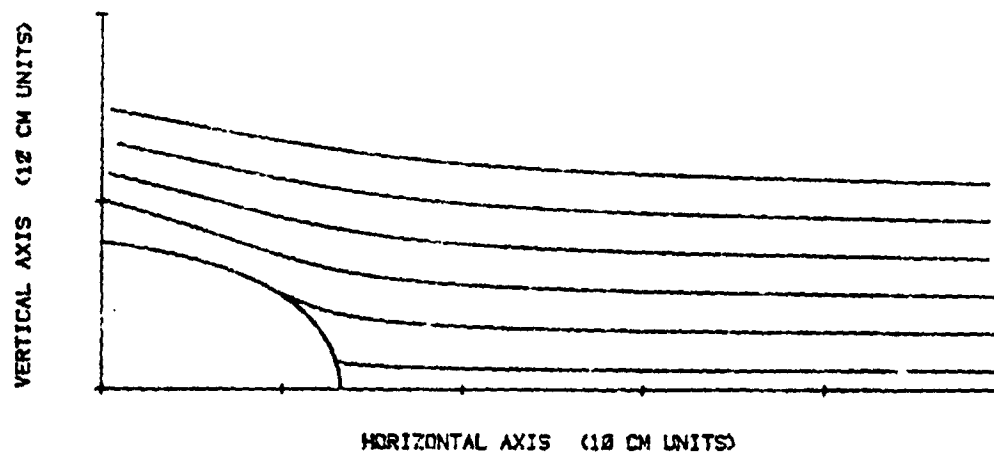
40 MICRON TRAJECTORIES WITH LEADING EDGE BLOWING

Blowing velocity = 36 m/s

VERTICAL AXIS (10 CM UNITS)

HORIZONTAL AXIS (10 CM UNITS)
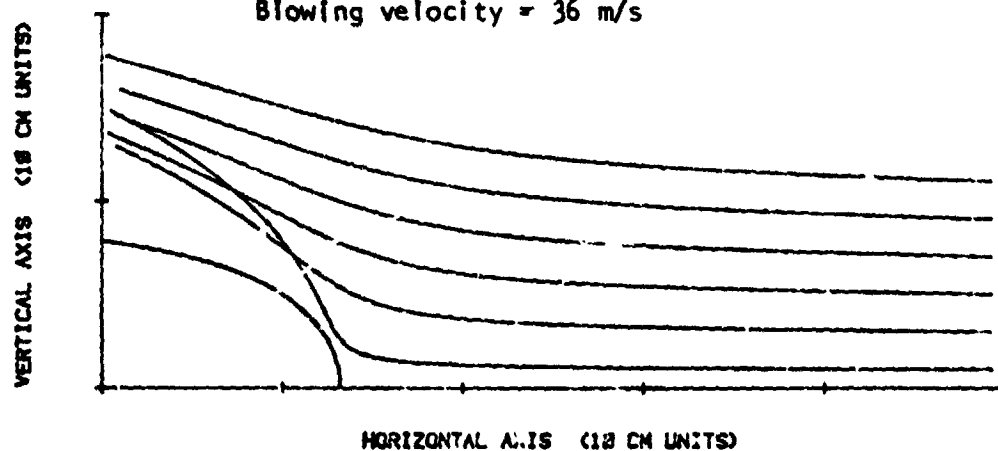
CHAPTER 6

COMPUTER SIMULATIONS OF DROPLET HEATING

The problem of heating water droplets by microwave radiation in the vicinity of an airfoil is studied in this chapter by means of a computer simulation. The simulation is, essentially, an amalgamation of the results of the preceding chapters. In Section 6.1 the structure of the code is described. Section 6.2 discusses the model used to maintain droplet energy balance in the simulation. Finally, in Section 6.3, some results of the droplet heating simulation are presented.

6.1 Description of the Simulation

In this section the droplet heating code is described. The code was written primarily as a means for obtaining analysis and design criteria for aircraft anti-icing schemes which employ microwave preheating of water droplets prior to impact. As a consequence, the results of the code presented in ths chapter center around droplets which are heated by microwave fields as they flow in the vicinity of an airfoil. The code is, actually, more general than this specific application and could just as easily be applied to problems such as the extinction of solar radiation by cloud droplets or the attenuation of radar or communication signals in the atmosphere.

A flow diagram of the code is shown in Figure 6.1. The primary structure of the heating code is the droplet trajectory code discussed in Section 5.1. Two sections are added to the trajectory code to account for droplet heating. The first accounts for the heating effect of the microwave field by calculating the Poynting flux at the droplet location,

Initial position Ambient temp.
Initial velocity Ambient pressure
Droplet size

Calculate acceleration
$$\vec{a} = \frac{-C_d \, Re}{24 \, K_a} (\vec{v} - \vec{u})$$

Flow field

Body shape
Body size
Free stream vel.

1st Order Euler Int. Scheme
$$\vec{x}_{i+1} = \vec{v}_i \Delta t + \vec{x}_i$$
$$\vec{v}_{i+1} = \vec{a}_i \Delta t + \vec{v}_i$$
yeilds trajectories

Step time
increment
Δt

Is the drop hydrodynamically stable? no

yes

I = i+i

Calculate absorbtion cross-section σ_a and Poynting flux at x_i

Electromagnetic field model

Increment droplet parameters
$$T_{d,i+1} = \left(\frac{dT_d}{dt}\right)_i \Delta t + T_i$$
$$M_{i+1} = \left(\frac{dM}{dt}\right)_i \Delta t + M_i$$
$$f_{w,i+1} = \left(\frac{df_w}{dt}\right)_i \Delta t + f_{w,i}$$

Heat transfer loss rates

no Does droplet hit the body at time t_{i+1}

yes

Output trajectories and temperatures

Figure 6.1 Flow diagram for heating code.

given some model of the electromagnetic field and calculating the droplet absorption cross-section.

The cross-section is calculated by first assuming Rayleigh absorption (equation 2.17). The code then checks for drop deformation and other non-Rayleigh effects and corrects the cross-sections by the multiplicative factors discussed in Section 3.1.1. The following non-Rayleigh effects are included in calculating the absorption cross-section σ_a

large droplets (Mie theory)

non-spherical droplets (Gans theory)

phase change effects

thermal effects on the dielectric constant

In the above, the magnitude of the drop axis ratio A/B is taken to be 50% of the maximum transient deformation limit discussed in Section 3.3.

Given the above, it is possible to calculate the rate of absorption of microwave energy by the drop as

$$\frac{dQ_{rf}}{dt} = \sigma_a S \qquad (6.1)$$

where S is the magnitude of the Poynting vector at the drop location.

The second additional section in the heating code calculates the incremental temperature change over one time step Δt by considering the total heat budget of the drop, including such effects as evaporation, melting, diffusive heat transfer and ventilation, along with the microwave heating of equation 6.1. The heat budget of a drop is discussed in more detail in Section 6.2.

Consideration of the droplet heat budget yields the rate of change of such droplet parameters as the droplet temperature, T_d, the droplet

mass, M, and the droplet mass fraction, f_w.   These parameters are

integrated at each time step Δt by the Euler integration scheme

discussed in Section 5.1

$$T_{d,i+1} = (\frac{dT_d}{dt})_i \Delta t + T_{d,i} \tag{6.2}$$

$$M_{i+1} = (\frac{dM}{dt})_i \Delta t + M_i \tag{6.3}$$

$$f_{w,i+1} = (-\frac{df_w}{dt})_i \Delta t + f_{w,i} \tag{6.4}$$

The droplet parameters T_d, M and f_w are therefore free-running

parameters in the heating code.

The initial value of T_d is generally assumed to be the ambient

temperature T_a.   The initial mass fraction and droplet mass are input

parameters in the code.   The droplet mass is represented by the diameter

of the water sphere of equivalent mass D_{eq}.

$$M_w = \frac{4}{3}\pi\rho_w(\frac{D_{eq}}{2})^2 \tag{6.5}$$

As in the trajectory code, the droplet parameters and position are

incremented through the loop until the droplet either impacts the body,

misses the body or becomes unstable.

The code parameters which will be assumed in the following, unless

otherwise noted, are

    Body = half-body 20 cm thick

    Free Stream Velocity = 60 m/sec

    Atmosphere = icing conditions (750 mb, $-20^{\circ}C$)

The electromagnetic field model and the coordinate system used in the code are shown in Figure 6.2. The field consisted of a bound surface wave which propagated along the leading edge of the airfoil perpendicular to the flow. The field strength was exponentially decaying with distance ahead of the airfoil and had a $\cos^2\theta$ angular dependence centered about the stagnation streamline. The field direction is assumed to be perpendicular to the radial direction in Figure 6.2. Therefore

$$|\vec{E}| = E_0 \exp\{-(r - x_s)/\ell\} \cos^2 \left(\frac{\pi}{2}\frac{\theta}{\theta_0}\right)^2 \tag{6.6}$$

where

$$\theta = \arctan \frac{x}{y} \tag{6.7}$$

$$r = \sqrt{x^2 + y^2} \tag{6.8}$$

θ_0 is a reference angle defining the angular width of the field, E_0 is the maximum electric field strength at the surface, ℓ is the exponential decay length of the field and x_s is the x coordinate of the leading edge of the half body.

On the stagnation streamline, the electric field simplifies to

$$|\vec{E}| = E_0 \exp \{-(x - x_s)/\ell\} \tag{6.9}$$

which is the exponential decay associated with a planar dielectric surface waveguide.[15] The exponentiation length ℓ of such waveguides can be controlled by the thickness of the dielectric coating. The effect of varying the above electromagnetic field parameters and the wavelength λ is studied in Section 6.3.
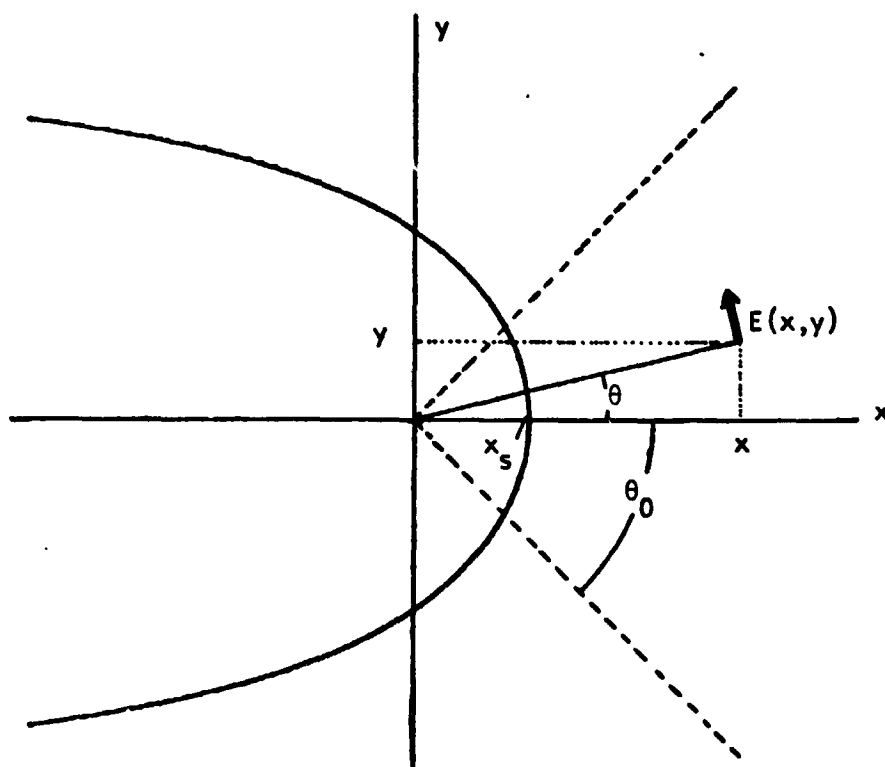
Figure 6.2   Coordinate system used for the electromagnetic
field model.

6.2 Droplet Energy Balance

In order to calculate the rate of change of such droplet parameters as temperature, T, droplet mass, M, and mass fraction, f_w, it is necessary to observe the heat budget of the drop. The heat budget is

$$\frac{dQ_r}{dt} = \frac{dQ_{rf}}{dt} + \frac{dQ_{evap}}{dt} + \frac{dQ_{melt}}{dt} + \frac{dQ_{td}}{dt} \qquad (6.10)$$

where

$$\frac{dQ_t}{dt} = \text{total heat change in drop} \qquad (6.11)$$

$$\frac{dQ_{rf}}{dt} = \text{heat change due to radiation} \qquad (6.12)$$

$$\frac{dQ_{evap}}{dt} = \text{heat change due to evaporation} \qquad (6.13)$$

$$\frac{dQ_{melt}}{dt} = \text{heat change due to melting} \qquad (6.14)$$

$$\frac{dQ_{td}}{dt} = \text{heat change due to thermal diffusion} \qquad (6.15)$$

The total rate of change of heat is related to the change in droplet temperature by the specific heat at constant pressure $(C_p = 1 \text{ cal/gm}^\circ C = 4.186 \times 10^7 \text{ erg/gm}^\circ C)$ and the mass M by

$$\frac{dQ_t}{dt} = C_p M \frac{dT}{dt} \qquad (6.16)$$

The rate of change of heat due to radiational heating was written in Section 6.1 as

$$\frac{dQ_{rf}}{dt} = \sigma_a S \qquad (6.17)$$

where σ_a is the absorption cross-section of the drop and S is the Poynting flux.

The change of heat due to droplet evaporation is

$$\frac{dQ_{evap}}{dt} = L_{wv} \frac{dM}{dt} = L_{wv} \bar{f}_v \left(\frac{dM}{dt}\right)_0 \qquad (6.18)$$

where

L_{wv} = the specific heat of evaporation of water

(L_{wv} = 600 cal/gm = 2.5 x 10^{10} erg/gm)

$\frac{dM}{dt}$ = the rate of change of mass due to vapor diffusion

$\left(\frac{dM}{dt}\right)_0$ = the value of $\frac{dM}{dt}$ for a stationary drop

$\bar{f}_v$ = the ventilation coefficient which accounts for the enhanced vapor diffusion due to air flow around the droplet

The value of $\left(\frac{dM}{dt}\right)_0$ may be found by solving the steady-state diffusion equation

$$\frac{\partial \rho_v}{\partial t} = D_v \vec{\nabla}^2 \rho_v \qquad (6.18)$$

where ρ_v is the water vapor density and D_v is the vapor diffusion coefficient. Calculating the rate of flux of water vapor through some closed surface around the drop yields, for spherical droplets[6]

$$\left(\frac{dM}{dt}\right)_0 = 4\pi D_v \left(\frac{D_{eq}}{2}\right) (\rho_{v,a} - \rho_{v,d}) \qquad (6.20)$$

where $D_{eq}/2$ is the radius of the drop and $\rho_{v,a}$, $\rho_{v,d}$ are the ambient and droplet surface vapor densities. If the effect of curvature on $\rho_{v,d}$ can be ignored and the ambient atmosphere is saturated with

water vapor, then $\rho_{v,a}$ and $\rho_{v,d}$ are simply the saturation vapor pressures over water and depend only on temperature appropriate to the pressure to be found.   Values of saturation vapor pressure versus temperature are plotted in Figure 6.3 from the Smithsonian Meteorological Tables.[60]

Values of the ventilation coefficient $\bar{f}_v$, which is the increase in vapor diffusion due to airflow by the drop, have been determined empirically by Beard and Pruppacher[65] to be

$$\bar{f}_v = 0.78 + 0.308 \; N_{sc,v}^{1/3} \; Re^{1/2} \tag{6.21}$$

where Re is the Reynolds number and $N_{sc,v}$ is the Schmidt number

$$N_{sc,v} = \frac{\mu}{\rho_a D_v} \tag{6.22}$$

μ is the dynamic viscosity of air and ρ_a is the density.   The value of the vapor diffusion is taken to be[66]

$$D_v = 0.211 \; (\frac{T_a}{273^{\circ}K})^{1.94} \; (\frac{1013 \; mb}{P_a}) \tag{6.23}$$

where T_a and P_a are the ambient values of temperature and pressure.

The heat loss from the drop can be found by noting that the thermal and vapor diffusion equations have identical form.   Therefore, by analogy to the vapor diffusion case,

$$\frac{dQ_{td}}{dt} = \bar{f}_h \; 4\pi k_a (\frac{D_{eq}}{2}) \; (T_a - T_d) \tag{6.24}$$

where k_a is the thermal diffusion coefficient taken to be 2.4×10^3 erg/cm sec$^{\circ}$C in air and $\bar{f}_h$ is the heat ventilation coefficient, which is taken to be equivalent to $\bar{f}_v$ following the example of Pruppacher.[6]

Figure 6.3   Saturation vapor pressure over water
versus temperature.
(from Smithsonian Meterological Tables)
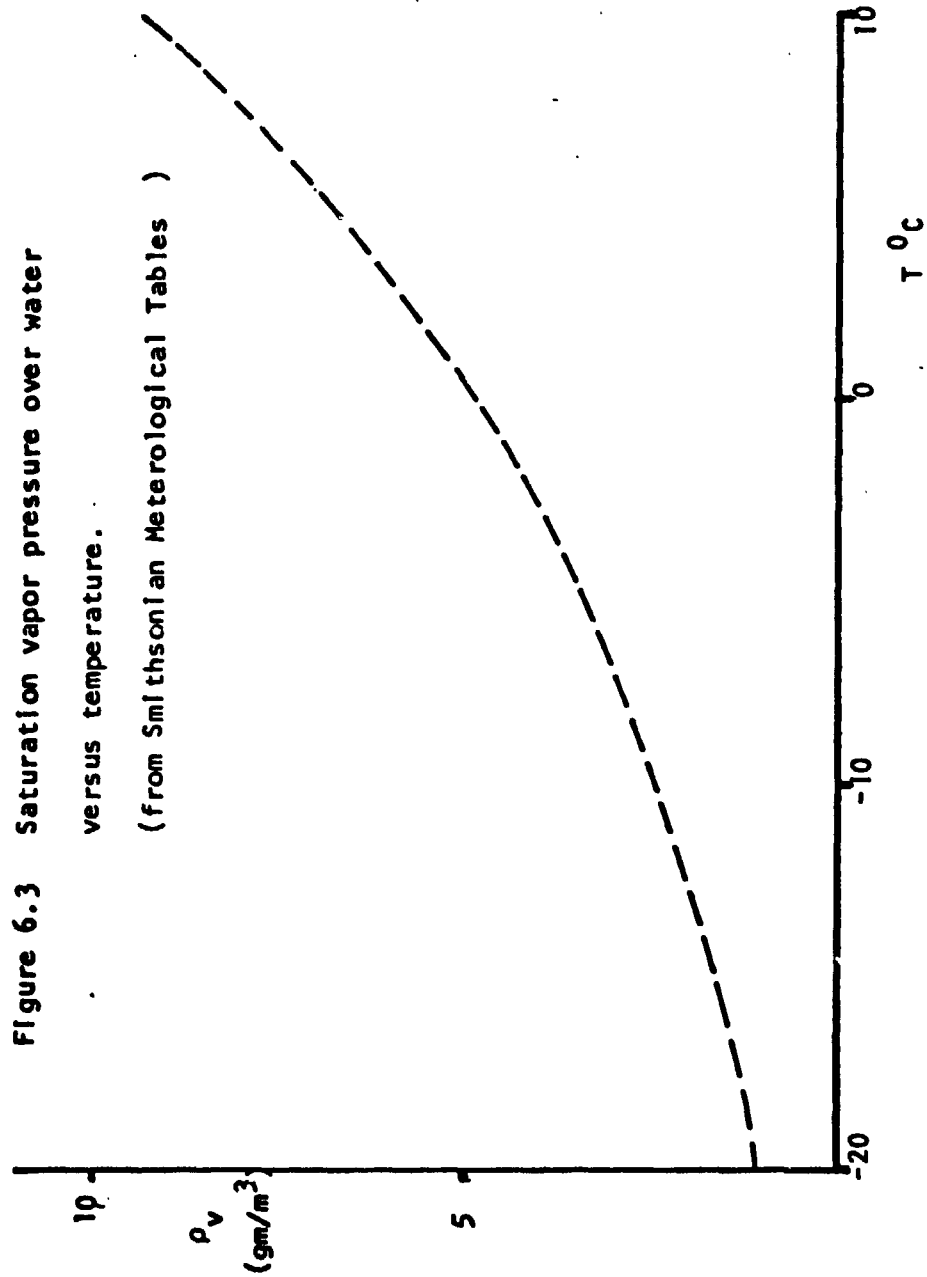
The change of heat due to melting of ice within the drop can be related to the change in mass fraction f_w by the latent heat of fusion L_{iw} (L_{iw} = 80 cal/gm = 3.36 x 10^9 erg/cm)

$$\frac{dQ_{melt}}{dt} = L_{iw}M \frac{df_w}{dt} \tag{6.25}$$

In the heating code, no melting is assumed to take place until the droplet is at or above 0°C, at which point the temperature remains constant and all excess goes into melting ice until f_w becomes unity.

By considering the above, it is possible to write the rate of change equations for the various parameters of interest

$T_d \neq 0$

$$\frac{dT_d}{dt} = \frac{1}{C_p M} [\sigma_a S + 4\pi(D_{eq}/2) \, \overline{f}_v (L_w \, D_v(\rho_{v,a} - \rho_{v,d}) + k_a(T_a - T_d))] \tag{6.26}$$

$T_d = 0$

$$\frac{df_w}{dt} = \frac{1}{L_{iw}} [\sigma_a S + 4\pi(D_{eq}/2) \, \overline{f}_v (L_{wv} D_v(\rho_{v,a} - \rho_{v,d}) + k_a(T_a - T_d))] \tag{6.27}$$

$$\frac{dM}{dt} = 4\pi(D_{eq}/2) \, \overline{f}_v \, L_{wv} D_v(\rho_{v,a} - \rho_{v,a}) \tag{6.28}$$

In order to check the droplet parameter section of the code, the cooling and evaporation of a 1 mm droplet was simulated. The droplet was given an initial temperature of 20°C in an ambient saturated atmosphere of 0°C. The two cases of a stationary, unventilated drop and a freely-falling, ventilated drop were simulated. The results are shown in Figures 6.4 and 6.5. The ventilated drop is seen to equilibrate in several seconds, while the unventilated drop requires

FIGURE 6.4

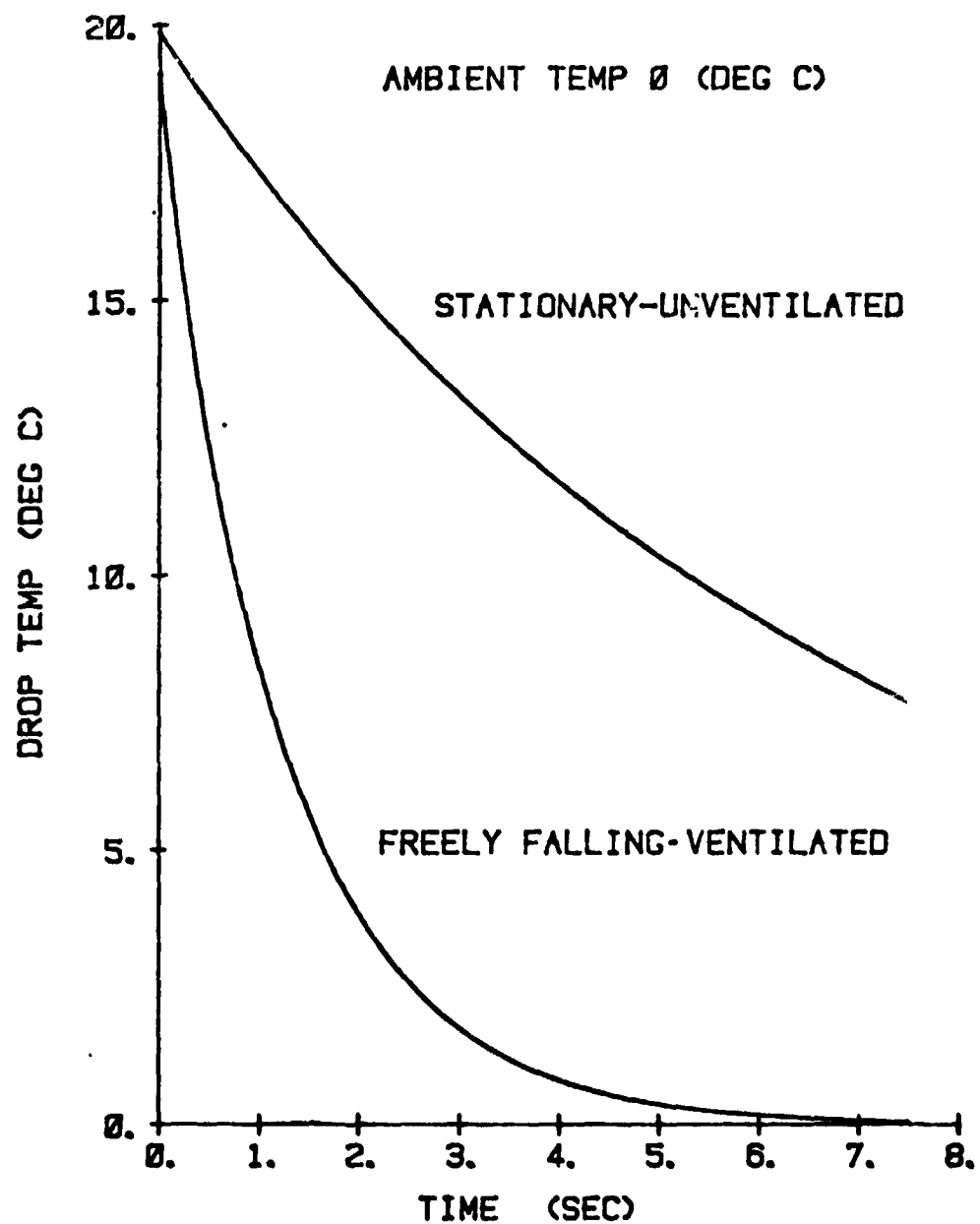COOLING OF FALLING AND STATIONARY 1 MM DROP

FIGURE 6.5

MASS CHANGE FOR COOLING DROP   (INITIALLY 20 C)
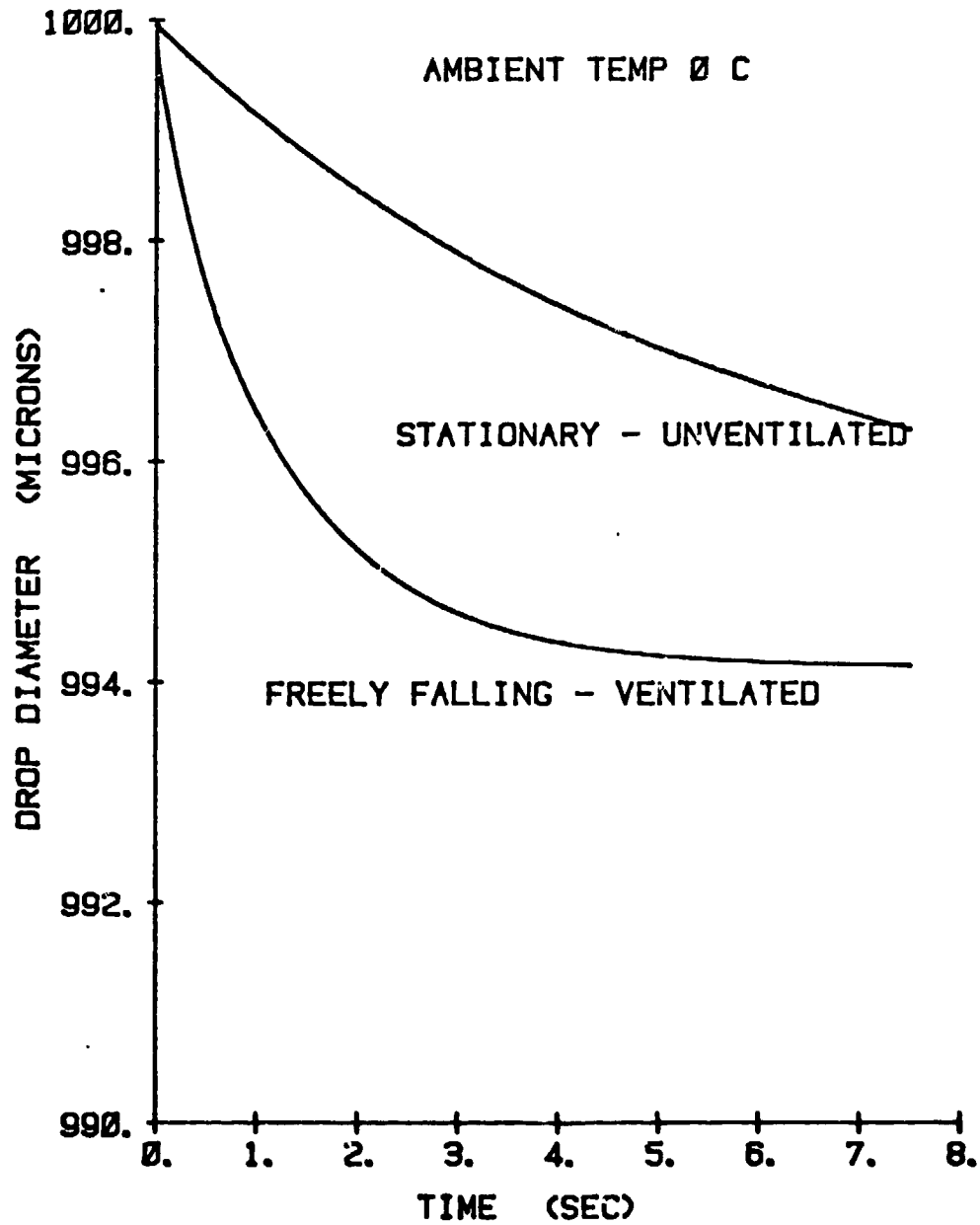
several tens of seconds. This is generally consistent with the experimental results of Kinzer and Gunn,[67] who found that a 1.35 mm drop cooling 7.5°C in subsaturated air took 4.4 seconds to equilibrate. There is, therefore, some confidence that the code reasonably approximates the changes in droplet parameters.

6.3 Simulation Results

In Figure 6.6, droplet temperature is plotted versus distance ahead of a 20-cm-thick half-body, for droplets impinging along the stagnation streamline. In this simulation, the wavelength λ was 1 cm, the maximum field strength E_0 was 7.5 kV/cm, the exponentiation length of the field ℓ was 10 cm, and the free-stream velocity was 60 m/sec. Droplets of 20, 40, 100 and 1000 micron diameters are seen to heat from the ambient temperature of -20°C to values greater than 0°C upon impact. It should be noted that all the thermodynamic losses such as evaporation and diffusion have been included and that the maximum electric field is one-half of the air breakdown value of 15 kV/cm.[68] It is clear, therefore, that for the above conditions droplets can be heated to above freezing before impacting the airfoil.

Further inspection of Figure 6.6 shows that the smallest drop (20 microns) is warmed the least. This is expected even though the smaller droplets dwell somewhat longer in the high field retion due to their low inertia. This is due to the small drops being poor absorbers by comparison to the larger drops. The trade-off between dwell time and absorption cross-section is what causes the bunching of the 20, 40 and 100 micron temperatures in Figure 6.6, while for the 1000 micron drop the strong non-Rayleigh absorption effects dominate.

FIGURE 6.6

DROPLET HEATING BY MICROWAVES AHEAD OF HALF BODY

DROPLET TEMPERATURE AT IMPACT (DEG C)

1000 MICRONS
100 MICRONS
40 MICRONS
20 MICRONS

DISTANCE AHEAD OF BODY   (10 CM UNITS)
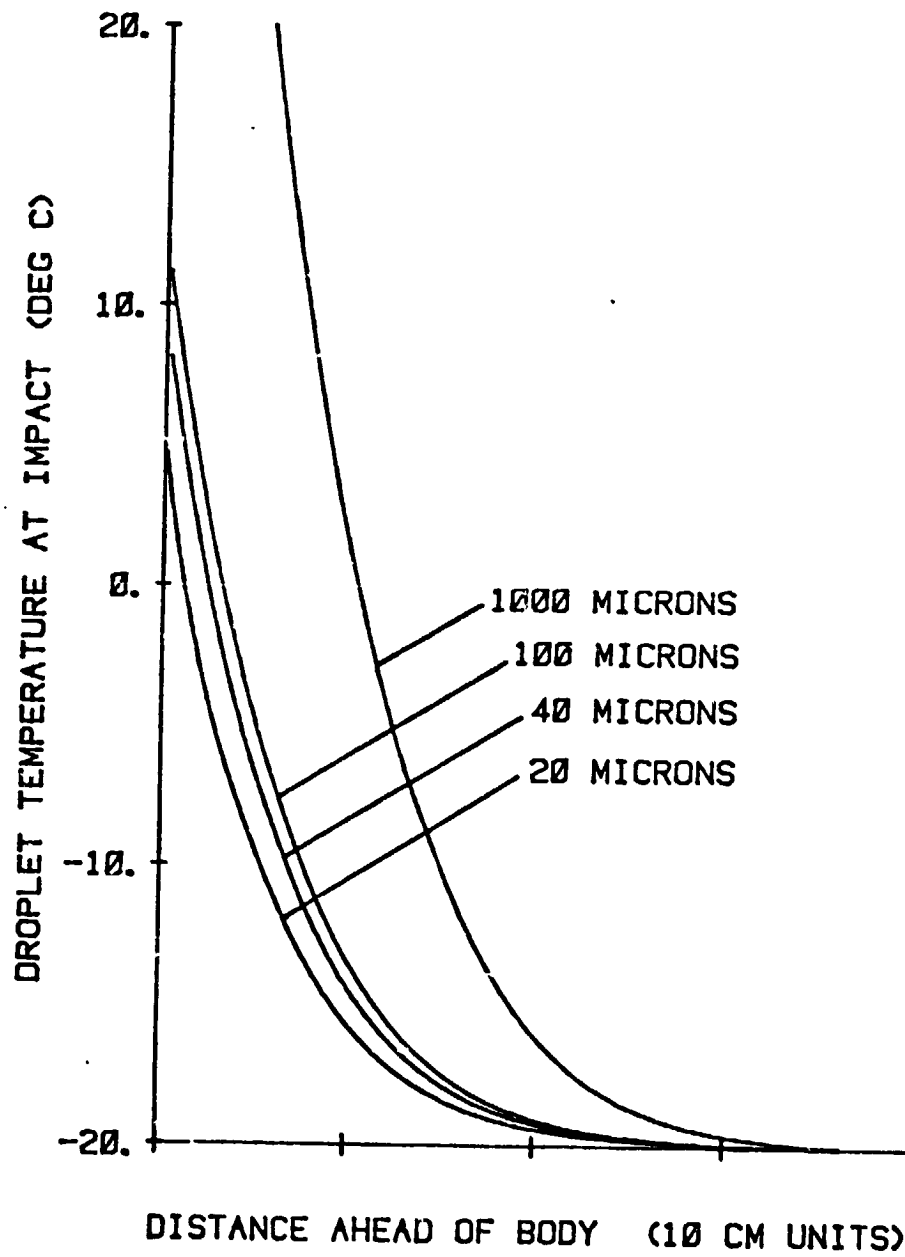
The effect of varying the electric field parameters is shown for 20 micron droplets impinging on the stagnation streamline. The 20 micron droplets have been chosen as a worst-case design point, in that diameters less than 20 microns were shown in Section 5.3 to have a low collection efficiency and their heating is, therefore, less critical.

In Figure 6.7 the droplet temperature at impact is plotted versus the maximum electric field strength for a wavelength of 1 cm and several values of the exponentiation length. For field strengths above 2.5 kV the final droplet temperature increases linearly with electric field at a rate of approximately 4.2°C/kV. The exponentiation length is seen to have a weak effect on the final droplet temperature, as the most effective heating occurs close to the airfoil. Since the ability to heat drops does not depend on long exponentiation lengths, then it is clearly advantageous to keep the electric field closely bound to the airfoil in order to minimize the heating of droplets which miss the airfoil.

In Figure 6.8, the droplet temperature at impact is plotted against wavelength for several values of the electric field and a 10-cm exponentiation length. The final temperature increases quickly with decreasing wavelength for λ less than 3 cm. Final temperatures above freezing are obtainable for λ less than 2 cm.

The field strength required to heat droplets is seen in Figure 6.7 to have a maximum value on the order of 7.5 kV/cm near the airfoil surface with $\lambda = 1$ cm. The power flux for a plane wave of 7.5 kV/cm can be calculated from the Poynting vector

$$\vec{S} = \frac{c}{4\pi} \vec{E} \times \vec{B} \tag{6.29}$$

FIGURE 6.7
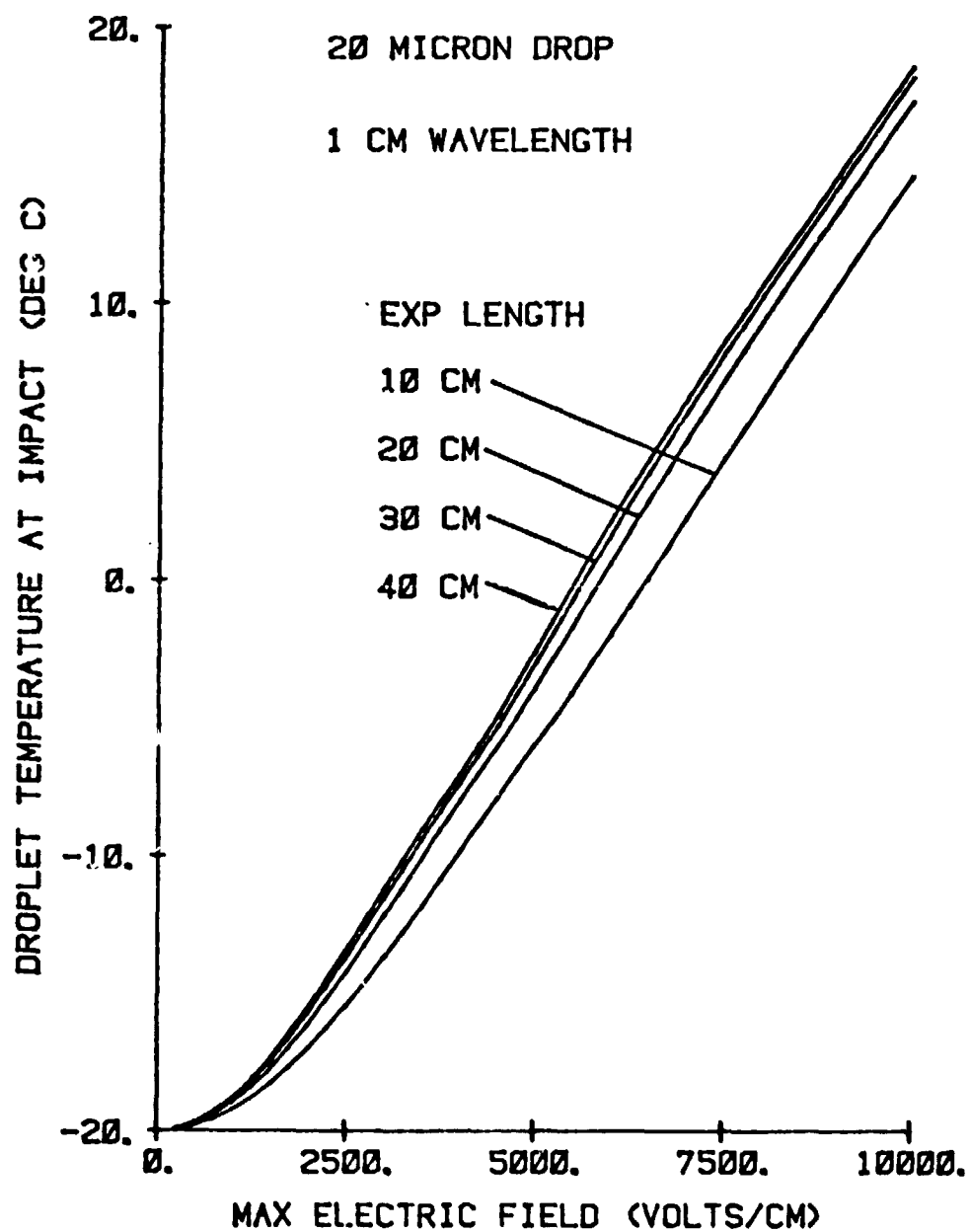
DROPLET TEMP AT IMPACT VS. MAX ELECTRIC FIELD

FIGURE 6.8

DROPLET TEMPERATURE AT IMPACT VS. WAVELENGTH

MAX ELEC FIELD

13 KV/CM

10 KV/CM

7 KV/CM

4 KV/CM

1 KV/CM

WAVELENGTH (CM)
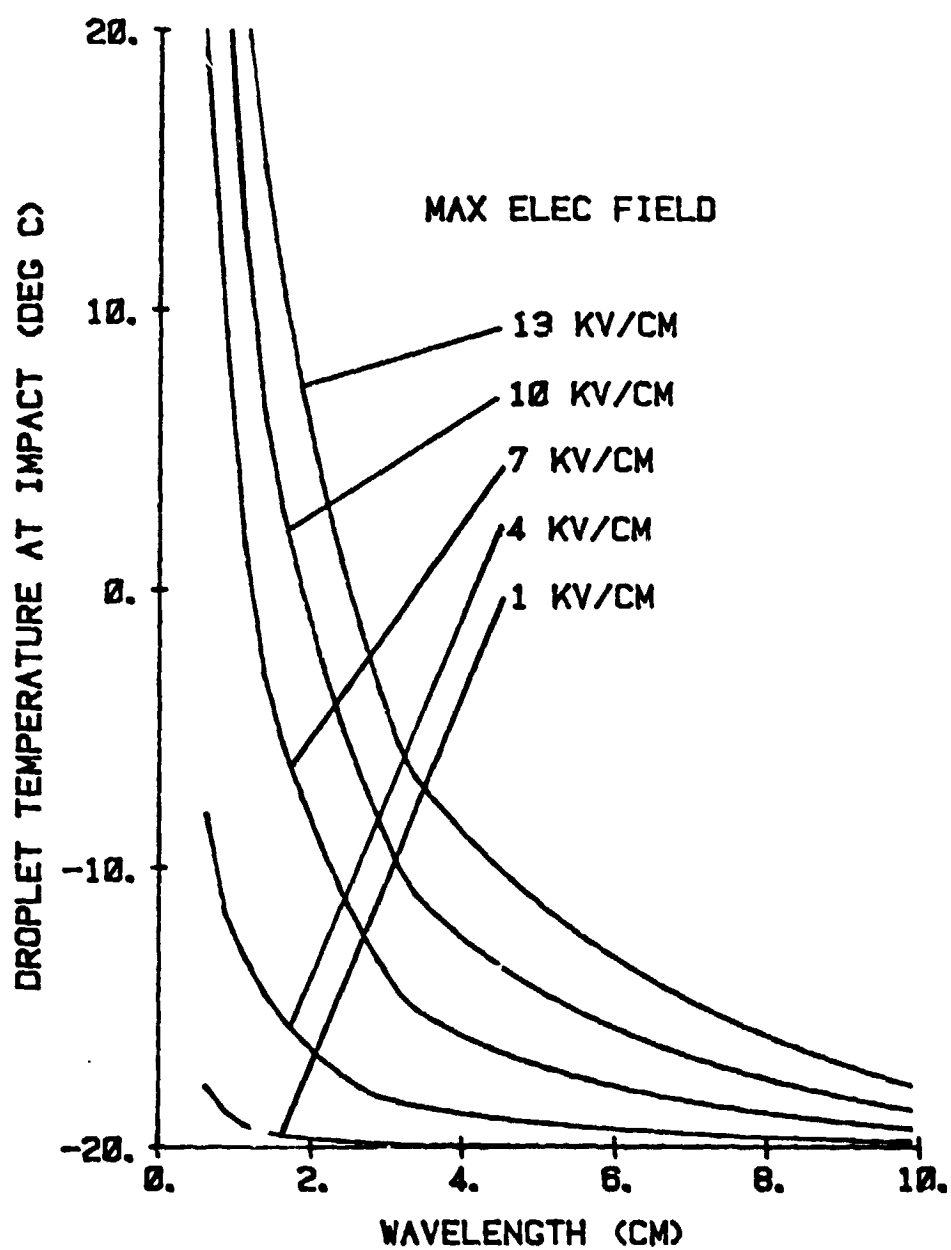
to be 74 kW/cm. This high peak power density implies large power flow in the microwave circuit. While this high power is not lost from the system, as it recirculates, it creates power handling problems. It may therefore be advantageous to keep the fields tightly bound and to operate at shorter wavelengths where the maximum electric fields are reduced, as is implied by Figure 6.8. It should also be noted that the electromagnetic fields are not necessarily plane waves and it may be possible to create a field structure which maximizes the electric field while minimizing the magnetic field. This would reduce the circuit power flux from equation 6.29, while still heating the droplets due to the non-magnetic nature of water droplet absorption.

In Figures 6.9 and 6.10, the effect of the ambient temperature and the flow velocity are plotted for 20 micron and 100 micron droplets. The maximum electric field is 7.5 kV/cm with $\lambda = 1$ cm on a 10 cm exponentiation length. In Figure 6.9 with a free-stream velocity of 60 m/sec, the final droplet temperature decreases with ambient temperature, as would be expected. It is noted that the 20 micron drop impacts at above freezing, even for ambient temperatures of -30°C and that the final temperature of the 100 micron drop averages approximately 4° warmer than the 20 micron drop.

The effect of the free-stream velocity, at a fixed ambient temperature of -20°C, is shown in Figure 6.10. As expected, the high velocities provide less time to heat the drops and their final temperatures are correspondingly lower. The 4°C to 5°C difference between the 20 and 100 micron drops is again observed.

FIGURE 6.9

DROPLET TEMP AT IMPACT VS. AMBIENT TEMP
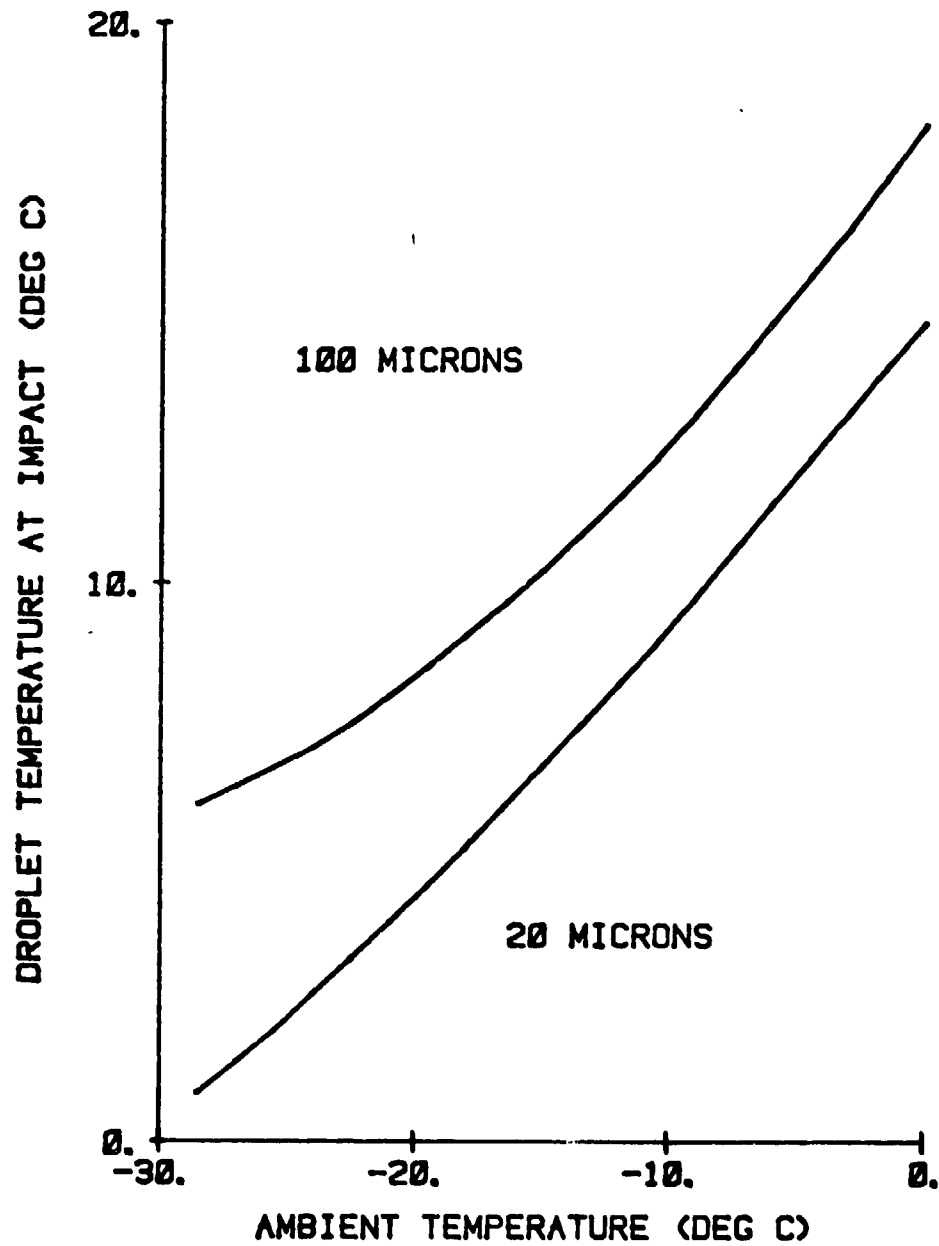
FIGURE 6.10

DROPLET TEMP AT IMPACT VS. FREE STREAM VEL.
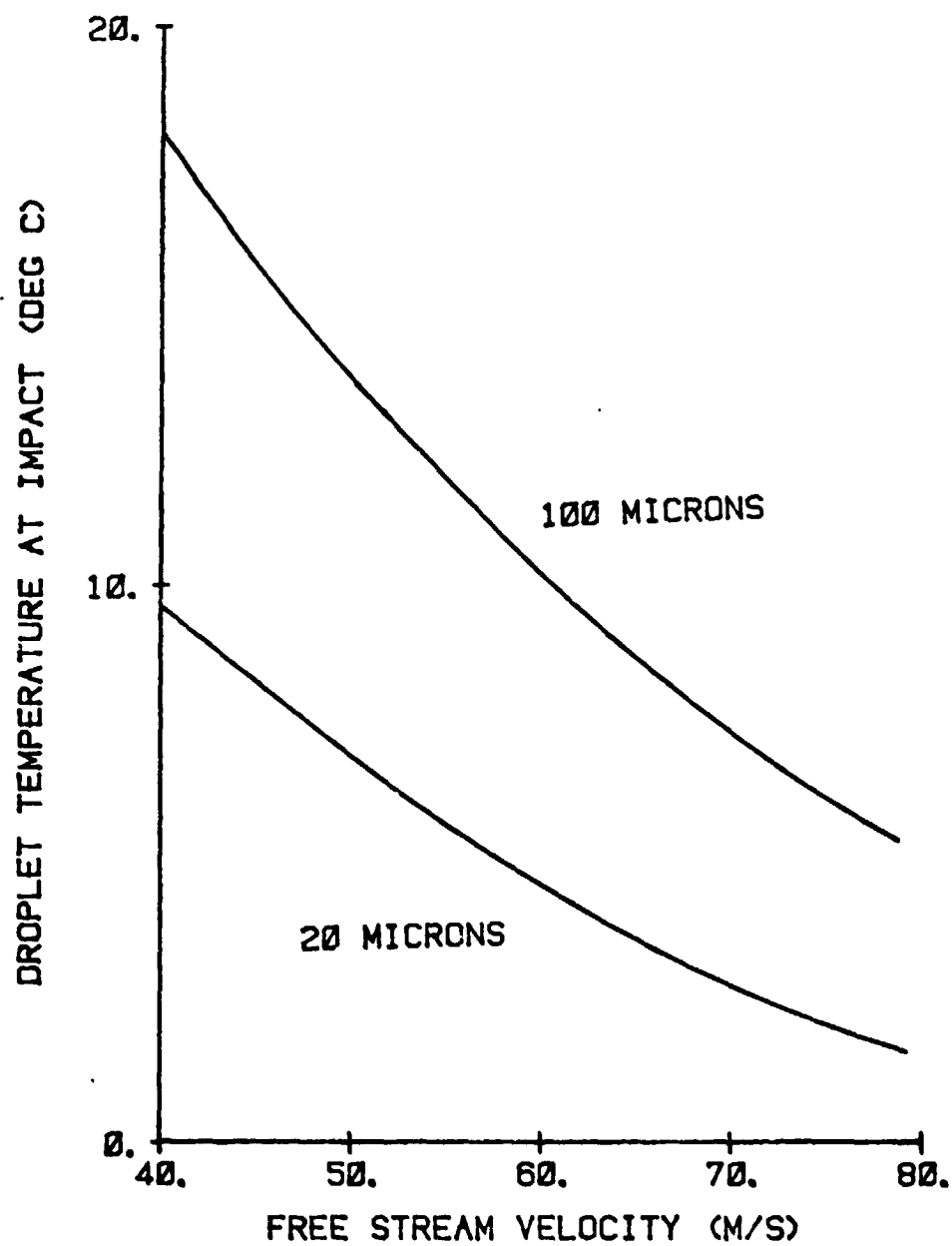
In Figure 6.11 the mass fraction is plotted versus distance ahead of the body. The value of the electric field parameters is the same as above, and the free-stream velocity is 60 m/sec. The initial value of f_w is 0.1. The large (1000 micron) drop is totally melted by the time it is within 6 cm of the body, while the smaller drops are still partially frozen upon impact. This is not considered a problem, in that most mixed-phase particles in the atmosphere are precipitation particles with dimensions on the order of millimeters.

An example of droplets which impinge from positions other than the stagnation streamline is shown in Figure 6.12. Droplet temperature at the nose of the airfoil $(x = x_s)$ is plotted against initial separation from the stagnation streamline. The droplet size is 20 microns and the reference angle θ_0 is 45°. The limit of the impingement window is also shown. The plot is somewhat misleading, in that there will be some additional heating for drops which impact behind the nose of the airfoil and the final temperature also depends on diffusive losses. It is clear, however, that the droplets which are heated the most are those within the impingement limit, and that by judicious choice of the electric field the selective heating of only the impacting droplets could be maximized.

In conclusion, a computer simulation has been made of droplets being heated by microwave radiation as they impinge onto an airfoil. The simulation utilizes the results of the preceding chapters. The results indicate that it is indeed feasible to heat droplets to above freezing prior to impact under most icing conditions. The effect of various electromagnetic field and flow parameters on droplet heating

FIGURE 6.11

MASS FRACTION OF WATER IN DROP VS. POSITION

DISTANCE AHEAD OF BODY (10 CM UNITS)

FIGURE 6. 12

FINAL DROPLET TEMP VS. INITIAL POSITION

INITIAL SEPARATION FROM STAGNATION STREAMLINE (CM)
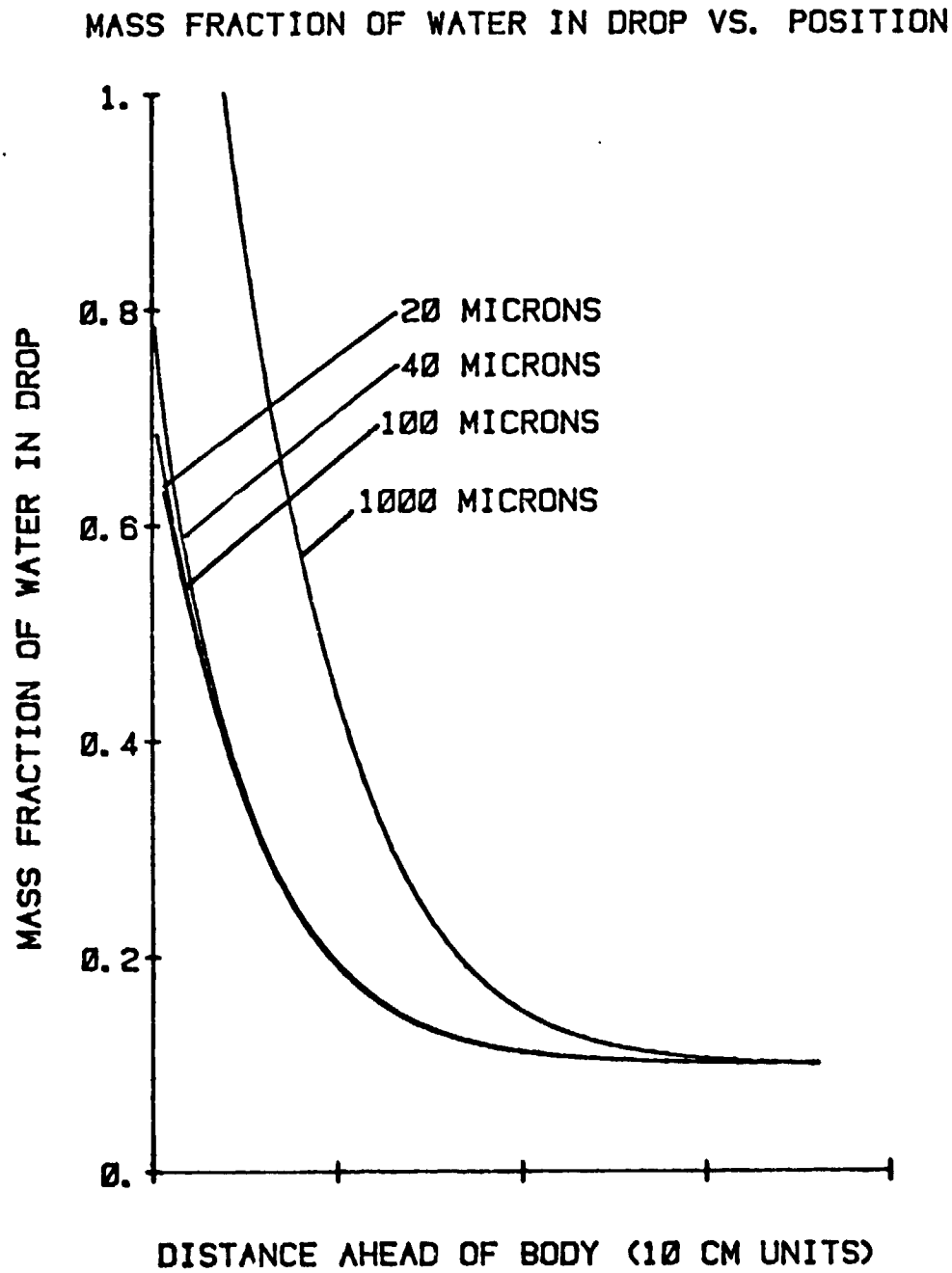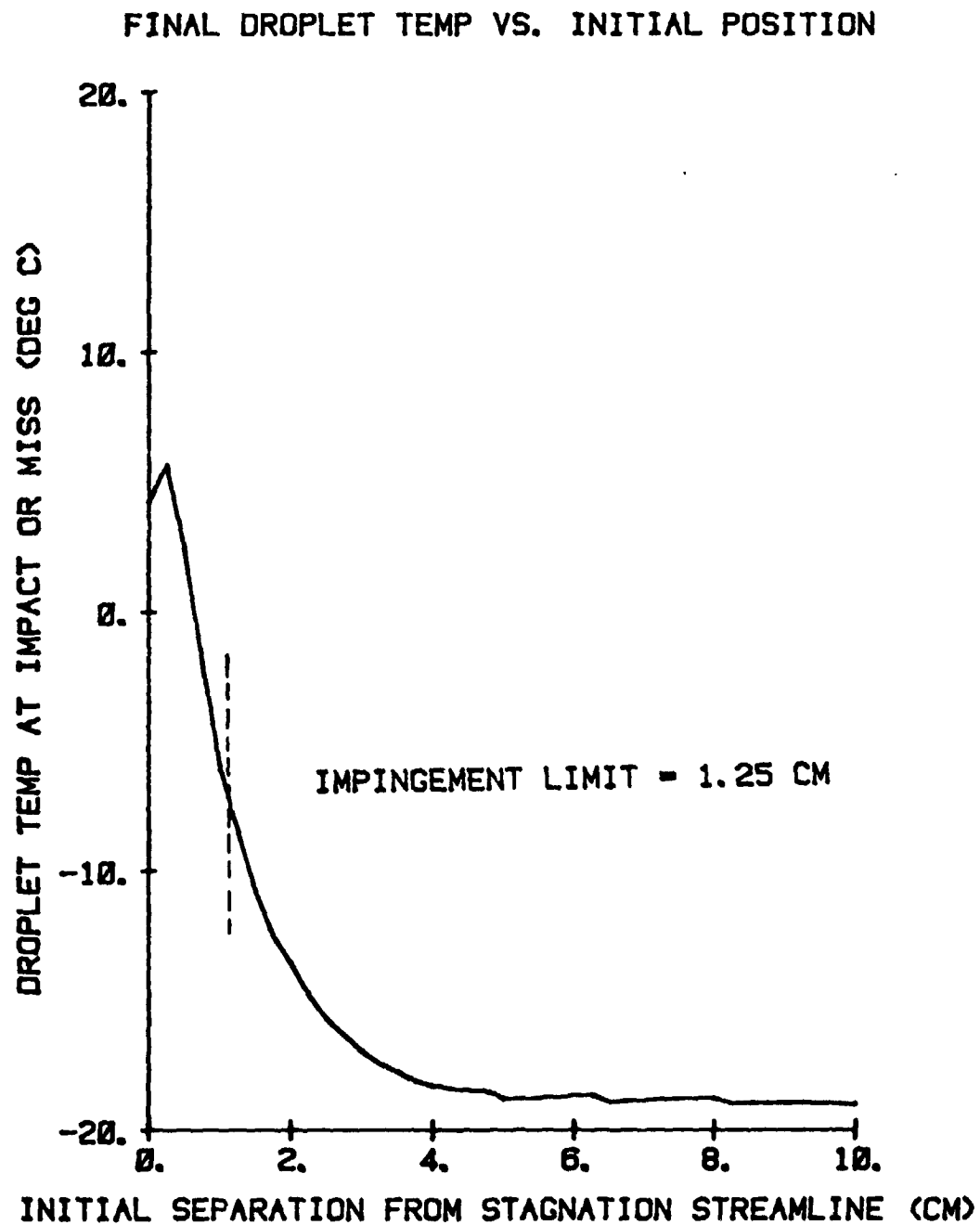
has been calculated, and the results are presented as an aid to the design and analysis of anti-icing systems which might employ the techniques of microwave heating. The results indicate that wavelengths less than 2 cm and maximum field strengths greater than 7 kV/cm are required to heat droplets to above freezing prior to impact. While the required field strength is high, it is less than the breakdown value of air, and the simulation indicates that the fields can be kept quite closely bound to the airfoil with little degradation in performance.

CHAPTER 7

CONCLUSIONS

The primary goal of this thesis was to understand the physics involved in advanced microwave anti-icing systems and to determine their feasibility in terms of the ability to heat supercooled water droplets to above freezing prior to impact. Correspondingly, this question was answered by means of a computer simulation in Chapter 6. The conclusion is that it is indeed possible to pre-heat water droplets to above freezing under anticipated icing conditions, as long as the maximum electric field exceeds 7 kw/cm and the wavelength is less than 2 cm. Detailed design curves for the electric field parameters are provided in Chapter 6.

The work was successful in demonstrating its original goal, i.e. that supercooled water droplets can be heated to above freezing ahead of the airfoil. In order to create the physically-realistic simulation from which the above conclusions were drawn, some preliminary work was necessary. The original techniques, methodology and results which were developed are most likely as significant as the original goal. These results will be reviewed briefly by chapter.

In Chapter 3, a technique was developed to accurately measure the absorption cross-section of a single droplet by its effect on the Q of a low loss resonant cavity. Using this technique, the theory of absorption by water-coated ice spheres of Aden and Kerker was experimentally confirmed for the first time. In addition, an

extension of the Aden and Kerker theory to melting of irregularly-shaped particles was made and confirmed experimentally. Finally, in Chapter 3, an extension of the resonant cavity technique allowed the dielectric properties of supercooled water to be measured, at $\lambda = 2.82$ cm, down to -17°C. This new data is shown in Figure 3.12.

In Chapter 4, the hydrodynamics of accelerated water droplets were observed in the wind tunnel by means of high-speed strobe photography. The transient deformation limit of the major-to-minor axis ratio was experimentally determined for droplets suddenly accelerated by another fluid. The result is shown in Figure 4.9. In addition, the theoretical prediction of Klett[45] as to the form of Rayleigh-Taylor instability in water droplets was unambiguously confirmed as the first six Bessel function instability modes were identified photographically. This experimental evidence verifies the theory of the maximum stable drop size in the atmosphere. The unstable break-up of large water droplets causes the truncation at approximately 5 mm observed in the atmospheric exponential droplet size distribution of Marshall and Palmer.

In Chapter 5, a computer code was written to calculate droplet trajectories, in any given flow field, and was experimentally verified. The code is useful in analyzing the susceptibility of airfoils to icing and to analyzing new ice prevention concepts. With the assistance of the code it was determined that, for cloud droplets, the larger drops contribute appreciably more to icing due to their increased collection efficiency and their increased mass. In

addition, the mechanism of the "double-horned" icing shapes resulting from large splashing droplets was observed and modeled.

Finally, in Chapter 6 the above results were amalgamated into a computer simulation, where it was seen that it is indeed possible to heat droplets to above freezing, even when evaporative and convective losses are included. From the design curves of Chapter 6, some conclusions can be drawn as to the practical requirements of a microwave anti-icing system. In Figure 6.8 where the strong influence of the wavelength on droplet heating is displayed, it is clear that the minimal wavelength is optimal in terms of heating and that a wavelength of less than 2 cm is required. Balancing the desirability of short wavelengths is the fact that microwave equipment costs tend to increase monotonically with decreasing wavelength. These factors indicate that a practical anti-icing system would operate with a wavelength of approximately 1 cm.

In Chapter 6, for $\lambda = 1$ cm it was found that a relatively high field strength of a roximately 7.5 kV was required to anti-ice in all anticipated icing conditions. This field strength is one-half the atmospheric breakdown limit. Even though the field strength was required to be large, in the results of Chapter 6 it was found that it need not be extensive, as a tightly-bound ($\ell = 10$ cm) surface wave was found to perform as well as a loosely-bound wave ($\ell = 40$ cm). This resu' indicates that it should be possible to be quite efficient in only heating the impacting water droplets. With the criteria for droplet heating determined by the above results, the practicality of microwave anti-icing systems depend solely on engineering

efficiency considerations and the ability of the microwave system
to be integrated with other systems, in a hybrid design, as discussed
in Chapter 1, to solve the runback-refreeze problem.

LIST OF SYMBOLS

A	drop major diameter
A	drop area perpendicular to the relative wind
A/B	ellipsoid axis ratio
a	sphere radius
$\vec{a}$	drop acceleration vector
a_n, b_n	magnetic and electric expansion coefficients of the scattered wave
B	drop minor diameter
$\vec{B}$	magnetic field vector
$\vec{B}_i$	incident magnetic field vector
C_d	drag coefficient
C_p	specific heat of water at constant pressure
c	speed of light
D	cylindrical cavity diameter
D_{eq}	equivolumetric sphere diameter
$\bar{D}_{eq}$	mean value of D_{eq}
D_v	water vapor diffusion coefficient
$\vec{E}$	electric field vector

$\vec{E}_i$ incident electric field vector

E_0 maximum electric field strength

E_z electric field strength in TM_{010} mode

e eccentricity of an ellipsoid

$\hat{e}_0$ polarization vector

F structure factor

f frequency

f_0 cavity resonant frequency

f_d Doppler frequency

f_n drop oscillation frequency of the nth mode

f_w mass fraction of water

$\bar{f}_h$ average heat ventilation coefficient

$\bar{f}_v$ average vapor ventilation coefficient

g, g' Gans factors

g acceleration due to gravity

H airfoil thickness

H_ϕ magnetic field strength in TM_{010} mode

h body half thickness

h_i Impingement window height

J_n n^{th} Bessel function

K dielectric parameter

K_a constant in the droplet equation of motion

$\overline{K}$ wave vector

K_a thermal diffusion coefficient

k_g gravitational wave number

$\vec{k}_0$ incident wave vector

$\vec{k}_s$ scattered wave vector

L cavity length

L_{iw} latent heat of fusion

L_{wv} latent heat of evaporation

ℓ exponential length of the electric field

M drop mass

M_i mass of ice

M_w mass of water

$\dfrac{dM_c}{dD_{ef}}$ impinging mass distribution

m complex refractive index

N	number of scatterers
N_{we}	Webber number
N_{sc}	Schmidt number
n	mode number
n	real part of the refractive index
$\hat{n}$	unit vector in the direction of propagation
P	power
P_a	ambient power
P, P'	geometrical factors for ellipsoid
P_d	power dissipated by a drop
P_w	power dissipated by the cavity walls
P_{min}, P_{max}	minimum and maximum power received
Q	quality factor
Q	heat
$\frac{dQ}{dT}$	rate of change of heat
$\vec{q}$	change in wave vector
R	rainfall rate
Re	Reynolds number
r	radial coordinate

r	interparticle spacing
S	surface function
$\vec{S}$	Poynting vector
$\vec{S}_i$	incident Poynting vector
T	temperature
T_a	ambient temperature
T(t)	cavity temperature
T_d	droplet temperature
t	time
t_0	time melting begins
t_f	time melting ends
U	energy stored in the cavity
U	free stream velocity
$\vec{u}$	fluid velocity
V	droplet volume
V_{rel}	relative wind velocity
$\vec{v}$	droplet velocity
x, y, z	Cartesian coordinates

186

$\vec{x}_j$	position of the jth scatterer
x_s	half body scale length
α	$2\pi a/\lambda$
α	instability growth rate
α	angle of attack
Γ	full width at half maximum
ϵ	complex dielectric constant
ϵ'	real part of ϵ
ϵ''	negative of the imaginary part of ϵ
η_c	airfoil collection efficiency
θ	angular coordinate
θ_0	heating code reference angle
k	negative of the imaginary part of m
λ	wavelength
λ	Marshall-Palmer coefficient
μ	dynamic viscosity
ζ	ellipsoid axis of revolution
ζ, η, χ	ellipsoid coordinates

ρ	density
ρ_i	density of ice
ρ_w	density of water
ρ_v	density of water vapor
ρ, ϕ, z	cylindrical coordinates
σ	surface tension
σ	cross-section
σ_b	backscatter cross-section
σ_a	absorption cross-section
σ_s	scattering cross-section
σ_t	total cross-section
$\dfrac{d\sigma}{d\Omega}$	diffential cross-section
ϕ	velocity potential function
Ω	solid angle

REFERENCES

1. "AGARD Conference on Icing Testing for Aircraft Engines", AGARD-CP-236 (1978).

2. "NASA-FAA Conference on Aircraft Icing", NASA CP-2086/FAA RD-78-109 (1978).

3. P.V. Hobbs, Ice Physics (Oxford Univ. Press, Oxford, 1974).

4. U.S. Federal Aviation Regulations, Part 25.

5. U.S. Federal Aviation Administration, AC-20-73 (1971).

6. H.R. Pruppacher and J.D. Klett, Microphysics of Clouds and Precipitation (D. Reidel, Dordrecht: Holland, 1978).

7. P.J. Perkins, NACA RM E52J06 (1952).

8. D. Atlas, J. Meteorology, 11, 309 (1954).

9. B. Magenheim, USAAMRDL-TR-77-34 (1977).

10. B. Magenheim and F. Hains, USAAMRDL-TR-76-18 (1976).

11. R.J. Hansman, Jr. and W. Hollister, NASA Conference Proceeding (to be published - 1981).

12. R.J. Hansman, Jr., U.S. Patent Serial No. 163,520 (Approved March 1982).

13. V.H. Gray, NACA TN 2799 (1952).

14. AGARD Working Group on Rotorcraft Icing, AGARD-AR-166 (1981).

15. R. Collins, Foundations for Microwave Engineering (McGraw-Hill, New York, 1966).

16. A.R. von Hippel, Dielectric Materials and Applications (MIT Press, Cambridge, 1954).

17. J.W. Ryde, The Attenuation and Radar Echoes Produced at Centimetre Wavelengths by Various Meteorological Phenomena (Phys. Soc. London, 1947).

18. G. Mie, Ann. Physik, 25, 377 (1908).

19. Lord Rayleigh, Phil. Mag. XLI, 107 (1871).

20. Lord Rayleigh, Phil. Mag. XLVII, 375 (1899).

21. J.S. Stratton, Electromagnetic Theory (McGraw-Hill, New York, 1941), pp. 563-573.

22. A. Lowan, Tables of Scattering Functions for Spherical Particles (National Bureau of Standards, Washington, 1949).

23. K.L.S. Gunn and T.W.R. East, Quart. J. Royal Meteor. Soc. 80, 522 (1954).

24. B.M. Herman and L.S. Batten, Quart. J. Royal Meteor. Soc. 87, 233 (1961).

25. L.J. Batten, Radar Observation of the Atmosphere (Univ. of Chicago Press, Chicago, 1973).

26. R. Gans, Ann. Physik. 37, 881 (1912).

27. D. Atlas, M. Kerker, and W. Hitschfeld, J. Atm. and Terr. Physics, 3, 108-119 (1953).

28. J.D. Jackson, Classical Electrodynamics (J. Wiley and Sons, New York, 1975).

29. A. Aden and M. Kerker, J. Appl. Phys. 22, 1242 (1951).

30. M. P. Langleben and K.L. Gunn, McGill Univ. Stormy Weather Group MW-5 (1952).

31. B. Herman and L. Batten, J. Met. 18, 468 (1960).

32. L. Batten, S. Browning and B. Herman, J. Appl. Met. 9, 832 (1970).

33. D. Atlas, W. Harper, F. Ludlum, and W. Macklin, Quart. J. Royal Meteor. Soc. 86, 468 (1960).

34. N. Labrum, J. Appl. Phys. 23, 1324 (1952).

35. N. Labrum, J. Appl. Phys. 23, 1320 (1952).

36. Bell Laboratory Technical Staff, Radar Systems and Components (Van Nostrand, New York, 1949).

37. C. Montgomery (ed.), Techniques of Microwave Measurements: Rad. Lab Series 11 (McGraw-Hill, New York, 1947), pp. 308-319.

38. H. Pruppacher and P. Pitter, J. Atm. Sciences 28, 86 (1970).

39. H. Pruppac and K Beard, Quart. J. Royal Meteor. Soc. 96, 247 (1970).

40. J.E. McDonald, J. Meteor. 11, 57-80 (1954).

41. A. Spilhaus, J. Meteor. 5, 108 (1948).

42. T. Taylor and A. Acrivos, J. Fluid Mech. 18, 446 (1964).

43. M. Komobayasi and K. Isomo, J. Meteor. Soc. Japan, Ser. 2 42, 330 (1964).

44. J. McTaggart-Cowan and R. List, J. Atm. Sci. 32, 1401 (1975).

45. J. Klett, J. Atm. Sci. 28, 646 (1970).

46. A.W. Green, J. Appl. Meteor. 14, 1578 (1975).

47. Lord Rayleigh, Phil. Mag. XIV, 184 (1882).

48. I. Langmuir, J. Meteor. 5, 175 (1948).

49. J.B. Mathews and B.J. Mason, Quart. J. Royal Meteor. Soc. 90, 275 (1964).

50. K.V. Beard and H.R. Pruppacher, J. Atmos. Sci. 26, 1060 (1969).

51. C.S. Yih, Dynamics of Nonhomogeneous Fluids (MacMillan, New York, 1965), pp. 142-145.

52. M. Abromowitz and J. Stegun, Handbook of Mathematical Functions (Dover, New York, 1964), pp. 355-435.

53. M. Glauert, British A.R.C., 2025 (1940).

54. A. Kantrowitz, NACA TN 779 (1940).

55. I. Langmuir and K. Blodgett, Dept. of Commerce PB 27565 (1945).

56. N. Bergron, NACA TN1397 (1947).

57. R. Brun, J. Serafini, and H. Gallagher, NACA TN 2903 (1953).

58. R. Brun and H. Mergler, NACA TN 2904 (1953).

59. R. Brun, H. Gallagher, and D. Vogt, NACA TN 2952 (1953).

60. R. List, Smithsonian Meteorological Tables (Smithsonian, Washington, D.C., 1949).

61. R. Gunn and G. Kinzer, J. Meteor. 6, 243 (1949).

62. M. Potter and J. Foss, Fluid Mechanics (Ronald, New York, 1975).

63. J.S. Marshall and W.M. Palmer, J. Meteor. 5, 165 (1948).

64. D. Atlas, Advances in Geophysics 10, 318 (1964).

65. K.V. Beard and H.R. Pruppacher, J. Atmos. Sci. $\underline{28}$, 1455 (1971).

66. W.D. Hall and H.R. Pruppacher, J. Atmos. Sci. $\underline{33}$, 1995 (1977).

67. G.D. Kinzer and R. Gunn, J. Meteor. $\underline{8}$, 71 (1951).

68. A.D. MacDonald, Microwave Breakdown in Gases (Wiley, New York, 1966).